LUDWIG-MAXIMILIANS-UNIVERSITÄT
MÜNCHEN

Master Thesis in:
Theoretical and Mathematical Physics

# Erasure of Defects: Vortex Unwinding by Domain Wall Sweeping

**Author: Juan Sebastian Valbuena Bermúdez**
**Supervisor: Prof. Dr. Gia Dvali**

LUDWIG-MAXIMILIANS-UNIVERSITÄT
MÜNCHEN

GROUP OF THEORETICAL PARTICLE PHYSICS

Master Thesis in:
Theoretical and Mathematical Physics

# Erasure of Defects: Vortex Unwinding by Domain Wall Sweeping

Author: Juan Sebastian Valbuena Bermúdez
Supervisor: Prof. Dr. Gia Dvali
Submission Date: December 2019

Becario Colfuturo: Promoción 2019

I confirm that the master thesis in theoretical and mathematical physics I am submitting is my own work. It has been composed by me and is based on my own work, unless stated otherwise. All references have been quoted, and all sources of information have been acknowledged.

Münich, December 2019 Juan Sebastian Valbuena Bermúdez

# Acknowledgments

I would like to express my sincere gratitude to my thesis advisor Prof. Gia Dvali. His valuable guidance, keen interest, and encouragement consistently helped me while developing this project. His support, and the support of my colleagues at the theoretical particle physics group has been invaluable. I take this opportunity to especially thank Michael Zantedeschi, Andrei Kovtun, and Andrea Giugno for all the illuminating discussions, and remarkable suggestions.

I am very grateful to COLFUTURO and DAAD. These institutions provided me the financial support needed to complete my master's program. In this regard, this venture would not be possible without Luz Angela Tellez, Floralba Bermudez, and Jose Valbuena. Thank you.

I would like to thank my family and friends, who were a constant source of motivation during my years of study. Finally, I thank my beloved Daniela. Her permanent support and continuous encouragement have accompanied me throughout all the stages of this trip, and I am glad for that.

# Abstract

Topological defects–such as Domain Walls, cosmic strings, and magnetic monopoles–are expected to appear during a phase transition in GUT of particle physics. The concentration of such monopoles in the early universe was estimated to be the dominant matter in the universe. However, this is in tension with the fact that monopoles have not been observed. The former is known as the cosmological monopole problem. Different solutions to this problem are known today, being inflation the most well known. In this scenario, the universe inflates, dilutes the monopoles, and their density decreases to acceptable levels. Another solution was proposed by Dvali, Liu, and Vachaspati in 1997. The main idea is that Domain Walls, generated during the same phase transition, swept away the monopoles before decaying.

In general, this solution proposes that defect interactions lead to a defect erasure mechanism. This mechanism has been investigated in a $SU(5)$ Grand unified model. Besides, it has been recognized in the interactions of skyrmions with walls, and vortices with walls in $^3He$. In the present work, we explore this mechanism in yet another system. We study the unwinding process of a vortex during the collision with a layer of Coulomb vacuum. This layer is a non-topological Domain Wall containing a core with a Coulomb-like phase, inside which the whole symmetry group is restored.

Specifically, we considered the $(2+1)$-dimensional model of a complex scalar field with a $U(1)$ gauge symmetry, and sextic potential $V(\phi) = \lambda^2|\phi|^2(|\phi|^2 - \nu^2)^2$. In this model, the zero homotopy group and the fundamental group of the vacuum manifold are non-trivial. Consequently, Domain Walls and vortices belong to the spectrum of this model. A $(\nu, 0)$-Domain Wall is a topological field configuration interpolating the Higgs ($\langle|\phi|\rangle^2 = \nu^2$), and the Coulomb ($\langle|\phi|\rangle^2 = 0$) vacua. In this setup, a $(\nu, 0, \nu)$-Domain Wall configuration forms a Coulomb vacuum layer characterized by its width $l$. Although this configuration is unstable, we find numerically that if $40m_h^{-1} \lesssim L$, the layer can be considered to be stable for time scales of order $\mathcal{O}(10^2 m_h^{-1})$, where $m_h$ is the mass of the Higgs-like boson. We verified that this result holds for neutral and charged Domain Walls.

On the other hand, the vortices in the $\phi^6$ model are formed in the Higgs vacuum, and are similar to the Nielsen-Olesen vortex lines. The vortex field profiles are computed numerically, and analytical asymptotic approximations are found. Finally, the collision of a vortex with a layer of Coulomb vacuum is simulated numerically for different regimes of the parameters $\lambda$, $\nu$, the charge $e$, and the winding number $n$. Within this approach, it is found that none of the vortices crosses the Coulomb vacuum layer. We observe how the collision leads to the unwinding of the vortex, and the unconfinement of the magnetic flux which dissipates in the core of the layer. We find that this defect erasure mechanism occurs for all considered regimes of the parameter space. According to these results, we suggest the independence of this mechanism from the values of the parameters, and we argue how this mechanism can be generalised to more general theories higher $(3+1)$ dimensions.

# Contents

# 1. Introduction and Motivation

The Standard Model of particle physics (SM) has been proven to be an accurate description of fundamental interactions up to an energy scale of order 100GeV. However, there are significant problems in high energy physics and cosmology that can not be answered within the SM. Among these problems are the neutrino mass problem, the strong CP problem, the origin of baryon asymmetry in the universe, and the nature of dark matter. As a consequence, extensions of the SM are required to approach these problems.

Possible extensions of the SM, within which the gauge interactions are merged into a single interaction, are known as Grand Unified Theories (GUT). If such unification exists, there is the possibility that there was a grand unification epoch in the very early universe. In the hot big bang cosmological model, the universe starts at a very high temperature. As the universe expands and cools down, it undergoes a sequence of phase transitions at different critical temperatures corresponding to different symmetry breaking scales. During these phase transitions, and depending on the structure of the vacuum manifold, different topological defects–such as Domain Walls, cosmic strings, and magnetic monopoles–may be produced. Although topological defects have not been observed, searches for magnetic monopoles are currently carried out[1].Besides, observations of the cosmological microwave background have constrained the surface tension of Domain Walls to be $\sigma < 3.85 \times 10^{9}\mathrm{kg/m^2}$, which corresponds to an energy scale of formation for Domain Walls of 0.93 MeV [2]. However, the no observation of topological defects is tension with the predictions from different GUT, in which the monopoles were expected to be the dominant matter in the universe. In consequence, a mechanism capable of solving this tension–known as the cosmological monopole problem–is required.

In the following sections, we outline the general ideas behind GUT, spontaneous symmetry breaking, and phase transitions in the early universe. Afterwards, we present the basic properties, and classification of topological defects, and the Kibble-Zurek mechanism for defects formation. Lastly, we establish in more detail the magnetic monopole problem and discuss different solutions to this problem. Finally, we focus on the mechanism proposed by Dvali, Liu, and Vachaspati in which the magnetic monopoles are swept away by the Domain Walls.

## 1.1. The Higgs mechanism in the Standard Model and Grand Unified Theories

The strong, weak, and electromagnetic interactions are the three gauge interactions of the $SU(3) \times SU(2) \times U(1)$ Standard Model (SM). In general, gauge theories predict massless gauge bosons. However, it is observed that the mediators of the weak force–the $W^{\pm}$, and the $Z$ bosons–are massive. The origin of the mass of the gauge bosons is explained by the Higgs mechanism. Due to the important role that this mechanism plays in the SM and GUT, and to introduce some notation, we review it here with few examples: the abelian-Higgs model, the non-abelian generalization, and the Glashow-Weinberg-Salam model.

*The abelian-Higgs model:*

Following [3], lets consider the abelian-Higgs model. It is a model with a $U(1)$ gauge symmetry, for which the Lagrangian is given by

$$\mathcal{L}[\varphi, A_\mu] = -\frac{1}{4}F_{\mu\nu}F^{\mu\nu} + (D_\mu\varphi)^* D^\mu\varphi - V(\varphi), \tag{1.1}$$

where $\varphi$ is a complex scalar field, $A_\mu$ is the vector potential with field strength $F_{\mu\nu} = \partial_\mu A_\nu - \partial_\nu A_\mu$, and $D_\mu = \partial_\mu - ieA_\mu$ is the covariant derivative, where $e$ is the coupling constant. If not stated otherwise, we will use natural units, and Greek indices $\mu$, and $\nu$ represent spacetime indices, while Latin indexes $i$, $j$, and $k$ represent space indexes. The scalar field potential is given by

$$V(\varphi) = \frac{1}{4}\lambda\left(\varphi\varphi^* - \nu^2\right)^2, \tag{1.2}$$

where we consider $\nu$, and $\lambda$ to be positive reals. The Lagrangian is invariant under the gauge transformations of the fields

$$\begin{aligned} A_\mu(x) &\rightarrow A'_\mu(x) = A_\mu(x) + \frac{1}{e}\partial_\mu\alpha(x), \\ \varphi(x) &\rightarrow \varphi'(x) = \mathrm{e}^{i\alpha(x)}\varphi(x), \end{aligned}$$

where $\alpha(x)$ is an arbitrary real function. A ground state, or vacuum, is a configuration of the fields which minimises the energy functional

$$\begin{aligned} E[\varphi, A_\mu] = \int d^3x \bigg[ &\frac{1}{2}F_{0i}F_{0i} + \frac{1}{4}F_{ij}F^{ij} \\ &+ (D_0\varphi)^* D_0\varphi + (D_i\varphi)^* D_i\varphi + V(\varphi) \bigg] \end{aligned} \tag{1.3}$$

Notice that the energy $E[\varphi, A_\mu]$ is gauge-invariant. Then any gauge transformation of a vacuum state is again a vacuum state. The first four terms of the integrand in 1.3 are non-negative. Then, in order to minimize the energy functional, lets consider the case when all this four terms vanish. This occurs when $A_\mu$ is pure gauge, i.e.

$$A_\mu = \frac{1}{e}\partial_\mu \alpha(x),$$

and, in consequence, $D_\mu \varphi = (\partial_\mu - i\partial_\mu \alpha(x))\varphi = 0$, i.e.

$$\varphi = \mathrm{e}^{i\alpha(x)}\varphi_0, \tag{1.4}$$

where the real constant $\varphi_0$ is determined from the minimization of the scalar field potential $V(\varphi)$, and it is equal to $\varphi_0 = \nu$. Then the vacuum expectation value (VEV) of the norm of the field $\varphi$ is non-zero, $\langle|\varphi|\rangle = \varphi_0 = \nu$.

Now, in order to study the spectrum of excitations of the theory, we need to study perturbations about a vacuum state. Since $\alpha(x)$ is arbitrary, it is always possible to perform a gauge transformation such that we fixed the gauge to be unitary, i.e., we can choose $\alpha(x) = 0$ such that the vacuum configuration is given by

$$A_\mu^{(v)} = 0,\ \varphi^{(v)} = \nu \tag{1.5}$$

Let's consider excitation about this vacuum state. Excitations of $A_\mu$ are described by $A_\mu$ itself, while excitations of $\varphi$ about its VEV can be described by two real fields $h$, and $\theta$ such that

$$\varphi = \left(\nu + \frac{1}{\sqrt{2}}h\right)e^{i\theta}.$$

In the analogous model with a global $U(1)$ symmetry, the field $\theta$ is known as the Nambu-Goldstone field. Rewriting the scalar field potential in terms of $h$, and $\theta$ we find:

$$V(\varphi) = V(h) = \frac{1}{2}\lambda\nu^2 h^2 + \frac{\lambda\nu}{2\sqrt{2}}h^3 + \frac{\lambda}{16}h^4.$$

In order to bring the Lagrangian to the canonical form (sum of the Lagrangian of individual fields), we introduce the field

$$B_\mu = A_\mu - \frac{1}{e}\partial_\mu\theta,$$

and substitute the field variables $(\varphi, A_\mu)$ by $(h, B_\mu)$. Then the Lagrangian 1.1 becomes

$$\mathcal{L}[h, B_\mu] = \frac{1}{2}\partial_\mu h\partial^\mu h + \frac{1}{2}m_h^2 h^2 - \frac{1}{4}B_{\mu\nu}B^{\mu\nu} + \frac{1}{2}m_v^2 B_\mu B^\mu + \mathcal{L}_{\text{int}}, \tag{1.6}$$

where $B_{\mu\nu} = \partial_\mu B_\nu - \partial_\nu B_\mu$, $m_h = \sqrt{\lambda}\nu$, $m_v = \sqrt{2}e\nu$, and the interaction part of the Lagrangian is given by

$$\mathcal{L}_{\text{int}} = \frac{\lambda\nu}{2\sqrt{2}}h^3 + \frac{\lambda}{16}h^4 + \sqrt{2}e^2\nu B_\mu B^\mu h + \frac{1}{2}e^2 B_\mu B^\mu h^2.$$

From the canonical form 1.6, we get the spectrum of excitations of the theory. It is composed by a real scalar field, $h$, with mass $m_h$, and a massive gauge boson, $B_\mu$, with mass $m_v$. Observe the appearance of a mass term for the vector field $B_\mu$, and the disappearance of the field $\theta$. Loosely speaking, the gauge boson acquires mass while "eating up" the Nambu-Goldstone boson. We remark here that our starting point, the Lagrangian 1.1, as well as the Lagrangian 1.6 are gauge-invariant. Within this example lies the essence of the Higgs Mechanism. The field $h$ is called the Higgs field, and the corresponding particle is the Higgs boson[1].

*The non-abelian case:*

In general, the Higgs mechanism can be generalised to non-abelian theories. Following [4], we start with the case of global symmetries. Let $G$ be a compact group with generators[2] $T^a$ , and let $\boldsymbol{\varphi} = \{\varphi_i\}$ be $n$ real scalar fields in a real unitary representation $D$ of $G$. We consider the Lagrangian

$$\mathcal{L} = \frac{1}{2}(\partial_\mu \boldsymbol{\varphi})^\dagger \partial^\mu \boldsymbol{\varphi} - V(\boldsymbol{\varphi}) \tag{1.7}$$

to be invariant under the global symmetry. Thereafter, under the transformation $\boldsymbol{\varphi} \to D(g)\boldsymbol{\varphi}$,

$$V(\boldsymbol{\varphi}) = V(D(g)\boldsymbol{\varphi}),$$

for all $g \in G$. In the case when the minimum of the potential are at non-vanishing values of $\boldsymbol{\varphi}$, the symmetry is said to be spontaneously broken, and the field $\boldsymbol{\varphi}$ will develop a non-vanishing vacuum expectation value $\langle \boldsymbol{\varphi} \rangle = \boldsymbol{\varphi}_0$. The little group $H$ of $G$ with respect to $\boldsymbol{\varphi}_0$, or unbroken subgroup, is formed by the elements of $G$ that leave $\boldsymbol{\varphi}_0$ invariant, i.e.

$$H = \{g \in G | D(g)\boldsymbol{\varphi}_0 = \boldsymbol{\varphi}_0\}.$$

Then, the generators $t^h$ of $H$ annihilate $\boldsymbol{\varphi}_0$, i.e. $t^h\boldsymbol{\varphi}_0 = 0$. Choosing a basis $\{T^a\}$ for the Lie algebra of $G$ such that $\{t^h\} \subset \{T^a\}$, we refer to the elements of $\{t^h\}$ as the unbroken generators, and the remainder generators of $G$, the elements of $\{t'^b\} = \{T^a\} - \{t^h\}$, as the broken generators, i.e. $t'^b\boldsymbol{\varphi}_0 \neq 0$. Without loss of generality, let $\boldsymbol{\varphi}^{(v)} = \boldsymbol{\varphi}_0$ be a ground state. Assuming that there is no accidental degeneracy, all possible vacua have the form $\boldsymbol{\varphi} = D(g)\boldsymbol{\varphi}_0$, where $g$ does not depend on $x$. In other words, if $\mathcal{M}$ is the set of classical vacua, then $G$ acts transitively on $\mathcal{M}$, where the action is determined by the representation $D$. Thus $\mathcal{M}$ can be identified with the coset space,

$$\mathcal{M} = G/H,$$

which is refereed to as the vacuum manifold.

[1] The term "Higgs field" is also applied to the scalar field $\varphi$, whose vacuum expectation value is non-trivial.

[2] More precisely, let $\{L^a\}$ be a basis for the Lie algebra of $G$ and $D$ the adjoint representation. Here $a = 1, ...N$, where $N$ is the dimension of the Lie algebra of $G$. We shall assume the correspondence $T^a = D(L^a)$.

Now, we consider perturbations about the vacuum state $\boldsymbol{\varphi}^{(v)}$ in order to get the spectrum of excitations. The perturbations can be described by a real scalar field $\boldsymbol{\varphi'} = \{\varphi'_i\}$, such that $\boldsymbol{\varphi} = \boldsymbol{\varphi}_0 + \boldsymbol{\varphi}'$. Rewriting the Lagrangian 1.7 up to second order on $\varphi'_i$, we get

$$\mathcal{L} = \frac{1}{2}\partial_\mu \varphi'_i \partial^\mu \varphi'_i - \frac{1}{2}\mu^2_{ij}\varphi'_i\varphi'_j = \frac{1}{2}\partial_\mu \boldsymbol{\varphi}'^\dagger \partial^\mu \boldsymbol{\varphi}' - \frac{1}{2}\boldsymbol{\varphi}'^\dagger \boldsymbol{\mu}^2 \boldsymbol{\varphi}', \tag{1.8}$$

where

$$\mu^2_{ij} = \left[\frac{\partial^2 V}{\partial\varphi_i \partial\varphi_j}\right]_{\varphi=\varphi_0}. \tag{1.9}$$

Since $\boldsymbol{\varphi_0}$ is a minimum of $V(\varphi)$, and $V(\boldsymbol{\varphi}) = V(D(g)\boldsymbol{\varphi})$, it follows that

$$\begin{aligned}
0 &= \frac{\partial V}{\partial \varphi_i} T^a_{ij}\varphi_j \\
0 &= \left[\frac{\partial^2 V}{\partial\varphi_i\partial\varphi_j} T^a_{jk}\varphi_k + \frac{\partial V}{\partial\varphi_j} T^a_{jk}\delta_{ki}\right]_{\varphi=\varphi_0} \\
0 &= \mu^2_{ij} T^a_{jk}\varphi_{0_k} = \boldsymbol{\mu}^2 T^a \boldsymbol{\varphi_0}.
\end{aligned}$$

The vectors $t'^b\boldsymbol{\varphi}_0$ are linearly independent. In consequence, for each broken generator $t'^b$, the vector $t'^b\boldsymbol{\varphi}_0$ is an eigenvector of $\mu^2$ with zero eigenvalue. In general, the remaining eigenvalues are non-zero. If $N$ is the number of generators of $G$, and $K$ the number of generators of $H$, then the spectrum of excitations is composed by $n-(N-K)$ massive modes, and $N-K$ massless modes corresponding to the Nambu-Goldstone bosons.

Considering now gauge invariance, we introduce the gauge fields $A^a_\mu = 0$. Let $L^a$ be a basis for the Lie algebra of $G$ satisfying the commutation relations

$$[L^a, L^b] = -i f_{abc} L^c,$$

where $f_{abc}$ are the structure constant of $G$. The non-abelian Higgs model is described by the gauge-invariant Lagrangian

$$\mathcal{L} = \frac{1}{2}(D_\mu\boldsymbol{\varphi})^\dagger D^\mu\boldsymbol{\varphi} - V(\boldsymbol{\varphi}) - \frac{1}{4}F^a{}_{\mu\nu}F^{a\mu\nu} \tag{1.10}$$

where

$$F^a_{\mu\nu} = \partial_\mu A^a{}_\nu - \partial_\nu A^a{}_\mu + e f_{abc} A^b{}_\mu A^c{}_\nu$$

is the Yang Mills field strenght, $e$ is the gauge coupling constant, and $D_\mu\boldsymbol{\varphi}$ is the gauge-covariant derivative

$$D_\mu = (\partial_\mu - ieA^a{}_\mu T^a)\boldsymbol{\varphi}$$

The gauge transformation is given by the following transformation of fields

$$\begin{aligned}
\mathcal{A}_\mu &\rightarrow g\mathcal{A}_\mu g^{-1} + ie^{-1}g^{-1}\partial_\mu g, \\
\boldsymbol{\varphi} &\rightarrow D(g)\boldsymbol{\varphi},
\end{aligned}$$

where $g = g(x)$, and $\mathcal{A}_\mu = A^a{}_\mu T^a$.

Proceeding as in the abelian case, we choose a ground state $\left(A^{a(v)}_{\mu}, \boldsymbol{\varphi}^{(v)}\right)$, and consider excitations about it in order to get the spectrum of excitations of the theory. In what follows we choose a basis in which $\mu$ is diagonal, i.e $\mu_{ij} = \mu_i \delta_{ij}$, where $\mu_i$ are the eigenvalues of $\mu$, and $\mu_l = 0$ for $l = K+1, \cdots, N$. After a field redefinition and a gauge transformation, one can rewrite the Lagrangian 1.10 as

$$\mathcal{L} = \frac{1}{2}\partial_\mu \varphi'_k \partial^\mu \varphi'_k - \frac{1}{2}\mu_k^2 {\varphi'_k}^2 - \frac{1}{4}F^a{}_{\mu\nu}F^{a\mu\nu} + \frac{1}{2}M^2_{bc}A_\mu{}^b A^{c\mu} + \mathcal{L}_{\text{int}}; \tag{1.11}$$

where $k = 1, \cdots, n-(N-K)$, $b, c = 1, \cdots, N-K$; and the vector field mass matrix is given by

$$M^2_{bc} = e^2 (t'^b t'^c)_{ij} \varphi_{0i} \varphi_{0j}. \tag{1.12}$$

It follows that the spectrum of excitations is composed by:

- $n-(N-K)$ massive Higgs bosons, corresponding to the scalar fields $\varphi_k$,
- $N-K$ massive vector bosons, corresponding to the vector fields associated with the broken generators $t'^b$,
- $K$ massless vector bosons, corresponding to the vector fields associated with the unbroken generators $t^h$.

Notice that the $N-K$ would-be Goldstone bosons have disappeared. The corresponding degrees of freedom have been absorbed as the longitudinal degrees of freedom of the $N-K$ massive vector fields. We remark here that the Lagrangian 1.11 is gauge-invariant. However, if one tries to interpret the massive vector fields as gauge fields, then one erroneously concludes that the gauge invariance is gone. This fact explains the standard terminology: Spontaneous Symmetry Breaking.

*Glashow-Weinberg-Salam Theory:*

In the SM, the electroweak theory of Glashow-Weinberg-Salam illustrates the Higgs mechanism[5]. Within this model, the gauge group is $G = SU(2) \times U(1)$. Then, for the group $G$, the number of generators is $N = 4$. The Higgs field $\varphi$ is a scalar field doublet with respect to $SU(2)$, and has $U(1)$ charge $\frac{1}{2}$, corresponding to $n = 4$. The scalar-field potential is given by $V(\varphi) = \lambda \left(\varphi^\dagger \varphi - \frac{v^2}{2}\right)^2$, and determines the vacuum expectation value (in the unitary gauge) $\langle \varphi \rangle = \begin{pmatrix} 0 \\ \frac{v}{\sqrt{2}} \end{pmatrix}$. One can show that there is only one unbroken generator $Q$, and it generates the little group $H = U(1)_{\text{e.m.}}$. In consequence, the spectrum of the theory is composed of $K = 1$ massless vector boson, $n-(N-K) = 1$ massive Higgs boson, and $N-K = 3$ massive vector bosons. The massless vector boson corresponds to the photon field $A_\mu$, while the massive vector bosons correspond to the $W^\pm$, and $Z$-boson fields. These bosons, including the Higgs boson, have been detected experimentally. Their masses are $m_W = 80$GeV, $m_Z = 91$GeV and $m_h = 125$GeV. As a final remark, the Higgs field also couples to fermionic fields through a Yukawa coupling. After symmetry breaking, these couplings give rise to the mass terms in the Lagrangian for the fermions, hence, the Higgs mechanism is said to explain how the fields acquire mass in the SM.

*Motivations for GUT:*

The SM is characterised by three coupling constants $g_s$, $g$, and $g'$. Due to radiative corrections, the coupling constants depend on the energy scale $q$ as well as their "fine structure constants" $\alpha = g^2/4\pi$. In the case of the $SU(2)$ group, for $q > 100$GeV, all particles can be treated as massless, and hence the running of $\alpha_w$ is given by [6]

$$\alpha_w(q^2) = \frac{g^2}{4\pi} \approx \frac{\alpha_w(q_0)}{1 + 0.265\alpha_w(q_0)\text{Ln}(q^2/q_0{}^2)}$$

where $q_0 \sim 100GeV$ and $\alpha_w(q_0) \approx 1/29$. On the other hand, in the case of quantum chromodynamics the running of the strong fine structure constant is given by

$$\alpha_s(q^2) = \frac{g_s^2}{4\pi} = \frac{12\pi}{(11n - 2f)\text{Ln}(q^2/\Lambda_{QCD}{}^2)},$$

where experimental data suggest that $\Lambda_{QCD} \approx 220$MeV. $f = 5$ is the number of massless flavors, and $n = 3$ the number of colors. Comparing $\alpha_w$ and $\alpha_s$, one finds that the coupling constants meet at $q \sim 10^{17}$GeV. This observation suggest that above $10^{17}$GeV, the strong and weak interactions may be unified in a large gauge group $G$, characterized by a single coupling constant $g_U$. Then, the different running for $g_w$ and $g_s$ is explained by the running within the $SU(3)$ and the $SU(2)$ subgroups, after the symmetry breaking of the larger group $G$ at $10^{17}$GeV.

*Georgi-Glashow Model:*

The smallest extension of the SM, that incorporates the whole spectrum is given by the simple group $SU(5)$. However, measurements of the proton lifetime and bounds on the neutrino masses rules out the minimal $SU(5)$ model as a realistic theory. Nevertheless, to explain the common features of GUT, we will consider this model as an example.

The $SU(5)$ group has $N = 24$ generators which correspond to 24 Gauge fields. It is possible to identify 8 of them with the generators of $SU(3)$, corresponding to the gluons fields; and 3 generators with the generators of the $SU(2)$ subgroup, and 1 generator with the $U(1)$ generator, corresponding to the electroweak interactions[5]. The 12 remaining bosons form two charged coloured triplets $X_i^{\pm 4/3}$, and $Y_i^{\pm 1/3}$, where $i = 1, 2, 3$ is the color index and the upper index corresponds to the electric charge. After the symmetry breaking $SU(5) \to SU(3) \times SU(2) \times U(1)$, the vector bosons $X$, and $Y$ acquire masses of order $10^{15} - 10^{17}$GeV. Then, bellow this energy scale, transitions between the $SU(2)$ and $SU(3)$ are exponentially suppressed. This behaviour is common to all GUT that undergo a phase transition associated to the spontaneous breaking of a unified group $G$.

### 1.1.1. Phase transitions and spontaneous symmetry breaking

Up to now, in the discussion of symmetry breaking and Higgs mechanism we have considered purely classical scalar field potentials to determine the vacuum expectation value of a Higgs field $\varphi$. Although this approximation simplifies the discussion, the reality is that quantum, and finite temperature effects should be taken into account.

Since $\varphi$ is a quantum field, radiative corrections modify the classical potential $V(\varphi)$. The radiative corrections are due to self-interactions, and interactions with other quantum fields. The corrected potential is known as the effective potential. Besides, at non-zero temperature, the expectation value of the Higgs field can be thought of as describing a Bose condensate of Higgs particles immersed in a thermal bath of various particles and antiparticles. Assuming that the particle masses are proportional to the Higgs expectation value, the free energy of the system,

$$F = E - TS \tag{1.13}$$

is a function of $\varphi$. Thus, the equilibrium value of $\varphi$ is found by minimizing the free energy, and is temperature-dependent[4].

At low temperature, the second term of the right-hand side of 1.13–$TS$–is negligible, and the equilibrium value of $\varphi$ tends to a ground state $\varphi^{(v)}$, which minimises the energy–$E$. On the other hand, at high temperatures, the entropy term becomes more relevant than the energy term. Thus, the free energy is minimized if the entropy is increased. This occurs when the available phase space becomes larger. For massive particles, the phase space is inversely proportional to the mass, and since the particle masses are proportional to the Higgs expectation (or equilibrium) value, then there is a tendency for the Higgs field to decrease as a function of temperature. As a consequence, above some critical temperature $T_c$ the Higgs expectation value vanishes, and the symmetry is said to be restored at high temperatures. Most of our experience with macroscopic systems suggest that the low-temperature phase has less symmetry than the high-temperature phase. However, different models can be constructed in which a broken symmetry at high temperatures can be restored at low temperatures. An example of such models, described by Weinberg in [7], is the model of two $n$-vectors with $\mathcal{O}(n) \times \mathcal{O}(n)$ global symmetry.

At zero temperature, one can evaluate the effective potential perturbatively as an expansion in powers of coupling constants,

$$V_{\text{eff}}(\varphi) = V(\varphi) + V_1(\varphi) + V_2(\varphi) + \cdots$$

where $V_n(\varphi)$ is the contribution of Feynman diagrams with $n$ closed loops. Depending on the model, radiative corrections are negligible, or can modify completely the character of symmetry breaking. At finite temperatures, it was found that the free energy density–$\mathcal{F}$–is given by the same diagrammatic expansion as the effective potential $V_{\text{eff}}(\varphi)$ with all the Green's functions replaced by finite-temperature Green's functions [4][7][8]. This is the reason why the free energy per unit volume is called the finite-temperature effective potential, $\mathcal{F}(\varphi, T) = V_{eff}(\varphi, T)$.

*The abelian-Higgs model, revisited*

As an example, following [4], we consider the abelian-Higgs model described by the Lagrangian 1.1, and quadratic potential

$$V(\varphi) = \mu_0^2|\varphi|^2. \tag{1.14}$$

The symmetry breaking in this model is induced by radiative corrections. The one-Loop contribution to $V_{\text{eff}}$ was computed [9] to be

$$V_1(\varphi) = \frac{\mu_0^2}{\nu_0\sigma^2}|\varphi|^4 \ln\left(\frac{|\varphi|^2}{\sigma^2}\right),$$

where $\sigma$ is the renormalization scale, and

$$\nu_0 = \frac{16\pi^2\mu_0^2}{3e^4\sigma^2} \tag{1.15}$$

is a dimensionless quantity. The corresponding effective potential is known as the Coleman-Weinberg potential

$$V_{eff}(\varphi) = \mu_0^2|\varphi|^2 + \frac{\mu_0^2}{\nu_0\sigma^2}|\varphi|^4 \ln\left(\frac{|\varphi|^2}{\sigma^2}\right). \tag{1.16}$$

The figure 1.1 shows the shape of the effective potential for different values of $\nu_0$. One can show that for $\nu_0 > 0.447$ the effective potential has a single minimum at $\varphi = 0$. For $\nu_0 < 0.447$, the effective potential has another minimum for $|\varphi| \neq 0$. Moreover, for $\nu_0 < 0.367$ the global minimum of the effective potential is at $|\varphi| \neq 0$, and the symmetry is spontaneously broken. In what follows, we assume that $\nu_0 < 0.367$, i.e. at zero temperature, the effective potential breaks the symmetry.

At high temperatures $T$, such that $e|\varphi| \ll T$, the finite-temperature effective potential is given by[4]

$$V_{eff}(\varphi, T) = m^2(T)|\varphi|^2 + \frac{\mu_0^2}{\nu_0\sigma^2}|\varphi|^4 \ln\left(\frac{|\varphi|^2}{\sigma^2}\right), \tag{1.17}$$

where $m^2(T) = \mu_0^2 + \frac{1}{4}e^2T^2$. In order to study the behaviour of this potential, we introduce the dimensionless temperature-dependent quantity

$$\nu(T) = \frac{16\pi^2 m^2(T)}{3e^4\sigma^2} = \nu_0 + \frac{4\pi^2}{3}\left(\frac{T}{e\sigma}\right)^2.$$

The figure 1.2 shows the behaviour of the effective potential 1.17 for $\nu_0 = 0.25$ at different temperatures. The behaviours (a) and (b) correspond to very high temperatures. If $T > T_1$, where $\nu(T_1) = 0.447$, then $V_{eff}(\varphi, T)$ is dominated by the $\frac{1}{4}e^2T^2|\varphi|^2$ term, and has a unique minimum at $\varphi = \varphi_0 = 0$. In this case the symmetry is said to be restored at high temperatures. Notice that, as a consequence, the gauge boson $A_\mu$ is effectively massless. (c) in figure 1.2 shows the behaviour of $V_{eff}\,(\varphi, T_1)$.

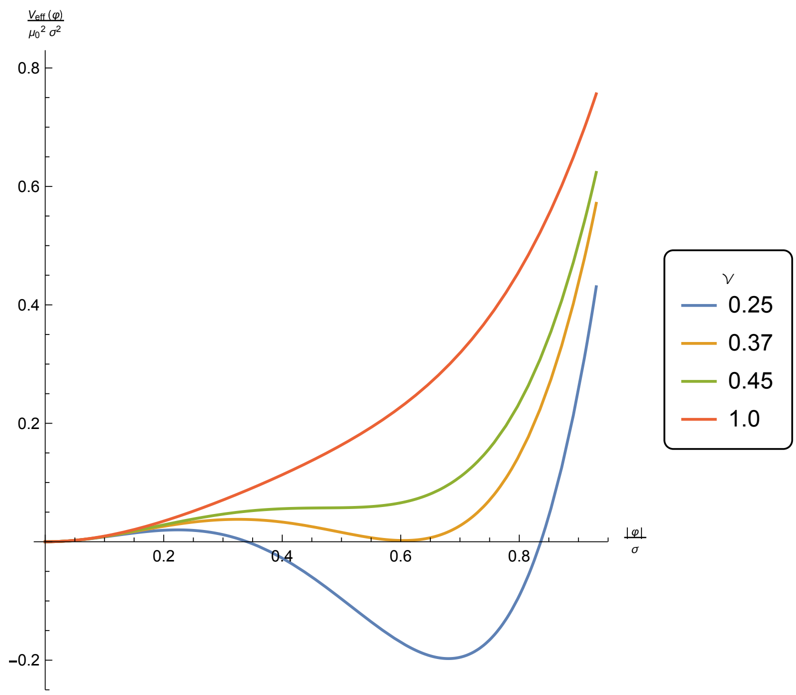


Figure 1.1.: Coleman-Weinberg effective potential 1.16 for different values of the parameter $\nu_0$.

When the temperature drops bellow $T_1$, a second minimum of the potential at $\varphi = \varphi_1 \neq 0$ appears, as shown by (d) of figure 1.2. Notice that the value of the Higgs field at the second minimum is temperature-dependent, $\varphi_1 = \varphi_1(T)$. Moreover, one can show that $\varphi_1(T)$ is a monotonic decreasing function. Further, the value of $V_{eff}(\varphi_1, T)$ decreases as the temperature decreases. As a consequence, there exists a critical temperature–$T_c$–such that the two minimum become equal, i.e

$$V_{eff}(\varphi_0, T_c) = V_{eff}(\varphi_1, T_c). \tag{1.18}$$

The behaviour of $V_{eff}(\varphi, T_c)$ is shown by (e) of figure 1.2. Similarly to the analysis of the Coleman-Weinberg potential, a first estimate for the critical temperature is given by $\nu(T_c) = 0.367$, which correspond to $T_c \approx \sqrt{\frac{4\pi^2}{3}(0.367 - \nu_0)}e\sigma$. However, the effective potential expansion 1.17 is not valid at $\varphi \sim \sigma$ and $T \sim T_c$, and a more detailed analysis is required[8][6][4]. Nevertheless, this detailed description of the critical temperature is not required for our discussion.

Below the critical temperature, $T < T_c$, corresponding to the behaviour (f) of figure 1.17, the minimum of the effective potential at $\varphi_1$ becomes a global minimum. As a consequence, the symmetry is spontaneously broken, and as seen before, the vector boson acquires mass via the Higgs mechanism. Finally, at zero-temperature, $T = 0$, the effective potential is given by the Coleman Weinberg potential, 1.16, and its behaviour is shown by (g) of figure 1.17.

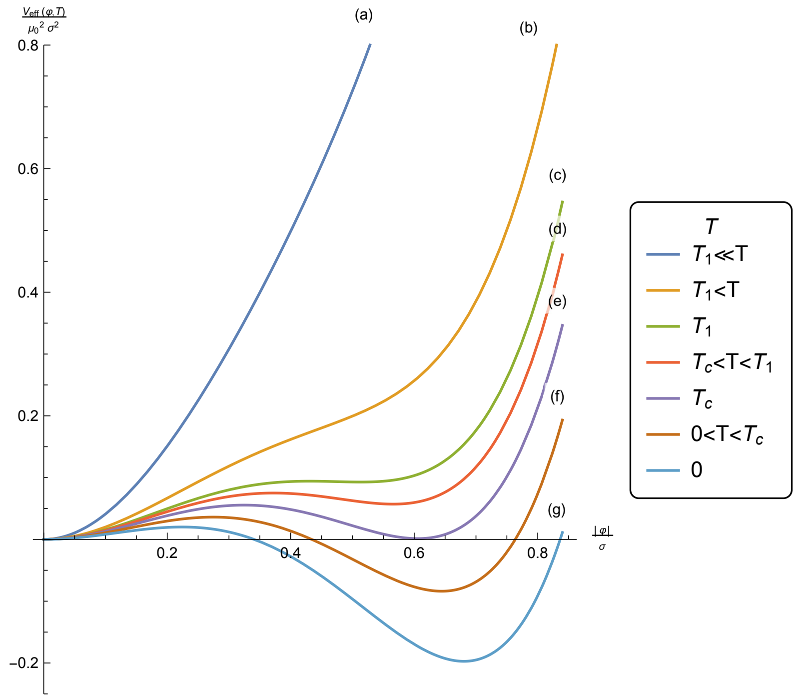


Figure 1.2.: Finite temperature effective potential 1.17 for fixed parameter $\nu_0$. The (a)-(f) behaviours corresponds to different temperature $T$ regimes: (a) and (b) corresponds to $T > T_1$, (c) to $T = T_1$, (d) to $T_1 > T > T_c$, (e) to $T = T_c$, (f) to $T_c > T > 0$, and (g) to $T = 0$. In this figure, $\nu_0 = 0.25$ is fixed. $T_1$ and $T_c$ are estimated to be $T_1 = 0.12e\sigma$, and $T_c = 0.095e\sigma$.

### Coulomb, Higgs, and Landau phases

The abelian-Higgs model 1.1 is a particular case of quantum electrodynamics. Depending on the details of the matter sector, quantum electrodynamics exhibit three different dynamical regimes[10], or *phases*[3]. We summarise the most important properties of these three different phases bellow.

- The **Coulomb Phase**, also known as the symmetric phase, corresponds to the regime in which the gauge field is massless. Consequently, two (static) probe electric charges, separated a distance $R$, will experience a Coulomb-like interaction with potential $U(R) \sim e^2(R)/R$. Classically, $e(R)$ is the probe particles charge, and it is constant. On the other hand, quantum corrections, due to loops of virtual particles of mass $m > 0$, make $e(R)$ run according to the Landau formula. At large distances $e^2(R) \sim 1/\ln R$. If $m$ is finite, then $e^2(R)$ is frozen at ${e_*}^2 = e^2(m^{-1})$, and the long-range interaction becomes $U(R) \sim {e_*}^2/R$.

[3]These regimes are also admitted in non-abelian gauge theories. However, non-abelian theories exhibit more dynamical regimes that are not discussed in the present work

- The **Higgs Phase**, also known as the broken phase, corresponds to the regime in which all excitations are massive. In the case of the abelian-Higgs model, this phase is realized when the expectation value of the Higgs field is non-zero, $\langle \varphi \rangle \neq 0$. Two probe (static) electric charges, separated a distance $R < m_v^{-1}$, will experience an interaction with a Coulomb-like potential $U(R) \sim e^2(R)/R$, where the gauge coupling $e(R)$ runs according to the Landau formula. For $R > m_v^{-1}$, $e(R)$ is frozen at $e(m_v^{-1})$, and the particles experience a Yukawa-like potential $U(R) \sim \mathrm{e}^{-m_v R}/R$. As a consequence, at large distances, there is no long-range interaction between charges.

- The **Landau zero-charge phase**, also known as an infrared-free phase, corresponds to the regime in which the gauge field, and the virtual particles are massless, $m = 0$. In this case, $e^2(R)$ does not freeze, and $e^2(R) \to 0$ as $R \to \infty$. Although this theory has no localized asymptotic states, nor $S$ matrix, it is well defined in a finite volume.

*Phase transitions*

*First-order phase transitions*

Returning to our example, the abelian-Higgs model with potential 1.14 and $\nu_0 < 0.367$, the system is present in different dynamical regimes depending on the temperature $T$. We remark here that, since we assume $\mu_0 \neq 0$, the Landau zero-charge phase is not admitted in this model. Above $T_c$, the symmetry is not broken, and the system is in the Coulomb phase. At $T = T_c$, the Coulomb and Higgs phases are both equally energetically favourable, and both phases can be present in the system in different regions of space. These regions, for reasons that we will discuss in the next section, are referred to as bubbles and are separated by Domain Walls. As the temperature decreases below $T_c$, the minimum $\varphi_1$ becomes deeper and the expectation value of the Higgs field can change from $\varphi_0$ to $\varphi_1$. In our example, as it can be seen in figure 1.2, the two minimum of the potential are separated by a potential barrier. In this case, the transition $\varphi_0 \to \varphi_1$ occurs via bubble nucleation[6][4]. If the bubble nucleation rate is big enough[4], the bubbles collide and eventually fill all space. As a consequence, the system undergoes a phase transition from the Coulomb phase to the Higgs phase.

The phase transition in the abelian-Higgs model is an example of first-order phase transitions. In general, this process is violent, and large deviations from thermal equilibrium are expected. Another typical characteristic of first-order phase transitions is that the symmetric phase remains metastable bellow the critical temperature. The metastable vacuum state, at $\langle \varphi \rangle = 0$ in the abelian-Higgs model, is referred to as "false vacuum". The false vacuum decay occurs via two different mechanisms. Firstly, if the temperature at the time of the transition is small compared to the potential barrier height, the transition occurs as a result of quantum tunnelling. On the other hand, if the temperature is bigger than the barrier, the transitions $\varphi_1 \to \varphi_0$ are classical and their

[4]More precisely, if we take into account the expansion of the universe, the bubble nucleation rate should be bigger than the universe's expansion rate.

rate is determined by static field configurations known as sphaleron.

*Second-order phase transitions*

On the other hand, second-order phase transitions are characterised by the fact that the order parameter (the vacuum expectation value $\langle\varphi\rangle$, in the case of the abelian-Higgs model) increases continuously as the temperature is decreased below the critical temperature. For completeness, we present here an example of such transition: the Goldstone model. It can be recovered from the abelian-Higgs model if we set $e = 0$ and consider the potential 1.2. As discussed in [4], the finite-temperature effective potential is given by

$$V_{eff}(\varphi, T) = m^2(T)|\varphi|^2 + \frac{\lambda}{4}|\varphi|^4,$$

where $m^2(T) = \frac{\lambda}{12}\left(T^2 - 6v^2\right)$, and $\varphi$ independent terms are omitted. The critical temperature is $T_c = \sqrt{6}v$. When $T > T_c$, the potential has a unique minimum at $\varphi_0 = 0$, and the symmetry is restored. Bellow the critical temperature, at $T < T_c$, the potential has a minimum at $\varphi_1 \neq 0$, and the symmetry is spontaneously broken. It follows that $|\varphi_1| = \frac{1}{\sqrt{6}}(T_c^2 - T^2)^{1/2}$, and that $\varphi_1 \to \varphi_0$ as $T \to T_c$. In addition, one can show that the two minimum $\varphi_0$ and $\varphi_1$ are never separated by a potential barrier, and that the transition $\varphi_0 \to \varphi_1$ is smooth.

*Phase transitions in the SM and GUT*

In the SM, the electroweak phase transition is a cross-over with no dramatic cosmological consequences, and no large deviations from the thermal equilibrium are expected. On the other hand, first-order phase transitions are pretty common in different GUT[4]. In general, critical temperatures are determined by the energy scale at which a symmetry breaking takes place. Thus, a Grand Unified Theory with a sequence of symmetry breaking

$$G \to H \to \cdots \to SU(3) \times SU(2) \times U(1) \to SU(3) \times U(1)_{\text{em}},$$

predicts a series of critical temperatures $T_{ci}$, corresponding to the scale of symmetry breaking due to the condensation of a Higgs-like field $\varphi_i$. In a cosmological context, when the universe cools bellow a certain $T_{ci}$, the field $\varphi_i$ acquires and expectation value $\langle\varphi_i\rangle \neq 0$. The magnitude of $\langle\varphi_i\rangle$ is determined by the scalar field potential. However, the orientation of $\langle\varphi_i\rangle \neq 0$ in the field space, i.e. the corresponding point in the vacuum manifold $\mathcal{M}$, is not fixed by any local physics.

For instance, in the abelian-Higgs model, the orientation of $\langle\varphi\rangle \neq 0$ in the field space is determined by its phase $\alpha(x)$ (see equation 1.4). The choice of $\alpha(x)$ depends on random fluctuations and takes different values in different regions of space, where the system is in the broken phase. Spatial variations of $\alpha(x)$ will gradually disappear since the free energy is minimized by and homogeneous field $\varphi$. Above certain correlation length scale $\xi(t)$, the values of $\alpha(x)$ are uncorrelated. Causality requires $\xi(t)$ to be smaller than the causal horizon,$d_H$. If one assumes that the universe is homogeneous and isotropic, its metric is given by the Friedmann-Robertson-Walker metric, and the causality bound of $\xi(t)$ can be rewritten in terms of the scale factor $a(t)$ as

$$\xi(t) < d_H(t) = a(t)\int_0^t \frac{dt'}{a(t')}.$$

We conclude that–for length scales bigger than the causal horizon $d_H$–the spatial variations of the VEV $\langle\varphi(x)\rangle$ is responsible for the formation of non-trivial field configurations[11]. These configurations are known as topological defects, and we expand on them on the next section.

## 1.2. Topological defects

In general, topological defects arise in models whose vacuum manifold $\mathcal{M}$ has a non-trivial topology. In order to be more precise, lets go back to, by now well known example, the abelian-Higgs model with scalar potential 1.2. As a first step, lets simplify further the discussion while considering the Goldstone model (i.e. let $e = 0$, and $\varphi$ to be real) in $(1+1)$ dimensions. Thus, the corresponding field equation for $\varphi$ simplifies to

$$\Box_{1+1}\varphi + \frac{\partial V(\varphi)}{\partial\varphi} = 0, \tag{1.19}$$

where the minimum of the quartic scalar potential $V(\varphi)$ is degenerate at $\varphi = \nu$, and $\varphi = -\nu$. An static solution to the field equation 1.19, that asymptotically interpolates between these two minimum, is given by

$$\varphi_k(x) = \nu\tanh\left(\sqrt{\frac{\lambda}{2}}\nu x\right) = \frac{m_h}{\sqrt{\lambda}}\tanh\left(\frac{m_h}{\sqrt{2}}x\right). \tag{1.20}$$

This solitonic solution is known as *kink* and is shown in figure 1.3. The corresponding energy density is given by [3]

$$\epsilon(x) = \frac{\lambda\nu^4}{2}\frac{1}{\cosh^4\left(\sqrt{\frac{\lambda}{2}}\nu x\right)} = \frac{m_h^4}{2\lambda}\frac{1}{\cosh^4\left(\frac{m_h}{\sqrt{2}}x\right)}.$$

Notice that, $\epsilon(x) \sim \frac{m_h^4}{4\lambda}\mathrm{e}^{\mp 2\sqrt{2}m_h x}$ for $x \to \pm\infty$. Thus, $\epsilon(x)$ is significantly different from zero only if $|x| \lesssim r_k \sim m_h^{-1}$. It follows that the size of the kink is of order $r_k$, which is comparable to the Compton wavelength of an elementary excitation. Integrating $\epsilon(x)$, we get the total energy $M_k = \frac{2\sqrt{2}}{3}m_h\nu^2 = \frac{2\sqrt{2}}{3}\frac{m_h^3}{\lambda}$. In the weakly coupled regime $\lambda \ll m_h^2$, thus $m_h \ll M_k$. Then the Compton wavelength corresponding to the energy of the kink, $\lambda_k = {M_k}^{-1}$, is much smaller than the classical size of the kink $r_k$, i.e.

$$\frac{r_k}{\lambda_k} \sim \nu^2 = \frac{m_h^2}{\lambda} \gg 1.$$

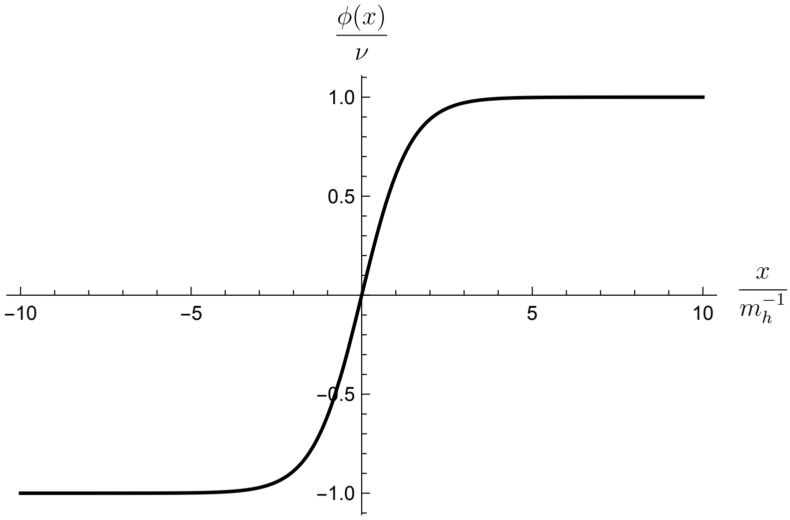


Figure 1.3.: Kink profile 1.20

Consequently, a kink is essentially a classical object, even in quantum theory[12].

The solution 1.20 is centred about $x = 0$, and it is not invariant under spatial translations, $x_\mu \to x_\mu - x_{0\mu}$, nor boost transformations, $x_\mu \to \Lambda_{\mu\nu}(u)x^\nu$. However, the transformed field configuration

$$\varphi_{(x_0,u)}(t,x) = \frac{m_h}{\sqrt{\lambda}}\tanh\left(\frac{m_h}{\sqrt{2}}\gamma_u((x-x_0)-ut)\right), \tag{1.21}$$

where $\gamma_u = (1-u^2)^{-\frac{1}{2}}$, is also a solution to the field equations. The new solution $\varphi_{(x_0,u)}$ is centred around $x_0 + ut$. Thus, $u$ represents the velocity of $\varphi_{(x_0,u)}$, and $\gamma_u$ is the corresponding Lorentz factor. Further, one can show that the corresponding energy is $M_{(x_0,u)} = \gamma_u M_k$. The solutions $\varphi_{(x_0,u)}$ are known as boosted kinks.

Another remarkable property of kink solutions is that they are non-dissipative solutions. The classical stability can be established by a perturbative analysis[12]. However, in a more fundamental sense, topological defects stability arises from a topological conservation law. As a first stage, lets define the topological current $k^\mu$ for the $(1+1)$ Goldstone model as

$$k^\mu = \frac{1}{2\nu}\epsilon^{\mu\nu}\partial_\nu\varphi,$$

where $\epsilon^{\mu\nu}$ is the anti-symmetric tensor with $\epsilon^{01} = 1$. It follows immediately that $\partial_\mu k^\mu$, so $k_\mu$ is conserved. The associated conserved topological charge, for a given field configuration is

$$Q_T = \frac{1}{2\nu}\int_{-\infty}^{\infty} dx k^0 = \frac{1}{2\nu}\varphi(t,x)|_{x=-\infty}^{x=\infty}.$$

Any field configuration $\varphi(t,x)$, such that it is a solution to the field equations and has finite energy, should satisfy

$$\lim_{x\to\pm\infty} x\epsilon[\varphi(t,x)] = 0,$$

where $\epsilon[\varphi] = \frac{1}{2}(\partial_0\varphi)^2 + \frac{1}{2}(\partial_1\varphi)^2 + V(\varphi)$. This condition is satisfied if, and only if, the field configuration approaches sufficiently fast [5] one of the vacuum configurations. In other words,

$$\begin{aligned} \varphi_+ &\equiv \lim_{x\to\infty} \varphi(t,x) = \pm\nu, \\ \varphi_- &\equiv \lim_{x\to-\infty} \varphi(t,x) = \pm\nu, \end{aligned} \tag{1.22}$$

for all times $t$. This conditions separates the space of possible solutions in four disconnected sectors characterized by the asymptotic behaviour of the solutions. The four possible asymptotic behaviour are $\{\varphi_+ = \nu, \varphi_- = \nu\}$, $\{\varphi_+ = -\nu, \varphi_- = -\nu\}$, $\{\varphi_+ = \nu, \varphi_- = -\nu\}$, $\{\varphi_+ = -\nu, \varphi_- = \nu\}$. The vacuum states $\varphi(x,t) = \nu$ and $\varphi(x,t) = -\nu$ have zero topological charge, $Q_T = 0$, and belong to the first and second sectors, respectively. The boosted kinks $\varphi_{(x_0,u)}$ have non-zero topological charge $Q_T = 1$, and belong to the third sector. The anti-kink configuration given by $\varphi(x) = -\varphi_k(x)$ belongs to the fourth sector and has topological charge $Q_T = -1$.

Notice that, due to 1.22, the time evolution of a solution can not change the sector to which it corresponds. This fact can be understood in terms of energy constraints. If such a smooth transition from one sector to another is possible, it would require an infinite amount of energy to lift the field configuration, near one of the two spatial infinities, over the potential barrier separating the two vacuum state. However, in a finite volume, such transitions are allowed although are exponentially suppressed.

We conclude the discussion of the Goldstone model by describing the relation between the existence of kink solutions and the topology of the vacuum manifold. The vacuum manifold is given by $\mathcal{M} = \{\varphi | V(\varphi) = 0\}$, where we assume the (global) minimum of the scalar potential to be at 0. For the potential 1.2 $\mathcal{M} = \{\nu, -\nu\}$, and we observe that each sector can be associated to a map $f : S^0 \to \mathcal{M}$, where $S^0 = \{-1, +1\}$ is the zero-sphere, if we identify $f(\pm 1) \equiv \varphi_\pm$. Fixing $\nu$ as a base point, i.e. $f(1) = \nu$, then $f(-1) = \pm\nu$. This condition determines that there are only two equivalence classes under homotopy. These classes are known as homotopy classes[3]. We denote the homotopy class of $f$ by $[f]$. The set of homotopy classes of maps with base point $x \in \mathcal{M}$ is known as the zero-homotopy group $\pi_0(\mathcal{M}, x)$. Notice that each homotopy class $[f] \in \pi_0(\mathcal{M}, x)$ corresponds to a different connected component of $\mathcal{M}$. In general, for all $x \in \mathcal{M}$, one identifies $\pi_0(\mathcal{M}) \equiv \pi_0(\mathcal{M}, x)$ with the set of disconnected components of $\mathcal{M}$.

This criteria for existence of kinks in the Goldstone model can be generalised as follows. The key points are that $V(\varphi)$ has multiple degenerate vacuum, and that the field configuration approaches different vacuum at the spatial infinity. In $d+1$ dimensional spacetimes, the spatial infinity can be identified with the $S^{d-1}$ sphere. Since the fields approach at infinity certain configuration corresponding to a point in the vacuum manifold $\mathcal{M}$, a field configuration can be associated to a function $f : S^{d-1} \to \mathcal{M}$. Notice that different field configurations can be associated to the same function $f$. When

[5] More precisely, there exist a distance $y$, such that $|\partial_i\varphi| < |x|^{-1}$ for $y < |x|$

a field configuration[6], associated to $f_1$, can be smoothly deformed into other field configuration, corresponding to $f_2$, via a symmetry transformation, one can show that $f_1$ and $f_2$ are in the same conjugacy class of the homotopy group $\pi_d(\mathcal{M})$[4]. If $\pi_d(\mathcal{M}) = 0$, then any field configuration can be deformed smoothly into any other field configuration via a symmetry transformation. On the other hand, when $\pi_d(\mathcal{M})$ is not trivial, there are solitonic field configurations that can not be deformed to a field configuration of homogeneous vacuum.

Because of this intertwining of the topology of the vacuum manifold $\mathcal{M}$ with the topology of spatial infinity, $S^{d-1}$, the resulting solitons are known as topological defects. In the following section we discuss the Kibble–Zurek mechanism[11], which explains how topological defects can be formed.

### 1.2.1. The Kibble–Zurek mechanism

In theories that undergo a phase transition, associated to a spontaneous symmetry breaking pattern $G \to H$, a Higgs-like field acquires a certain vacuum expectation value $\langle \phi \rangle$ corresponding to a point of the vacuum manifold $\mathcal{M}$. the VEV $\langle \phi \rangle$ does not need to be constant over spacetime. Moreover, as we mention before, the orientation of the Higgs condensate appear in a random fashion in causally disjointed points[7]. Depending on the topology of $\mathcal{M}$, we have the following cases:

- If $\pi_0(\mathcal{M}) \neq 0$, two neighbouring causally disconnected volumes can develop a VEV corresponding to different disconnected components of the vacuum manifold (probably corresponding to different phases of the theory). Therefore, there will exist a transitional region between these two volumes where the VEV will interpolate between the two VEV. In a cosmological context, as we mention in section 1.1.1, in $(3+1)$ dimensions, the transitional region is an extended object, whose energy is concentrated near two-dimensional surfaces, the so called *Domain Walls*[13].

- If $\pi_1(\mathcal{M}) \neq 0$, three neighbouring causally disconnected volumes can develop the VEVs $\varphi_1$, $\varphi_2$, and $\varphi_3$. We assume here that $\mathcal{M}$ is connected, so that no pair of volumes are separated by a Domain Wall. The VEV $\langle \varphi \rangle$ in the transition region between the three volumes should interpolate between $\varphi_1$, $\varphi_2$, and $\varphi_3$. If $\langle \varphi \rangle$ can not be smoothly deformed to a homogeneous vacuum, then a region of symmetric phase will be trapped along the edge. In this case, the energy in the transitional region is concentrated near a one dimensional extended object, known as *cosmic string*.

- If $\pi_2(\mathcal{M}) \neq 0$, a similar argument goes trough for four neighbouring causally disconnected volumes developing the VEVs $\varphi_1$, $\varphi_2$, $\varphi_3$, and $\varphi_4$. The VEV $\langle \varphi \rangle$

[6]Here we assume a certain base point $x \in \mathcal{M}$. If $d > 1$, and $\mathcal{M}$ is not connected, we restrict $\mathcal{M}$ to be the connected component of $x$. For details see section 3.3 of [4]

[7]More precisely, there exist a correlation length $\xi < d_H$ such that, if the distance between the spacetime points x and y is larger than $\xi$, then $\langle \phi(\mathrm{x}) \rangle$ and $\langle \phi(\mathrm{y}) \rangle$ are independent.

in the transition region around the vertex where the four volumes meet, should interpolate between $\varphi_1$, $\varphi_2$, $\varphi_3$, and $\varphi_4$. If $\langle\varphi\rangle$ can not be smoothly deformed to a homogeneous vacuum, then a region of symmetric phase will be trapped around the vertex. In this case, the energy in the transitional region is concentrated near one point. These field configurations are known as *monopoles*.

In this way topological defects can be formed during a phase transition. In addition, the existence of stable topological defects is constrained by Derricks theorem [14]. It states that for $d \geq 1$, there are no stable time-independent, localized solutions to the field equations. This result also applies for the case when the Higgs field is composed by $n$ real scalar fields. For gauge theories, the theorem prohibits the existence of non-trivial static classical solutions for $d \geq 4$. However, this obstruction to construct solitonic solutions can be avoided in various different ways, for example, by adding higher derivative terms as in the Skyrme model[15][4], allowing time-dependence of the solution, relaxing the localisation assumption, or considering curved backgrounds [16].

### 1.2.2. Domain Walls, Cosmic Strings, and Monopoles

In this section we present the most relevant characteristic of topological defects for our discussion.

*Domain Walls:* Since energy should be finite, the total area of a Domain Wall should be finite, constraining the wall to be curved–reason why they are also referred to as bubbles[8]. In the case of the real Goldstone model in $(d+1)$ dimensions spacetime, the kink profile 1.20 gives a solution to the field equations $\varphi_k(x_1)$, which depends only on one coordinate. This solutions represent an infinite planar Domain Wall, which would have infinite energy. However, if the curvature of a bubble, $R$, is much bigger than the size of the kink, $R \gg r_k$, then the field profile in the transition region can be approximated by $\varphi_k(r)$. As a consequence, the total energy, $M_k = \frac{2\sqrt{2}}{3}\frac{m_h^3}{\lambda}$, should be interpreted as the Domain Wall tension $\sigma$. For $d = 2$ it has units of energy per unit length, while for $d = 3$ it has units of energy per unit area.

Further, the area of the Domain Wall tends to decrease until the bubble collapses producing highly radiative processes [17]. Zel'dovich et al. concluded that for weakly coupled regime, $\lambda < 1$, the Domain Walls are so heavy that their existence would lead to a radical change of the cosmological evolution of the Universe[13]. If there is no mechanism that leads to the disappearance of domains at a sufficiently early stage of the evolution of the Universe, the domains would lead to conclusions which are in contradiction with observations. Current observations of the CMB have constrained the Domain Wall surface tension to be $\sigma < 3.85 \times 10^{-}9\mathrm{kg/m^2}$, which corresponds to an energy scale of formation for Domain Walls of 0.93MeV [2].

[8]It is also possible that bubbles have boundaries, in the sense that they can terminate on other bubbles, or other topological defects, as it is discussed in [10]

*Vortex Lines and Cosmic Strings*

The vortex lines are part of the spectrum of theories whose vacuum manifold is not simply connected, for the abelian-Higgs model with scalar field potential 1.2. The string solutions are known as the Nielsen-Olesen cortex lines[18]. At large distances from the core

$$\varphi \sim \nu e^{in\theta},$$

where $n$ is an integer number, and $\theta$ is the polar angle. Meanwhile, the vector potential approaches

$$A_\mu \sim \frac{1}{ie}\partial_\mu \ln\varphi.$$

The energy density decreases exponentially away from the core. For $n = 1$, the width of the string is determined by two different scales: the vector core size $m_v^{-1}$, and the scalar core size $m_h^{-1}$. Along the vector core, there is a magnetic field $B$ corresponding to a total magnetic flux

$$\Phi_B = \frac{2\pi n}{e}, \tag{1.23}$$

which is proportional to the topological charge, or winding number,

$$n = \frac{1}{2\pi\nu^2}\oint dx^i \varphi^* \partial_i \varphi, \tag{1.24}$$

In the weakly coupling regime, the total string mass per unit length is approximately $\mu \sim \nu$. For GUTs with $\nu \sim 10^6$GeV, this corresponds to $\mu \sim 10^{22}$g cm$^{-1}$. In consequence, the strings have large energy density, and large tension. Thus, if the string is curved, it tends to contract acquiring relativistic velocities. The cosmological implications and dynamics are discussed in much detail in [4]

*Monopoles*

Monopoles arise in theories such that $\pi_2(\mathcal{M}) \neq 0$. In the case of a model with symmetry breaking $G \to H$, the vacuum manifold is $\mathcal{M} = G/H$, and the condition for monopoles existence is $\pi_2(G/H) \cong \pi_1(H) \neq 0$[9] An example of monopole solutions is given by the t'Hooft-Polyakov monopole. It arises in a model with a $SU(2)$ gauge symmetry, with a Higgs field in a triplet representation, $\varphi^a$, such that The VEV of the Higgs field breaks the gauge group to $U(1)$. Far from the core of the monopole, the Higgs field configuration approximates a 'hedgehog' configuration

$$\varphi^a = \nu x^a,$$

while the the vector field $A_\mu$ aligns such that the energy functional is minimized. As a result a radial magnetic field remains:

$$B_i = \frac{x_i}{ex_jx^j},$$

[9] Here $G$ is assumed to be a simply connected Lie group.

corresponding to a total magnetic flux,

$$\Phi_B = \frac{4\pi}{e}$$

which corresponds to a magnetic charge $g = \frac{4\pi}{e}$. In general, the magnetic charge $g_M$ is an integer multiple of $g$, $g_M = ng$. It is possible to show that $n$ is the degree of the mapping $f : S^2 \to \mathcal{M}$ characterising the Higgs field at spatial infinity, so it corresponds to a topological charge. As a consequence, the magnetic charge $g_M$ is topologically conserved.

Similar to the string case, the monopole has two characteristic lengths: $r_v \sim m_v^{-1}$ and $r_s \sim m_h^{-1}$, corresponding to the vector and scalar core, respectively. In the weak coupling regime, $\frac{\lambda}{e^2} \to 0$, the monopole mass can be estimated to be bigger than the BPS bound[4]

$$M_M \geq \frac{4\pi\nu}{e} = \frac{m_v}{\alpha_e},$$

where $\alpha_e = \frac{e^2}{4\pi}$, and the inequality is saturated for $\lambda = 0$. It follows that in the in weak coupling regime, the Compton wavelength of the monopole $\lambda_M = {M_M}^{-1} \leq \alpha_e m_v^{-1} \ll r_v$. Hence, to high accuracy monopoles can be treated as classical objects. For further details we refer the reader to chapter 9 of [3].

## 1.3. The cosmological monopole problem

In GUT, where a gauge group $G$[10] is broken to $H = SU(3) \times U(1)$, we have that

$$\pi_2(\mathcal{M}) \cong \pi_2(G/H) \cong \pi_1(H) \cong \pi_1(SU(3) \times U(1)) \cong \mathbb{Z}.$$

Thus monopole configurations are a common feature of GUTs. In general, monopoles can have magnetic charges corresponding to several different unbroken generators. However, for realistic monopoles, the colour-magnetic field is screened at $\Lambda_{QCD}$. Thus monopoles in GUTs, are usually refereed to as *magnetic monopoles*, and are expected to have a mass of order $M_M \sim M_X/\alpha_g \sim 10^{16}$GeV. The concentration of this heavy relic–also known as 't Hooft-Polyakov monopoles–in the early universe was first estimated by Zeldovich and Khlopov[19], and by Preskill [20] to be unacceptably large in comparison to observational bounds[11]. This tension indicated an incompatibility between the standard cosmology and GUT. This discrepancy is known as the cosmological monopole problem. Below we review some of the possible solutions to this problem.

In the inflationary universe scenario[21], there was a period of exponential expansion, and the observable universe aroused from a region which initially was smaller than

[10] $G$ is assumed to be a simply connected Lie Group. If $G$ is not simply connected, then the universal covering group of $G$ should be considered. This condition excludes the SM group $SU(3) \times SU(2) \times U(1)$, reason why there are no stable monopoles within it.

[11] See section 14.3.3 of [4].

the causal horizon. Thus, topological defects that formed before inflation are diluted until the universe is thermalized at a certain temperature $T$. In this way, less than one monopole per present horizon scale is left. This solution works only if the reheating temperature after inflation does not exceed the GUT scale, $10^1$6GeV. The present upper bound on the inflationary vacuum energy density is very close to the GUT scale[22]. This guarantees that the monopole problem can be solved by inflation. Langacker & Pi suggested another mechanism in which monopoles and anti-monopoles are connected by flux tubes, or strings[23]. The string pulls the pair together, and in consequence the annihilation efficiency is enhanced. However, this mechanism is highly sensible to the details of the Higgs structure of a specific model. Another, more radical, solution relies on non-restoration of the grand unified symmetry[24]. In this case, there was never a phase transition in which monopoles were produced. Lastly, another possible solution to the monopole problem was proposed by Dvali, Liu, and Vachaspati [25] in which the interaction between Domain Walls and magnetic monopole leads to the monopole erasure and the subsequent Domain Wall decay. We will describe this mechanism in more detail in the following chapter.

# 2. Erasure of Defects

## 2.1. Sweeping Away the Monopole Problem

The basic idea of this mechanism is that Domain Walls sweep away the magnetic monopoles and subsequently decay [25]. This mechanism requires that the phase transition that produces magnetic monopoles also produces Domain Walls. A Domain Wall accelerates and moves through space. then, when a monopole encounters a wall, it unwinds, and dissipates in the wall. In this way, the walls sweep away the monopoles from the universe. If the Domain Walls were stable, the monopole problem may have been replaced by a Domain Wall problem. However, at lower energy scale the walls can be unstable and hence collapse. This can be achieved in two different ways: the discrete symmetry responsible for the walls is chosen to be approximate, or, instanton effects violate discrete symmetry and destabilize the walls. The previous requirements ensure that Domain Walls do not dominate the universe but live long enough to solve the monopole problem. This mechanism was firstly discussed in the $SU(5)$ Grand Unified Theory[25]. In this GUT[5], the adjoint scalar field, $\Phi$, has the following potential

$$V(\Phi) = -\frac{1}{2}m^2\mathrm{Tr}\Phi^2 + \frac{h}{4}\left(\mathrm{Tr}\Phi^2\right)^2 + \frac{\lambda}{4}\mathrm{Tr}\Phi^4 + \frac{\gamma}{3}m\mathrm{Tr}\Phi^3.$$

The dimensionless parameter $\gamma$ characterizes an explicit violation of the $Z_2$ symmetry: $\Phi \to -\Phi$. In the case $\gamma = 0$, the scalar field $\Phi$ acquires a vacuum expectation value $\Phi_0$, and the spontaneous symmetry breaking

$$SU(5) \times \mathbb{Z}_2 \to \left[SU(3)_C \times SU(2)_L \times U(1)_Y\right] / \mathbb{Z}_6 \tag{2.1}$$

occurs. $\Phi_0$ is proportional to $v = m/\sqrt{\lambda'}$, where $\lambda' = h + 7\lambda/30$, and $\lambda$ are assumed to be positive. In the case $\gamma \neq 0$ the discrete symmetry $Z_2$ is explicitly broken. However, if $\gamma$ is small enough to have an approximate discrete symmetry, the VEV $\Phi_0$ still leads to the symmetry breaking pattern 2.1.

In both cases–$\gamma = 0$, and $\gamma \neq 0$–$Z_2$ Domain Walls interpolating between $\Phi_0$ and $-\Phi_0$, and $SU(5)$ monopoles arise during the phase transition associated to the symmetry breaking 2.1. If the Domain Walls sweep away the monopoles, and subsequently decay safely, one requires that:

- The Domain Walls never dominate the universe.
- The Domain Walls percolate, and there is a period during which their evolution is tension dominated[1]

[1] If the Domain Walls do not percolate, they will all be finite and will collapse without sweeping through the whole volume of the universe.

Imposing this conditions, the following constraints on the parameters of the Higgs scalar potential, $\lambda'$, and $\gamma$, were found[25]

$$10^{-19}{\lambda'}^{-1/2} \lesssim \gamma \lesssim 10{\lambda'}^{1/2}.$$

In the case $\gamma = 0$, the $Z_2$ symmetry is expected to be broken by instanton contributions, if it is anomalous under a strongly coupled gauge group[26]. This violation leads to instability of the Domain Walls, and the requirement that they never dominate the universe can be meet. In this way, this mechanism is a plausible solution to the cosmological monopole problem. An important consequence of this resolution is that it allows inflation to occur before, during, or after the GUT phase transition. On the other hand, this mechanism suggests that interactions of topological defects produced during a phase transition can lead to defect 'erasure'.

A detailed investigation of the interaction of magnetic monopoles and Domain Walls in the $SU(5)$ model has been carried out by Brush, Pogosian, and Vachaspati [27][28] [29]. Following their discussion, a stable Domain Wall can have different orientations in the internal field space. After studying the interaction via numerical simulation, they found two different possibilities depending on the relative orientation in internal space. In the first case, the wall and the monopole resides in different non-overlapping blocks of field space. Thus, the interaction is weak, and only leads to a time delay or advance as the monopole goes through the wall. In the second case, the monopole resides in blocks of field space that overlap with those in which the wall resides. Thus, when the monopole hits the wall it unwinds, and its energy is transformed into radiation. These results suggest a scenario in which a Domain Wall allows certain monopole 'polarization' to pass through but not others. It is then possible that these interactions could lead to a universe that is free of magnetic monopoles. However, due to the several types of Domain Walls and monopoles that can arise, and the complexity in the dynamics, the evolution of defects after the grand unified phase transition remains uncertain.

## 2.2. DLV Mechanism

In general, the Dvali-Liu-Vachaspati solution to the cosmological monopole problem proposes that defect interactions can lead to the *Erasure of defects* during a phase transition. The defects erasure mechanism–or DLV mechanism–is supported by different investigations. We list some of them below

*Domain Walls and Monopoles in the $SU(5)$ GUT:*

The interactions of domain walls and monopoles in the $SU(5)$ GUT were consider by Vilenkin et al. in [27][28] [29]. Their results allowed them to conclude that, according to the classical evolution of the fields, a monopole can unwind within the Domain Wall, and its magnetic flux gets confined in the core of the wall. In this case the Domain Wall size is of order $\mathcal{O}({m_h}^{-1})$, and–depending on the orientation in internal field space–the $SU(5)$ symmetry can be fully restored inside its core. Thus, the unwinding process takes place inside the core of the wall. However, due to the several types of Domain Walls and monopoles that can arise, and the complexity in the dynamics, the evolution of defects after the grand unified phase transition remains uncertain.

*Monopoles and Domain Walls in $\mathcal{O}(3)$ sigma model:*

The interaction between monopoles, and Domain Walls was studied in a $\mathcal{O}(3)$ linear sigma model[30]. In this study, Alexander et al. simulated the interaction, and found that the monopole unwinds on the wall while the winding number spreads out on the surface.

*Skyrmions and Domain Walls in $\mathcal{O}(3)$ sigma model:*

Additionally, the interaction of Skyrmions with Domain Walls was considered in the nonlinear vector $\mathcal{O}(3)$ sigma model spontaneously broken to $\mathcal{O}(2) \times Z_2$ in $(2+1)$ dimensions[15]. In this model, waves carrying a topological charge can propagate on the wall. It was found that Skyrmions and Domain Walls attract each other leading to the absorption of Skyrmions by the walls and the creation of topological waves. Besides, under appropriate initial conditions, a Domain Wall can emit Skyrmions. In [31], a generalization to $(3+1)$ dimensions was considered. Similar to the lower-dimensional case, Kudryavtsev et al. showed that there is an attractive interaction between Skyrmions and Domain Walls, and established the existence of bound states between the defects. Further, these states are stable or unstable depending on the form of the mass term in the theory. If a bound state is unstable, its evolution leads to the capture of the Skyrmion which is then turned into topological waves that spread out on the wall.

*Vortices and Domain Walls in $^3$He:*

The interactions of topological defects have been studied also in $^3$He [32][33]. A-phase vortices and Domain Walls separating the A and B phases of $3^He$ have been investigated and observed experimentally. It is found that singular vortices do not penetrate from one phase into the other. The measurements show that the vortices experience a force from the advancing interface and are pushed as a vortex layer in front of it. A critical velocity has been identified, at which a vortex will leave the layer and will penetrate through the interface, transforming thereby into a new structure[34]. This behaviour exhibit the fact that that a A-phase vorticity is not able to cross the AB interface and is accumulated on the A-phase side of the interface such that it coats the interface with a dense vortex layer[35].

*Vortices and Coulomb Vacuum Layers in $\phi^6$-Model:*

The interactions of Vortices and Coulomb Vacuum Layers in $\phi^6$-Model lead to the unwinding of vortices. We discuss in the following sections and chapters, how the DLV-mechanism is confirmed for different parameters of the theory. In addition, within the $\phi^6$-model, one can investigate the dynamical behaviour of the fields in the core of a Coulomb Vacuum Layer, inside which the full symmetry is restored. In this way, we are able to study the DLV-mechanism in detail in a finite size region in which the unwinding process is allowed.

### 2.2.1. The $\phi^6$ Model

We will discuss the interaction of topological defects in the $\phi^6$-Model, we start by introducing the Lagrangian, and the different phases of the model. Following, we describe the spectrum of perturbations, and topological defects of the of model. In the following chapters, we describe the Vortices, Coulomb Vacuum Layers, their interaction and how it leads to the erasure of defects–the Vortices–bearing out the DVL-mechanism.

*The Model*

We consider a model with a $G$ gauge symmetry which is spontaneously broken by a Higgs field, $\phi$. We require the existence of topological defects–including Domain Walls–in the spectrum of the model, corresponding to different homotopy groups of the vacuum manifold. The Domain Walls may not necessarily be stable, but we required that they can form finite-size configurations that asymptotically interpolates two broken phases, such that it has a core inside which the full symmetry group $G$ is restored.

Lets consider the spacetime to have $(2+1)$ dimensions[2]. Further, let $G = U(1)$ be the gauge group. We denote the corresponding gauge field by $A_\mu$. The Higgs field is a complex scalar field, $\phi$. After the Higgs acquires a VEV $\langle\phi\rangle$ determined by the minimum of the scalar field potential $V(\varphi)$, we require that the Coulomb and the Higgs phase can be present simultaneously. In addition we require that it is possible to construct Domain Wall configurations interpolating between this two phases. In addition, in the Higgs phase, there arise other topological defects–vortexes in $(2+1)$ dimensions, or strings in $(3+1)$ dimensions. Consequently, the shape of the potential $V(\phi)$ is constrained to have a degenerate minimum at $\phi_0 = 0$ and at $\phi_1 = \nu \neq 0$. An example of a potential with such behaviour is shown by (e) of figure 1.2–it corresponds to the finite temperature effective potential at critical temperature $T_c$.

The minimal-degree polynomial potential $V(\phi)$ that fulfils the previous considerations turns out to be the sextic potential

$$V(\phi) = \lambda^2 \phi\phi^* (\phi\phi^* - \nu^2)^2. \tag{2.2}$$

The corresponding gauge invariant Lagrangian density is

$$\mathcal{L}[\phi, A_\mu] = -\frac{1}{4} F_{\mu\nu} F^{\mu\nu} + (D_\mu\phi)^* D^\mu \phi - V(\phi), \tag{2.3}$$

where the gauge field strength is $F_{\mu\nu} = \partial_\mu A_\nu - \partial_\nu A_\mu$, and the covariant derivative is $D_\mu = \partial_\mu - ieA_\mu$. We refer to this model as the $\phi^6$ model. Although the $\phi^6$ and the abelian-Higgs models are similar, we remark here an important difference. The potential 2.2, shown in figure 2.1, has a minimum at $\phi = 0$, allowing the existence of the Coulomb

[2] Equivalently, we consider translation invariance in one direction of a $(3+1)$ spacetime.

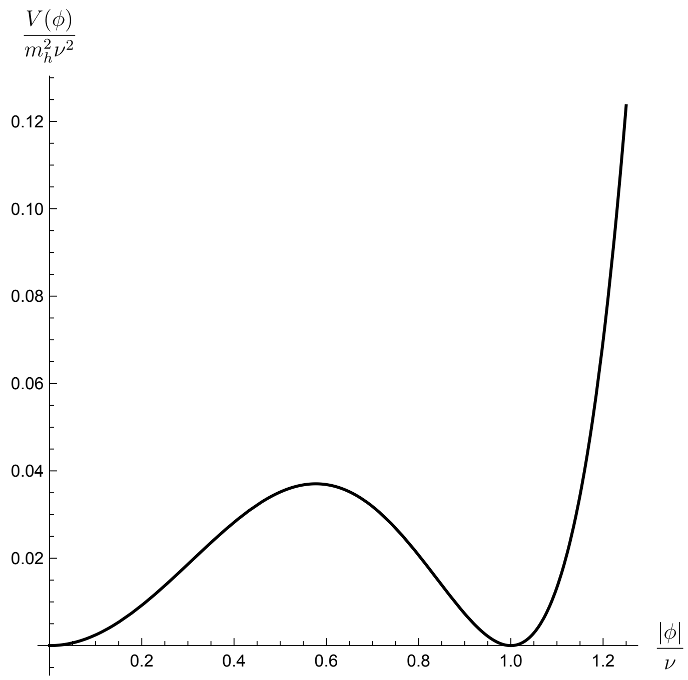


Figure 2.1.: Scalar field potential $V(\phi)$ 2.2

phase after the Higgs condensates and acquires a VEV, while the potential 1.2 does not allow this possibility. In addition, in $(2+1)$ dimensions, the $\phi^6$ model is renormalizable.

The field equations for $\phi$ and $A_\mu$, calculated from the Lagrangian 2.3, are respectively

$$\Box\phi + \frac{\partial V(\phi)}{\partial\phi^*} = 0, \tag{2.4}$$

$$\partial_\mu F^{\mu\nu} = j^\nu, \tag{2.5}$$

where $\Box = D_\mu D^\mu$, and is $j^\mu = -i\left(\phi^* D^\mu\phi - (D^\mu\phi)^*\phi\right)$ is the Noether current associated to the $U(1)$ symmetry. The coupled system of partial differential equations 2.4 and 2.5 is non-linear, and general analytical solutions are not known. However, the spectrum of vacuum excitations, and numerical approximations to different solutions can be found as we describe bellow.

### 2.2.2. Spectrum of the Model

We start by discussing sepctrum of vacuum excitations. We proceed as we did before for the abelian-Higgs model. Due to Noether's theorem, and the invariance of the Lagrangian under time translation, the total energy is conserved. The energy functional is given by

$$
\begin{aligned}
E[\phi, A_\mu] = \int d^2x \Big[ & \frac{1}{2} F_{0i} F_{0i} + \frac{1}{4} F_{ij} F_{ij} \\
& + (D_0\phi)^* D_0\phi + (D_i\phi)^* D_i\phi + V(\phi) \Big],
\end{aligned}
\tag{2.6}
$$

where the indices $i$, $j$ run over 1 and 2. A ground state of this model is a field configuration $\left(\phi^{(v)}, A_\mu^{(v)}\right)$ which minimises the energy functional 2.6. The first four terms of the integrand of 2.6 are non-negative. To minimise the energy, these four terms should vanish. It implies that $A_\mu^{(v)}$ is pure gauge.

The Higgs field $\phi$ will acquire a certain vacuum expectation value (VEV) $\langle\phi\rangle$, such that $V(\langle\phi\rangle)$ is a (local) minimum of the potential. It is important to repeat a previous remark: $\langle\phi\rangle$ does not need to be constant over all the spacetime. Moreover, if the spacetime points x and y are causally disconnected, then $\langle\phi(\mathrm{x})\rangle$ and $\langle\phi(\mathrm{y})\rangle$ are independent. For now we consider the case in which $\langle\phi\rangle$ is constant, and consider perturbations about it in order to determine the spectrum of excitations of the model. Since $V(\phi) \geq 0$, then $\langle\phi\rangle$ being a (local) minimum of the potential implies that $V(\langle\phi\rangle) = 0$. Thus the VEV has the following two possibilities:

$$
\langle\phi\rangle = \begin{cases} 0, & \textbf{Coulomb or Symmetric Phase,} \\ \\ ve^{i\alpha}, & \textbf{Higgs or Broken Phase,} \end{cases}
\tag{2.7}
$$

where $\alpha = \alpha(x)$ is arbitrary. To appreciate this fact, we have plotted the scalar field potential 2.2 in the figure 2.2.

In the first possibility, $\langle\phi\rangle = 0$, perturbations of the fields around the VEV determine the following spectrum:

- A charged boson–corresponding to the complex field $\phi$. Its mass is $m_\phi = \lambda v^2$, and it carries two degrees of freedom.

- A massless real gauge boson–corresponding to the gauge field $A_\mu$–carrying two degrees of freedom.

We notice that the spectrum corresponds to a Coulomb or symmetric phase. In the figure 2.2, this phase corresponds to the blue region.

On the other hand, the second possibility, $\langle\phi\rangle = ve^{i\alpha}$, determines a Higgs or broken phase–corresponding to the orange region of the figure 2.2. More precisely the phenomena of spontaneous symmetry breaking or Higgs mechanism occurs, and the gauge boson becomes massive. The spectrum of the theory can be found as we discussed for the abelian-Higgs model. It is always possible to perform a gauge transformation such that we fixed the gauge to be unitary, i.e. $\langle\phi\rangle = v$. Let's consider a perturbation of $\phi$

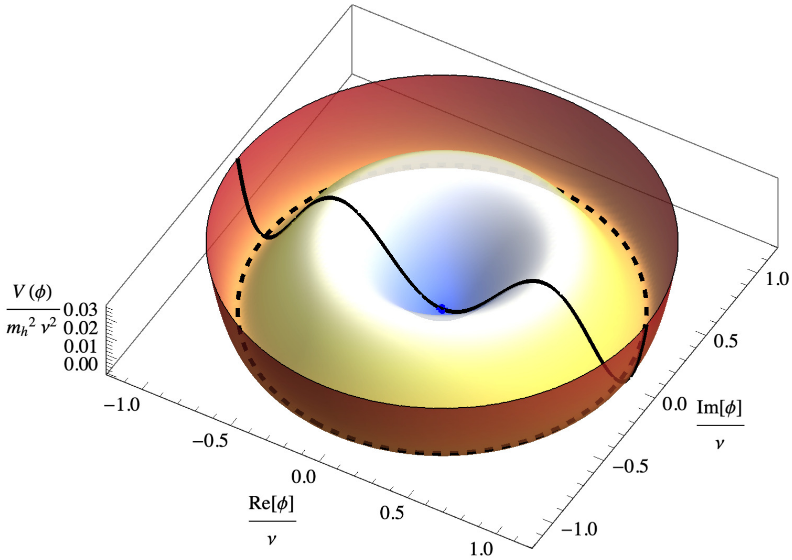


Figure 2.2.: Scalar field potential 2.2. The minimum of $V(\phi)$–achieved when $V(\phi) = 0$–is degenerate. The blue dot corresponds to the minimum at $\langle\phi\rangle = 0$, while the dashed line represents the minimum at $\langle\phi\rangle = ve^{i\alpha}$. These minima correspond to a Coulomb, and a Higgs phases of the model, respectively. The solid black line corresponds to the scalar field potential when $\phi$ is constrained to be a real field.

about its VEV, namely $\phi = \left(v + \frac{h}{\sqrt{2}}\right) e^{i\theta}$. Here $h$ and $\theta$ are real fields. Rewriting the potential in terms of $h$ and $\theta$ we find:

$$V(\phi) \equiv V(h) = 2\lambda^2 v^4 h^2 + 3\sqrt{2}\lambda^2 v^3 h^3 + \frac{13}{4}\lambda^2 v^2 h^4 + \frac{3\sqrt{2}}{4}\lambda^2 v h^5 + \frac{1}{8}\lambda^2 h^6.$$

In order to bring the Lagrangian to the canonical form we introduce the field

$$B_\mu = A_\mu - \frac{1}{e}\partial_\mu \theta,$$

and change the field variables $(\phi,\ A_\mu)$ to $(h,\ B_\mu)$. Thus the Lagrangian 2.3 becomes

$$\mathcal{L}[h, B_\mu] = -\frac{1}{4}B_{\mu\nu}B^{\mu\nu} + e^2 v^2 B_\mu B^\mu + \frac{1}{2}\partial_\mu h \partial^\mu h + 2\lambda^2 v^4 h^2 + \mathcal{L}_{\mathrm{int}}, \tag{2.8}$$

where $B_{\mu\nu} = \partial_\mu B_\nu - \partial_\nu B_\mu$, and the interaction part of the Lagrangian is

$$\begin{aligned}\mathcal{L}_{\mathrm{int}} =& 3\sqrt{2}\lambda^2 v^3 h^3 + \frac{13}{4}\lambda^2 v^2 h^4 + \frac{3\sqrt{2}}{4}\lambda^2 v h^5 + \frac{1}{8}\lambda^2 h^6 \\ &+ \sqrt{2}e^2 v B_\mu B^\mu h + \frac{1}{2}e^2 B_\mu B^\mu h^2.\end{aligned}$$

From the canonical form 2.8, we get that the spectrum of the model in the Higgs phase is composed by:

- A neutral Higgs boson–corresponding to the scalar field $h$. Its mass is $m_h = 2\lambda v^2$, and it carries one degree of freedom.
- A massive vector boson–corresponding to the vector field $B_\mu$. Its mass is $m_v = \sqrt{2}ev$, and it carries three degree of freedom.

By way of conclusion of this section, we observe that the scalar field potential 2.2 can also be understood as a polynomial approximation to the finite temperature effective potential–at the critical temperature $T_c$–of a model undergoing a first order phase transition. In the $\phi^6$ model, Coulomb and Higgs phases can arise in different regions of space–the phase of certain region being determined by the VEV of the scalar field $\phi$. Qualitatively, this behaviour is the same for the abelian-Higgs model, with effective potential 1.17, at $T = T_c$.

The finite temperature effective potential at $T_c$–shown by (e) of figure 1.2–can be approximated by a sextic potential, $V_6(\varphi)$, as it is shown in figure 2.3. The corresponding parameters $\lambda$ and $v$ (see equation 2.2) can be constrained by the following two conditions.

- Firstly, we imposed that the VEV of $\varphi$ is the same for both potentials–the effective, and the sextic potential–implying that the minima of the potentials coincides. The norm of the field at the non-zero minimum of the effective potential can be found numerically[3]. Then, this value constraints the parameter $v$ to be

  $$v = a\sigma,$$

  where $a$ is a dimensionless parameters depending on $\nu_0$ (see equation 1.15).
- Secondly, we impose that the height of the potential barrier separating the different minima, $\Delta V$, is the same for the effective, and the sextic potential. For $V_{\text{eff}}(\varphi, T_c)$, $\Delta V_{\text{eff}}$ can be computed numerically in terms of $\mu_0^2\sigma^2$, while for $V_6(\varphi)$ we obtained

  $$\Delta V_6 = \frac{4}{27}\lambda^2 v^6,$$

  and it is achieved at $|\varphi| = \frac{1}{\sqrt{3}}v$. Equating both heights, and solving for $\lambda$, one gets

  $$\lambda = b\frac{\mu_0}{\sigma^2},$$

  where $b$ is a dimensionless parameter depending on $\nu_0$.

Finally, the masses of the Higgs boson, and the Gauge boson can be estimated as $m_h \sim \mu_0$, and $m_v \sim e\sigma$. Figure 2.3 shows an explicit example of these estimations.

So far we have shown that there exist two different phases in the $\phi^6$ model. If they are realised simultaneously in regions of space that are causally disconnected, different topological defects would be formed due to the Kibble mechanism. We recall that one of the motivations for considering the $\phi^6$ model was the existence of defects. In the following section we will show that Domain Walls, and vortices are part of the model spectrum.

[3] It is possible to find the minimum and maximum of the effective potential using the Lambert W function, also called the product logarithm. However, for our discussion, an explicit expression is not required.

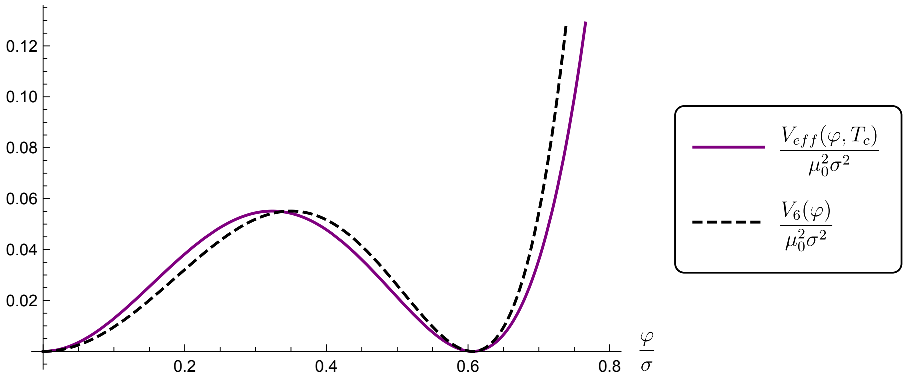


Figure 2.3.: Finite temperature effective potential and its polynomial approximation. The effective potential at critical temperature $T_c$, $V_{\text{eff}}(\phi, T_c)$, is given by the equation 1.17, while the polynomial approximation, $V_6(\phi)$, is given by 2.2. In the plot $\nu_0 = 0.25$, and the critical temperature corresponds to $T_c = 0.095e\sigma$. The parameters in $V_6(\phi)$ are constraint to be $\nu = 0.61\sigma$ $\lambda = 2.73\frac{\mu_0}{\sigma^2}$. The corresponding Higgs boson mass, and vector boson mass are $m_h = 2.01\mu_0$, $m_v = 0.86e\sigma$.

### 2.2.3. Topological Defects in the $\phi^6$-Model

As we described in section 1.2, the classification of the possible topological defects that can appear during a phase transition of a certain model is determined by the topology of its vacuum manifold $\mathcal{M}$, and its homotopy groups[4]. We proceed in such way to classify the defects in the $\phi^6$ model.

*The Topology of the Vacuum Manifold $\mathcal{M}$*

The equation 2.7 determines the vacuum manifold $\mathcal{M}$ of the theory, up to gauge transformations. More explicitly, let $G = U(1)$ be the gauge group, and $\phi_0 = \langle\phi\rangle$ the VEV of the Higgs field. The corresponding unbroken subgroup–or little group–of $G$ respect to $\phi_0$ is[4]

$$H_{\phi_0} = \{g \in G | g\phi_0 = \phi_0\},$$

and the quotient group $G/H_{\phi_0}$ corresponds to the different field configurations that are not equivalent under gauge transformations. Since $\phi_0$ can take different values, we discuss them separately.

If $\phi_0 = 0$, one finds that $H_0 = U(1)$, and the quotient group is

$$\mathcal{M}_{\text{C}} \equiv G/H_0 = 1.$$

Instead, if $\phi_0 = \nu e^{i\alpha}$, one finds that $H_{\nu e^{i\alpha}} = \{I\}$, where $I$ is the identity element of the $G$ group. Since $\alpha$ is arbitrary, we identify $H_\nu \equiv H_{\nu e^{i\alpha}}$. The quotient group in this case is

$$\mathcal{M}_{\text{H}} \equiv G/H_\nu = U(1).$$

[4]Here $g\phi_0$ is the action of $g$ over the field $\phi_0$.

Finally, the vacuum manifold can be identified with the disjoint union

$$\mathcal{M} \equiv \mathcal{M}_{\mathrm{C}} \dot{\cup} \mathcal{M}_{\mathrm{H}}.$$

These two disconnected components correspond to the Coulomb phase, and the Higgs phase, respectively. This correspondence can be appreciated graphically in figure 2.2. $\mathcal{M}_{\mathrm{C}}$ is homeomorphic to the point $\phi = 0$–corresponding to the blue dot –while $\mathcal{M}_{\mathrm{H}}$ is homeomorphic to the circumference $S^1$ given by $\phi = ve^{i\alpha}$–corresponding to the dashed line.

Now, we compute the homotopy groups of the vacuum manifold, $\pi_n(\mathcal{M})$. For $n = 0$,[5]

$$\pi_0(\mathcal{M}, v) = \{[f_0], [f_1]\}, \tag{2.9}$$

where $f_0$, and $f_1$ are maps from the 0-sphere–$S^0 = \{-1, 1\}$–to $\mathcal{M}$ given by

$$\begin{aligned} f_0(1) = v,\;\; f_0(-1) = v, \\ f_1(1) = v,\;\; f_1(-1) = 0, \end{aligned}$$

and $[c_v]$, $[f_v]$ are the corresponding homotopy classes. Each homotopy class $[f] \in \pi_0(\mathcal{M}, v)$ correspond to a different connected component of $\mathcal{M}$. In consequence $\pi_0(\mathcal{M}, 0)$ and $\pi_0(\mathcal{M}, v)$ can be identified with each other.

$$\pi_0(\mathcal{M}) \equiv \pi_0(\mathcal{M}, 0) \equiv \pi_0(\mathcal{M}, v)$$

For $n = 1$, we compute the first homotopy group–also known as fundamental group–for each connected componenet of $\mathcal{M}$, separeately:

$$\begin{aligned} \pi_1(\mathcal{M}_{\mathrm{H}}) &\equiv \pi_1(\mathcal{M}, v) \\ &= \pi_1(G/H_v) \\ &= \pi_1(U(1)) \\ &= \mathbb{Z}. \end{aligned} \tag{2.10}$$

$$\begin{aligned} \pi_1(\mathcal{M}_{\mathrm{C}}) &\equiv \pi_1(\mathcal{M}, 0) \\ &= \pi_1(G/H_0) \\ &= \pi_1(1) \\ &= 0. \end{aligned} \tag{2.11}$$

Lastly, for $n \geq 2$,

$$\begin{aligned} \pi_n(\mathcal{M}_{\mathrm{C}}) = 0 \\ \pi_n(\mathcal{M}_{\mathrm{H}}) = 0. \end{aligned} \tag{2.12}$$

[5]Strictly speaking $\pi_0(\mathcal{M}, x)$ is not a group but the set of homotopy classes,$[f]$, of maps $f : S^0 \to \mathcal{M}$ with base point $x$.

### Domain Walls and Vortex Lines in the $\phi^6$ Model

The criteria for topological defects existence in terms of the homotopy groups of $\mathcal{M}$, dictates that in the $\phi^6$ model different topological defects are part of the spectrum of the model. The classification of these defects is as follows.

- By equation 2.9, $|\pi_0(\mathcal{M})| = 2$. Thus, there can exist static field configurations that depend on one space dimension and asymptotically approach two different phases. We will refer to this configurations as $(\nu, 0)$**-Domain Walls**. We remark here that the $(\nu, 0)$-Domain Walls in the $\phi^6$ model are different to the kink solutions in $\phi^4$ Goldstone model. While a kink interpolates between two Higgs phases with different VEV $\langle\phi\rangle$, a $(\nu, 0)$-Domain Wall interpolates between the Higgs, and the Coulomb phases.

- By equation 2.10, $\pi_1(\mathcal{M}_{\mathrm{H}}) = \mathbb{Z}$. Thus, there can exist static field configurations that approach asymptotically the Higgs Phase with non-zero *winding number*. These configurations are known as **Vortices** in $(2+1)$ dimensions, and Strings–or Vortex Lines–in higher dimensions. On the other hand, by equation 2.11, $\pi_1(\mathcal{M}_C) = 0$, and then there are not vortex configurations in the Coulomb phase

- By equation 2.12, $\pi_n(\mathcal{M}_h) = \pi_n(\mathcal{M}_c) = 0$, for $n \geq 2$, and consequently there are not monopoles nor textures in the spectrum of the $\phi^6$ model.

In the following chapters we will elaborate on each of these topological defects in the $\phi^6$ model. In chapter 3, we discuss properties of the $(\nu, 0)$-Domain Walls, and present analytical solutions for the field configurations. In addition, vortex configuration are discussed in chapter 4. Although analytical solutions for the vortex field configurations are not know, we present approximate solutions to them.

Finally, the motivations to study this model become clearer. We required that the Domain Walls can form a finite-size configuration that asymptotically interpolates two broken phases with a core inside which the full symmetry group $U(1)$ is restored. Strictly speaking, such configurations are not topologically protected. To avoid misunderstandings, we will refer to this configuration as a *Coulomb vacuum layer*. As a first approximation, a Coulomb vacuum layer can be achieved as a concatenation of two $(\nu, 0)$-Domain Walls: one interpolating between the Higgs and the Coulomb phase, and a second one interpolating between the Coulomb and the Higgs phase. As a result, inside the core of a Coulomb vacuum layer the full symmetry is restored as required, while asymptotically in interpolates two Higgs phases.

We studied the interaction of vortices and Coulomb vacuum layers by a numerical simulation of the classical evolution of fields. Our results bear out the erasure of defects mechanism proposed by Dvali-Liu-Vachaspati. In the following chapters, we describe in detail the Coulomb vacuum layers, the vortices, and their interactions. In chapter 5 we present our results, and discuss how the vortex unwinding occurs in the core of the Coulomb Vacuum layer.

# 3. Domain Walls and Coulomb Vacuum Layers

In the $\phi^6$ model, described by the Lagrangian,2.3, there are two different phases: a Higgs phase, and a Coulomb phase. If they are realised simultaneously in two neighbour regions of space a $(\nu, 0)$-Domain Wall would be formed.

A first approximation to the field profiles configuration, $(\phi,\ A_\mu)$, in the transition region between the two phases can be obtained by finding the field configuration that minimises the energy functional 2.6, and maintains the asymptotic behaviour interpolating the two phases.

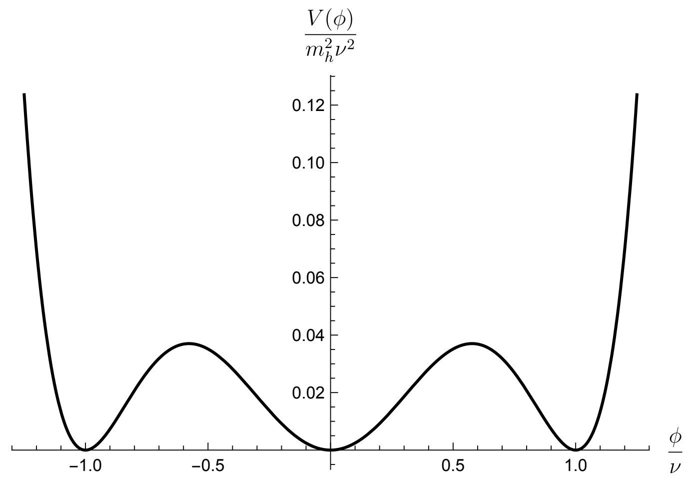


Figure 3.1.: Scalar field potential 2.2 for a real scalar field $\phi$. This plot corresponds to the solid black line of figure 2.2. Observe that the vacuum manifold is restricted to $\mathcal{M}_{\mathrm{DW}} = \{-\nu, 0, \nu\}$

More precisely, let's assume for now that the field $\phi = \phi(t, x, y)$ depends only on the coordinate $x$. Moreover, let's assume that the Domain Wall does not carry electric charge. Therefore, we can fix $A_\mu = 0$, and $\phi$ to be real. Therefore, the scalar field potential is constrained as it is shown in figure 3.1. Redefining the field $\phi$ as $\phi = \frac{\chi}{\sqrt{2}}$, where $\chi$ is a real field, the Lagrangian 2.3 becomes

$$\mathcal{L}_{DW} = \frac{1}{2}\partial_\mu \chi \partial^\mu \chi - \lambda^2 \frac{\chi^2}{2}\left(\frac{\chi^2}{2} - \nu^2\right)^2. \tag{3.1}$$

With these considerations, the canonical Lagrangian 3.1 corresponds to a model in

$(1+1)$ dimensions for a real scalar field $\chi$ and potential

$$V_\chi \equiv \lambda^2 \frac{\chi^2}{2}\left(\frac{\chi^2}{2} - \nu^2\right)^2.$$

We are interested in finite energy, and static field configurations of $\chi(x)$, with the following asymptotic behaviour approaching two different phases:

$$\begin{aligned} \lim_{x\to-\infty} \chi(x) &= 0 \\ \lim_{x\to\infty} \chi(x) &= \sqrt{2}\nu \end{aligned} \tag{3.2}$$

The field equation 2.4 becomes

$$\chi'' = \frac{dV_\chi}{d\chi}, \tag{3.3}$$

where prime denotes derivative respect to $x$. Solutions to equation 3.3 have been studied by Vakhid et.al [36]. These solutions are precisely found when the Bogomolny bound–or BPS condition–is saturated, as we show bellow. The energy functional 2.6 is rewritten in terms of $\chi$ as

$$\begin{aligned} E[\chi] &= \int dx \left[\frac{1}{2}\chi'^2 + V\left(\frac{\chi}{\sqrt{2}}\right)\right] \\ &= \int dx \left[\frac{1}{2}\left(\chi' \pm \sqrt{2V\left(\frac{\chi}{\sqrt{2}}\right)}\right)^2 \mp \chi'\sqrt{2V\left(\frac{\chi}{\sqrt{2}}\right)}\right] \\ &\geq \mp \int dx \chi' \sqrt{2V\left(\frac{\chi}{\sqrt{2}}\right)}. \end{aligned} \tag{3.4}$$

When the bound is saturated, one gets:

$$\begin{aligned} \chi' &= \pm\sqrt{2V\left(\frac{\chi}{\sqrt{2}}\right)} \\ &= \pm\lambda\chi\left(\frac{\chi^2}{2} - \nu^2\right). \end{aligned} \tag{3.5}$$

Solving 3.5 for $\frac{\chi(x)}{\sqrt{2}}$, one finds the field profiles

$$\begin{aligned} \phi_{\text{DW}}(x) &= \pm\nu\sqrt{\frac{1}{2}\left(1 \pm \tanh\left(\lambda\nu^2 x\right)\right)} \\ &= \pm\nu\sqrt{\frac{1}{1+e^{\pm 2\lambda\nu^2 x}}}. \end{aligned} \tag{3.6}$$

There are four different solutions, and the reason is the following. When one restricts $\phi$ to be a real field, the vacuum manifold is reduced to $\mathcal{M}_{\text{DW}} = \{-\nu, 0, \nu\}$ (see figure

3.1). Then, the possible asymptotic behaviours of a Domain Wall are: $(0, \nu)$, $(0, -\nu)$, $(-\nu, 0)$,$(-\nu, 0)$, where we used the notation[1] $(\phi_-, \phi_+)$. Using the same convention, and recalling that $m_h = 2\lambda\nu^2$, we will refer to the different Ansätze

$$\phi_{(\pm\nu,0)}(x) \equiv \pm\nu\sqrt{\frac{1}{1+e^{m_h x}}}, \tag{3.7}$$

$$\phi_{(0,\pm\nu)}(x) \equiv \pm\nu\sqrt{\frac{1}{1+e^{-m_h x}}}, \tag{3.8}$$

as the $(\pm\nu, 0)$-Domain Wall, and $(0, \pm\nu)$-Domain Wall profiles, respectively. The asymptotic behaviour 3.2 corresponds to the $(0, \nu)$-Domain Wall profile. This profile is plotted in figure 3.2.

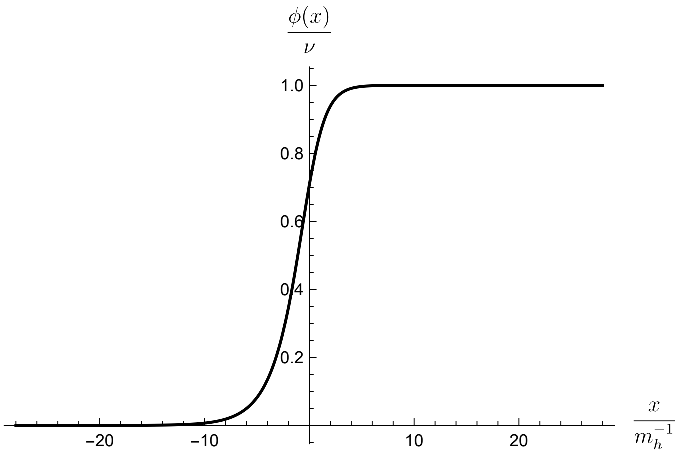


Figure 3.2.: $(0, \nu)$-Domain Wall profile, $\phi_{(0,\nu)}(x)$.

Highlight the fact that the solutions approach exponentially fast the VEV of the corresponding asymptotic phase. The energy density (the integrand of the left hand side of equation 2.6) for a real field $\phi(t, x)$ is

$$\mathcal{E}[\phi(t, x)] = \partial_t\phi^2 + \partial_x\phi^2 + V(\phi). \tag{3.9}$$

For a $(0, \nu)$-Domain Wall, it reduces to

$$\begin{aligned}\epsilon(x) \equiv \mathcal{E}[\phi_{(0,\nu)}(x)] &= \phi'(x)^2 + V(\phi(x)) \\ &= 2\lambda^2\nu^6 \frac{e^{2\lambda\nu^2 x}}{\left(e^{2\lambda\nu^2 x}+1\right)^3} \\ &= \frac{m_h^3}{4\lambda}\frac{e^{m_h x}}{\left(e^{m_h x}+1\right)^3}.\end{aligned} \tag{3.10}$$

[1] $\phi_\pm \equiv \lim_{x\to\pm\infty} \phi(x)$. Compare to equation 1.22

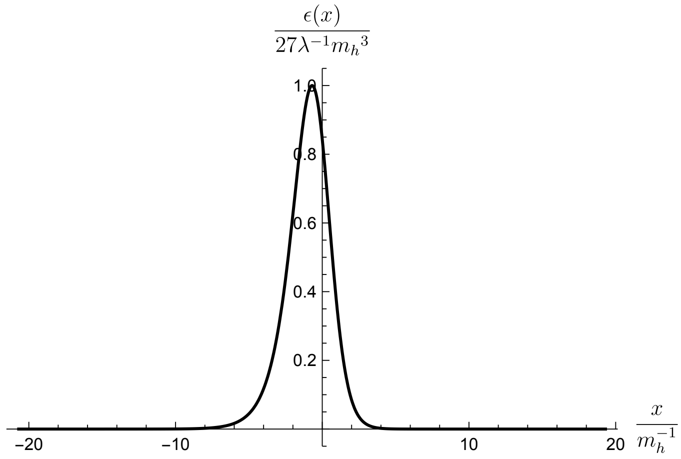


Figure 3.3.: $(0,\nu)$-Domain Wall energy density 3.10

The energy density 3.10 has a maximum at $x = -\log(2)m_h^{-1}$, corresponding to two times the maximum of the scalar field potential, $\epsilon_{\max} = \frac{8}{27}\lambda^2\nu^6 = \frac{m_h^3}{27\lambda}$. Notice that

$$\epsilon(x) \sim \frac{m_h^3}{4\lambda}e^{m_h x}, \qquad \text{for } x \to -\infty, \text{ and}$$
$$\epsilon(x) \sim \frac{m_h^3}{4\lambda}e^{-2m_h x}, \qquad \text{for } x \to \infty.$$

Thus, $\epsilon(x)$ is significantly different from zero only if $|x - \log(2)m_h^{-1}| \lesssim r_{\mathrm{DW}} \sim m_h^{-1}$, where the size of the $(0,\nu)$-Domain Wall, $r_{\mathrm{DW}}$, is of order $m_h^{-1}$. Integrating $\epsilon(x)$, we get the total energy

$$M_{\mathrm{DW}} = \frac{m_h^2}{8\lambda}.$$

In the weakly coupled regime, $\lambda \ll m_h$, thus $m_h \ll M_{\mathrm{DW}}$. Then, the Compton wavelength corresponding to the energy of the $(0,\nu)$-Domain Wall–$\lambda_{\mathrm{DW}} = M_k{}^{-1}$–is much smaller than the classical size of the Wall–$r_{\mathrm{DW}}$–i.e.

$$\frac{r_{\mathrm{DW}}}{\lambda_{\mathrm{DW}}} \sim \frac{m_h}{\lambda} \gg 1.$$

A similar discussion would follow for the $(0,-\nu)$, $(\nu,0)$, and $(-\nu,0)$-Domain Walls. One finds that the size, and the total energy of the Walls is the same for all the four topological sectors. Consequently, we will treat a Domain Wall essentially as a classical object. These results should not be surprising since, in general, Domain Walls are analogous to the Kink solutions of the Goldstone Model, and thus these field configurations are expected to be highly massive in the weakly coupled regime[12].

The solutions 3.6 are not invariant under spatial translations, nor boost transformations. However, the transformed field configurations

$$\phi_{(x_0,u)}(t,x) = \phi_{\mathrm{DW}}(\gamma_u((x-x_0)-ut)), \tag{3.11}$$

are also solutions to the field equation 2.4, where $u$ represents the velocity of the Wall, and $\gamma_u = (1-u^2)^{-\frac{1}{2}}$ is the correspondent Lorentz factor. The total energy becomes $M_{(x_0,u)} = \gamma_u M_{\mathrm{DW}}$. We will refer to these solutions as boosted Domain Walls.

## 3.1. Coulomb Vacuum Layer: the $(\pm\nu, 0, \pm\nu)$ Domain Wall

One of the motivation to study the $\phi^6$ model, is the possibility of constructing a field configuration interpolating between two different Higgs phases with a core inside which the symmetry is restored, i.e. the core is in the Coulomb phase. To show that such field configurations are realizable, lets consider again a real (charge less) scalar field $\phi$. Then if a $(\pm\nu, 0)$-Domain Wall, and a $(0, \pm\nu)$-Domain Wall are concatenated, then the symmetry is restored in the region between the two Domain Walls. The Ansätze for these configurations are given by:

$$\phi_{(\pm\nu,0,\pm\nu)}(x) = \phi_{(\pm\nu,0)}\left(x + \frac{l}{2}\right) + \phi_{(0,\pm\nu)}\left(x - \frac{l}{2}\right), \tag{3.12}$$

where $l$ is the distance between the Domain Walls. We will refer to these field configurations as a Coulomb Vacuum Layer, or a $(\pm\nu, 0, \pm\nu)$-Domain Wall. Figure 3.4 shows the Coulomb Vacuum Layer profiles corresponding to $l = 40 m_h^{-1}$.

*Dynamical Stability of $(\pm\nu, 0, \pm\nu)$-Domain Walls*

Notice that the Ansätze 3.12 is just an approximate solution to the field equation 2.4. Therefore, it is expected to be unstable under time evolution. The dynamical evolution of $(\pm\nu, 0, \pm\nu)$ Domain Wall profiles have been investigated by Vakhid et al. in [36]. They used the collective coordinate approximation, and numerical simulations to study the classical stability of the Ansätze.

There are two conclusions of [36] that are relevant for our discussion. The first one is respect to the dynamical evolution of the $(\nu, 0, \nu)$-Domain Wall[2].It is energetically favourable for the $(\nu, 0)$, and the $(0, \nu)$-Domain Walls to attract each other, and eventually they collide. As a consequence, the Coulomb Vacuum Layer is unstable, but the two colliding Walls can form a long-lived bound state (referred to as bion). We have reproduced these phenomena by solving the field equation 2.4 numerically. An example of the found solutions is shown in figure 3.5.

The second relevant conclusion is respect to the dynamical evolution of the $(-\nu, 0, \nu)$ Domain Wall[3]. In this case, the two Walls repel each other till they get a limit speed, and the parameter $l$ increases infinitely. We also reproduced these phenomena numerically, and an example of the results is shown in figure 3.6.

In general, the unstable behaviour of a Coulomb Vacuum Layers is independent of its core size, $l$. However, the time scale during which a Layer is stable is proportional to $l$. Moreover, we found that, if $40 m_h^{-1} \lesssim l$, the Domain Wall can be considered to be stable for time scales of order $\mathcal{O}(10^2 m_h^{-1})$. Figure 3.7 shows this behaviour. We conclude this

[2]A similar discussion applies to the evolution of the $(-\nu, 0, -\nu)$ Domain Wall.

[3]A similar discussion applies to the evolution of the $(\nu, 0, -\nu)$ Domain Wall

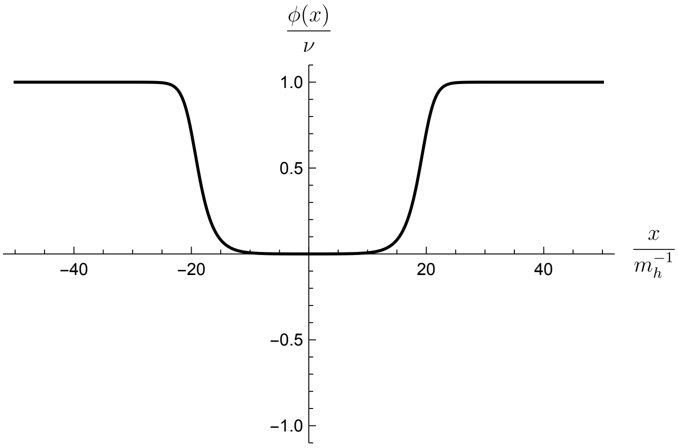


(a) $\phi_{(\nu,0,\nu)}(x)$

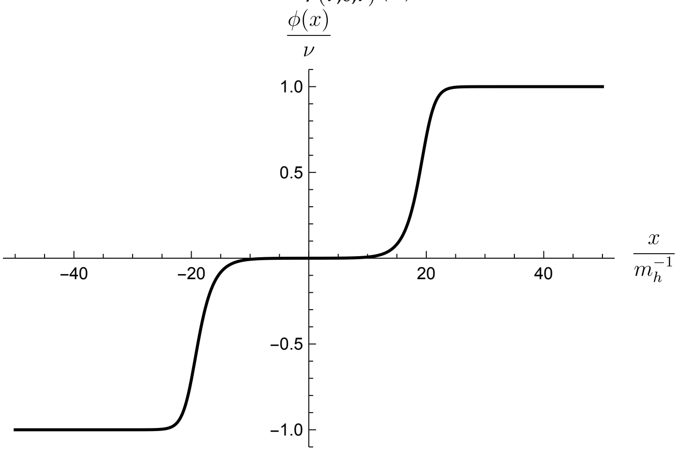


(b) $\phi_{(-\nu,0,\nu)}(x)$

Figure 3.4.: Coulomb Vacuum Layer profiles, with a core size $l = 40m_h^{-1}$

section with this important fact, which will be relevant for the interaction of Coulomb Vacuum Layer with vortices.

### 3.1.1. Complex Coulomb Vacuum Layers: the $(e^{i\alpha}\nu, 0, \nu)$ Domain Wall

If we restrict to $(1+1)$ dimensions, and we assume the field $\phi$ to be real, the topological defects are the $(\pm\nu, 0)$ or $(0, \pm\nu)$ Domain Walls. It is possible to generalise this Domain Walls if the field $\phi$ is complex. In this case there would be a phase $\alpha$ determining the asymptotic relative phase of the field $\phi$ in the broken phase. Then, using the same convention as before, there could be produced $(e^{i\alpha}\nu, 0)$ or $(0, e^{i\alpha}\nu)$-Domain Walls. We study the time evolution of the $(e^{i\alpha}\nu, 0)$ or $(0, e^{i\alpha}\nu)$-Domain Walls for the case of global, and gauge symmetry. In the case of global $U(1)$ symmetry, the field configuration that minimises the energy is the one which has constant phase $\alpha$. On the other hand, in the case of $U(1)$ gauge symmetry, the difference in phase between the two broken phases,

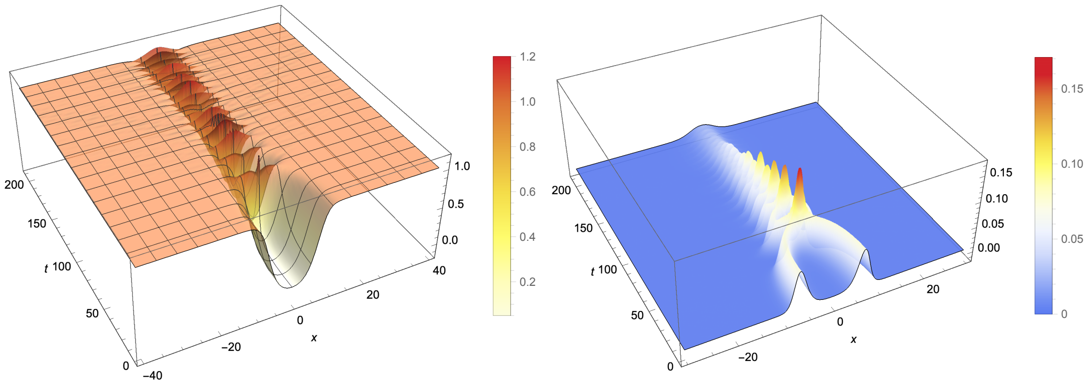


(a) $\phi(t,x)$ (b) $\mathcal{E}[\phi(t,x)]$

Figure 3.5.: Dynamical evolution of the $(\nu, 0, \nu)$ Domain Wall. We observe the creation of a bion after the collision of the two Walls. (a) shows the time evolution of the field profile, while (b) shows the time evolution of the energy density. For this simulation, we have fixed the parameters $\nu = 1$, and $\lambda = 1/2$, corresponding to $m_h = 1$. At $t = 0$, the core size of the Coulomb Vacuum Layer is $l = 15 m_h^{-1}$.

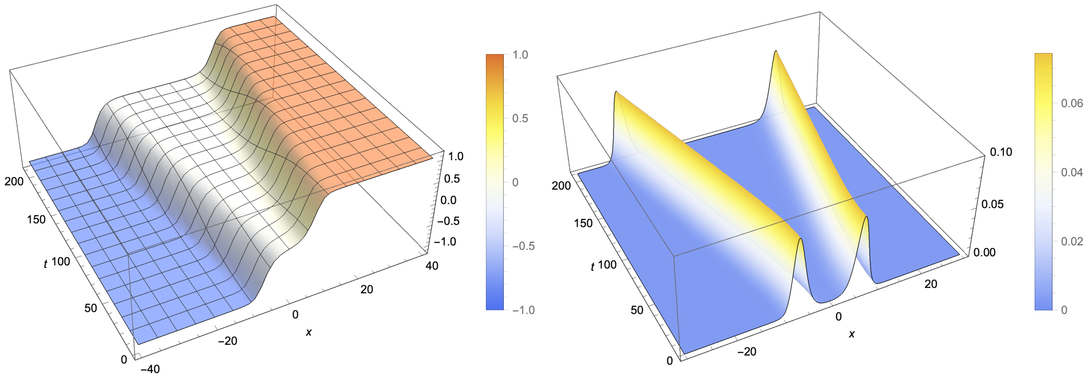


(a) $\phi(t,x)$ (b) $\mathcal{E}[\phi(t,x)]$

Figure 3.6.: Dynamical evolution for the $(-\nu, 0, \nu)$ Domain Wall. (a) shows the time evolution of the field profile, while (b) shows the time evolution of the energy density. For this simulation, we have fixed the parameters $\nu = 1$, and $\lambda = 1/2$, corresponding to $m_h = 1$. At $t = 0$, the core size of the Coulomb Vacuum Layer is $l = 15 m_h^{-1}$

can be rotated away, and the time evolution becomes similar to the time evolution of a $(\nu, 0, \nu)$-Domain Wall. According to our simulations, we can extend our previous results for complex scalar fields: a Coulomb Vacuum Layers can be considered stable for $\mathcal{O}(10^2 m_h^{-1})$, if $l > 40 m_h^{-1}$. The results of the performed simulations can be found in the following web page `https://github.com/jusvalbuenabe/TMP-Valbuena`

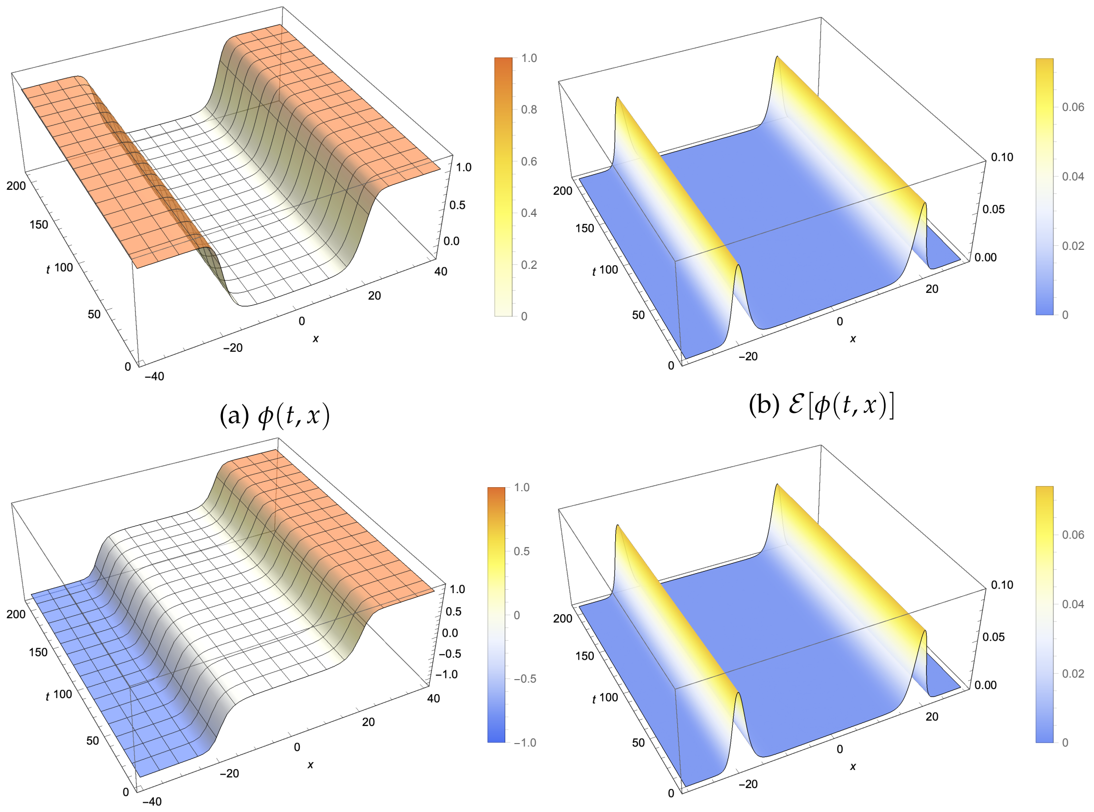


(a) $\phi(t,x)$

(b) $\mathcal{E}[\phi(t,x)]$

(c) $\phi(t,x)$

(d) $\mathcal{E}[\phi(t,x)]$

Figure 3.7.: Dynamical evolution of a metastable Coulomb Vacuum Layer. At $t = 0$, the core size of the Coulomb Vacuum Layer is $l = 40m_h^{-1}$. The time evolution of the field profile, and the energy density of $(v, 0, v)$-Domain Wall are shown in (a) and (b), respectively. Similarly, (c) and (d) show the time evolution of a $(-v, 0, v)$-Domain Wall. For these simulations, we have fixed the parameters $v = 1$, and $\lambda = 1/2$, corresponding to $m_h = 1$. At $t = 0$, the size of the Layer is $l = 40$. We observe that, for time scales of order $\mathcal{O}(10^2 m_h^{-1})$, the Coulomb Vacuum Layers can be considered as stable.

## 3.2. Domain Walls in $(d+1)$-Dimensions

In general, the problem with extending a Domain Wall solution to $(d+1)$ dimensions is that the energy would become infinite. However at the moment of the phase transition it is still possible that the VEV of the Higgs field inside a finite region is in a certain phase while outside it is in another phase. The boundary of these two regions would be a hyper surface of dimension $d-1$, and it would be stable if its mean curvature is 0, as it is discussed by Kibble in [11][4]. Let's assume that the hyper-surface separating the two regions is not stable, and that it can be approximated by hyper-sphere of radius $R >> m_h^{-1}$. Then the field profile would depend only on the radial coordinate $r$, and the transition region between the two different phases can be approximated by a Domain Wall profile:

$$\phi(r) = \phi_{DW}(r-R).$$

The energy (per unit area)–or tension–of a $(0,\nu)$ Domain Wall is given by the energy functional

$$\begin{aligned} \sigma_{DW} &= \int_{-\infty}^{\infty} dz \left(\partial_z {\phi_{DW}}^2 + V(\phi_{DW})\right) \\ &= \frac{1}{2}\lambda\nu^4 \\ &= \frac{m_h^2}{8\lambda}. \end{aligned} \tag{3.13}$$

In $(1+1)$ dimensions, 3.13 corresponds to the total mass of the Domain Wall, $M_{DW}$, while in $(2+1)$ dimensions, it corresponds to the tension per unit length of the Domain Wall. The total energy of the Domain Wall is then the Domain Wall tension times the area of the hypersphere times the Lorentz factor due to the velocity of the wall:

$$E = \gamma\sigma_{DW} S_{n-1} R^{n-1},$$

where $S_{n-1} = \frac{2\pi^{n/2}}{\Gamma(n/2)}$, and $\gamma = \left(1 - \left(\frac{dR}{dt}\right)^2\right)^{-1/2}$. At a certain moment, the bubble will have a maximum radius $R_0$ and, since its mean curvature is non-0, it will start shrinking. As a first approximation to this process, we can assume the energy of the Domain Wall is conserved, i.e. we neglect radiative effects. Then we have that

$$E_0 = \sigma_{DW} S_{n-1} R_0^{n-1} = \gamma\sigma_{DW} S_{n-1} R^{n-1}$$

Notice that this can be generalised to any type of Domain Wall in arbitrary dimensions i.e. this relation is independent of $\sigma_{DW}$. It follows then that $R_0^{n-1} = \gamma R^{n-1}$, which in

[4] In some curved backgrounds, as the a Schwarzschild-Rindler-anti–de Sitter spacetime, it is possible to find metastable configurations as discussed in [16]

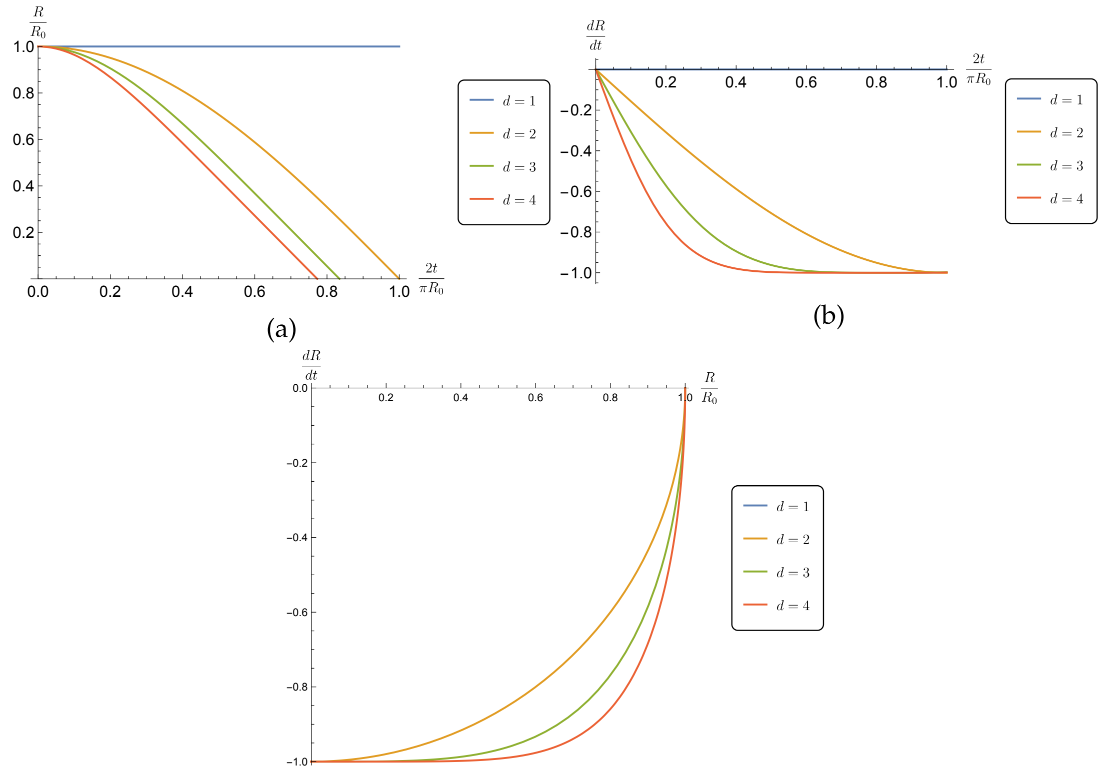


Figure 3.8.: Solutions to equation 3.14 for $d = 1, 2, 3, 4$

turns implies

$$\left(1 - \left(\frac{dR}{dt}\right)^2\right) = \left(\frac{R}{R_0}\right)^{2(d-1)}. \tag{3.14}$$

The solutions to the equation 3.14, for $d = 1, 2, 3, 4$, assuming $R(t = 0) = R_0$, are shown in the figure 3.8.

In $(2+1)$ dimensions, the Domain Wall is a curve, and the bubble configuration would correspond to a circle of radius $R$. In this case the solution to equation 3.14 is $R(t) = R_0 \cos\left(\frac{t}{R_0}\right)$. For small time scales $\Delta t$ compared to the curvature radius $R$, where $m_h^{-1} \ll R < R_0 = \frac{E_0}{\sigma_{DW}}$, the change of the radius is

$$\frac{\Delta R}{R} = \frac{\Delta t}{R}\left(1 - \frac{R}{R_0}\right),$$

while the change of the Domain Wall velocity is

$$\Delta \dot{R} = -\frac{\Delta t}{R_0}\left(\frac{R}{R_0}\right).$$

Although, the field configuration is unstable, for time, and length scales much smaller than $R$, but greater than $m_h^{-1}$–i.e. scales in the vicinity of the hypersphere–it is reasonable

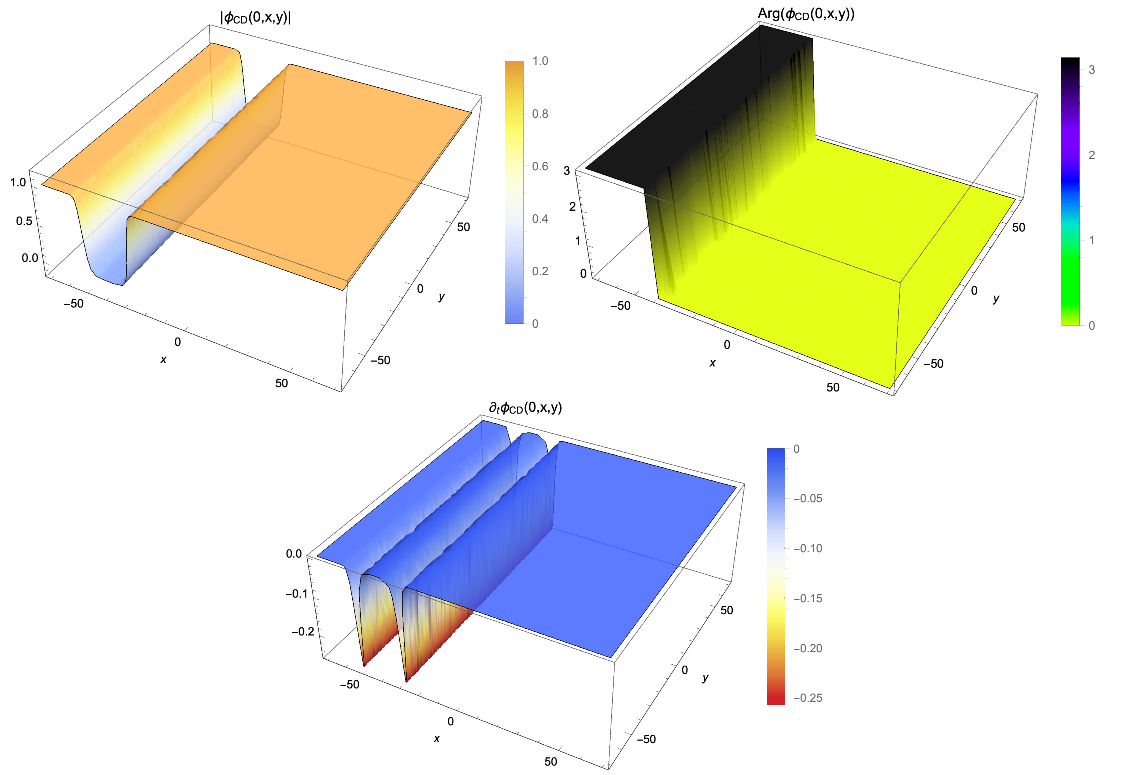


Figure 3.9.: Cauchy data for a boosted $(-\nu, 0, \nu)$-Domain Wall. Here $m_h = 1$, $l = 40$, $v = 0.8$, and $x_0 = -40$. The square mesh has side length $L_{DW} = 140$ and the corresponding total energy is is $m_{DW} = 116.6$.

to approximate the field configurations by an extended boosted Domain Wall moving with a relativistic velocity $v$[5]. It is then reasonable to use the boosted profile

$$\phi(t, x, y) = \phi_{(\pm\nu,0,\pm\nu)}(\gamma(x - vt - x_0))$$

as an ansatz to approximate the field profile of a $(\pm\nu, 0, \pm\nu)$-Domain Wall in $(2+1)$-dimensions.

to define our Cauchy data $\phi_{CD}$. At $t = 0$,

$$\phi_{CD}(0, x, y) = \phi_{(\pm\nu,0,\pm\nu)}(\gamma(x - x_0))$$

$$\partial_t\phi_{CD}(0, x, y) = -v\gamma\partial_x\phi_{(\pm\nu,0,\pm\nu)}(x)$$

where $\gamma = \frac{1}{\sqrt{1-v^2}}$ is a Lorentz factor and $x_0$ is the initial position of the Domain Wall. Since we consider neutral Domain Walls we have $A_i = 0$ and $\partial_t A_i = 0$. An example of such Cauchy data is shown in figure 3.9.

[5]Notice that, as shown in figure 3.8c, if $R < 0.8R_0$ then $v = |\dot{R}| > 0.6$. For higher dimensions the Domain Wall's speed increases faster and it becomes relativistic at bigger radius.

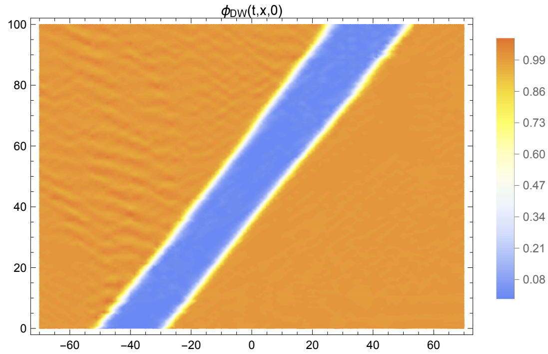


Figure 3.10.: Field configuration $\phi(t,x)$ for the boosted $(-\nu, 0, \nu)$-Domain Wall. Here $m_h = 1$, $l = 40$, $v = 0.8$ and $x_0 = -40$. Observe that the change in the width of the Coulomb vacuum layer, $\Delta l$ is negligible in comparison to $l$.

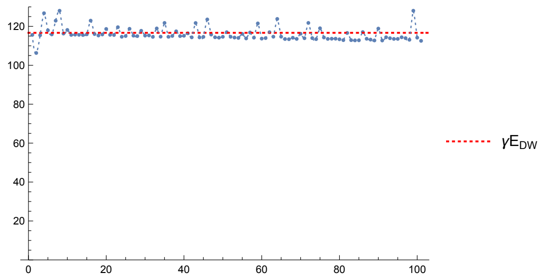


Figure 3.11.: Time evolution of the total energy for the boosted $(-\nu, 0, \nu)$ Domain Wall. Here $m_h = 1$, $l = 40$, $v = 0.8$ and $x_0 = -40$. The total energy for this configuration is expected to be $\gamma E_{DW} = 116.66$. For time scales $\mathcal{O}(100 m_h^{-1})$, we observe that this configuration is metastable

We discussed the Domain Wall classical stability in $(1+1)$ dimensions in terms of the stability of the parameter $l$. Since we are interested in Domain Walls that are stable during the interaction whit the vortex, we will consider $l$ big enough such that the change of the with, $\Delta l$, is negligible during the interaction time. This can be estimated numerically as shown in figure 3.5 and 3.6. For time scales of order $\mathcal{O}(10^2 m_h^{-1})$ we found that $40 m_h^- 1 \lessapprox l$ is an acceptable bound. We confirm this estimation in $(2+1)$ dimension proceeding similarly as in $(1+1)$-dimensions. As a stability criteria, we study the evolution of the total energy

$$m_{DW} = 2\sigma_{DW} L_{DW} = \lambda \nu^4 L_{DW},$$

where $L_{DW}$ is the length of the Domain Wall. Figure 3.10 shows the time evolution of the Domain Wall section for $y = 0$, and figure 3.11 time evolution of the total energy, $m_{DW}$. The initial conditions we used are shown in figure 3.9. We conclude that that our bound–$40 m_h^{-1} \lessapprox l$–applies also to $(2+1)$ dimensions.

# 4. Vortex Lines

As it was disccussed in the sections 1.2.2, and 2.2.3, vortex lines–or cosmic strings–arise in models in which the vacuum manifold $\mathcal{M}$ is not simply connected. This is the case of the $\phi^6$-model, with Lagrangian 2.3, and $\pi_1(\mathcal{M}_\mathrm{H}) = \mathbb{Z}$ (see equation 2.10). Consequently, vortex lines are part of the spectrum of the $\phi^6$-model, and they arise in the Higgs phase. Each homotopy class of $\pi_1(\mathcal{M}_\mathrm{H})$ corresponds to a different *winding number*, $n$, of different vortex solution. These solutions are similar to the the Nielsen-Olesen [18] vortex lines that arise in the abelian-Higgs model. Lets discuss now the corresponding field profile configurations.

## 4.1. Topological Charge: the Winding Number

A map $g : S^m \to S^m$, $\theta \mapsto g(\theta)$, is characterised by an integer number, $n$, that represents the number of times the domain wraps around the range of $f$. $n$ is known as the degree of $g$. In the case $m = 1$, $n$ is known as the *winding number*, and corresponds to the homotopy class of $g$: $n = [g] \in \pi_m(S^m) = \mathbb{Z}$. For details, we refer the reader to chapter 7 of [3]. Other useful bibliography can be [37] or [38].

$$n = \frac{1}{2\pi i v^2} \oint dx^i \phi^* \partial_i \phi,$$

and magnetic flux

$$n = \frac{e}{2\pi} \int B d^2 x,$$

B confinement

## 4.2. Field Profile Configuration

We look for field configurations with finite energy, that asymptotically approach the Higgs Phase, and winds around $\mathcal{M}$ $n$ times. As a first approach, we look for static cylindrical-symmetric solutions $(\phi, A_\mu)$ in the temporal gauge $A_0 = 0$. The energy functional 2.6 then becomes

$$E[\phi, A_\mu] = \int d^2 x \left[ \frac{1}{4} F_{ij} F^{ij} + (D_i \phi)^* D_i \phi + V(\phi) \right] \tag{4.1}$$

The requirement that 4.1 is finite, and that asymptotically the system is in the Higgs phase, implies that

$$|\phi| \to v, \text{ as } r \to \infty.$$

Then, for sufficiently large radius $r$, the modulus of $\phi$ approximates $\nu$, but the phase of $\phi$ may depend on the polar angle $\theta$:

$$\mathrm{Arg}(\phi) = g(\theta).$$

The corresponding winding number[1] of $g$ is invariant under smooth gauge transformations. Moreover, the winding number is a topological number characterizing the field configuration, and it is an integral of motion[3]. In fact, the winding number can be written as

$$n = \lim_{r\to\infty} \frac{1}{2\pi i \nu^2} \oint_{C_r} dx^i \frac{1}{2} \left(\phi^* \partial_i \phi - \phi \partial_i \phi^*\right) \tag{4.2}$$

where $C_r$ is the circle of radius $r$, and centered at the origin. The gauge invariance is now explicit. On the other hand, one can show that two field configurations with the same winding number differ by a phase factor with winding number zero[3]. Consequently, field configurations with a fixed winding number $n$ are (asymptotically) equivalent up to a smooth gauge transformations. For a given configuration with winding number $n$, we can perform a gauge transformation such that the argument of $\phi$ is chosen to be $g(\theta) = n\theta$. This means that asymptotically, for a fixed polar angle $\theta$, the scalar field approaches the Higgs phase (equation 2.7) as:

$$\phi \to \nu e^{ig(\theta)} = \nu e^{in\theta}, \text{ as } r \to \infty. \tag{4.3}$$

In addition, the finiteness of 4.1 implies that, asymptotically, $|D_i\phi|$ must decrease faster than $\frac{1}{r}$. Since

$$\partial_i \phi \to \left(\nu e^{in\theta}\right) \left(-\frac{in}{r} \epsilon_{ij} n_j\right),$$

where $\epsilon_{ij}$ is the antisymmetric tensor with $\epsilon_{12} = 1$, and $n_i = \frac{x_i}{r}$; then

$$A_i \to \frac{1}{e} \partial_i g(\theta) = -\frac{n}{er} \epsilon_{ij} n_j, \text{ as } r \to \infty. \tag{4.4}$$

Notice that, the asymptotic behaviour of $A_\mu$ is pure gauge, and that $F_{ij}$ decreases faster than $\frac{1}{r^2}$.

The asymptotic conditions 4.3, and 4.4 are invariant under spatial rotations and global phase transformations of $\phi$. Therefore, the most general–up to gauge transformations–invariant ansätze for the field profiles are:

$$\phi(r,\theta) = \nu e^{in\theta} F(r), \tag{4.5}$$

$$A_i(r,\theta) = -\frac{n}{er} \epsilon_{ij} n_j A(r), \tag{4.6}$$

[1] A map $g : S^m \to S^m$, $\theta \mapsto g(\theta)$, is characterised by an integer number, $n$, that represents the number of times the domain wraps around the range of $f$. $n$ is known as the degree of $g$. In the case $m = 1$, $n$ is known as the *winding number*, and corresponds to the homotopy class of $g$: $n = [g] \in \pi_m(S^m) = \mathbb{Z}$. For details, we refer the reader to chapter 7 of [3]. Other useful bibliography can be [37] or [38]).

where $F(r)$, and $A(r)$ are smooth numerical functions that have the following asymptotic behaviour:

$$F(r) \to 1,$$
$$A(r) \to 1.$$

Moreover, the requirement that the fields are smooth at 0 implies that:

$$F(0) = 0,$$

$$A(0) = 0.$$

Substituting the ansätze 4.5, and 4.6 in the field equations 2.4, and 2.5, we find the following system of equations for $A(r)$ and $F(r)$:

$$\begin{aligned} 0 = & -rF''(r) - F'(r) + \frac{(1-A(r))^2}{r} n^2 F(r) \\ & + \frac{m_h^2}{4} rF(r)\left(F(r)^2 - 1\right)\left(3F(r)^2 - 1\right) \end{aligned} \tag{4.7}$$

$$0 = -\frac{A''(r)}{r} + \frac{A'(r)}{r^2} - \frac{m_v^2}{r}(1 - A(r))F(r)^2 \tag{4.8}$$

Solutions to the equations 4.7, and 4.8 determine the field profiles 4.5, and 4.6, which we will refer to as the *Vortex Profiles*. Analytical solutions for $F$, and $A$ are not known so far, but approximate solutions for small and large $r$ can be found as we discussed bellow.

### 4.2.1. Behaviour for $r \to \infty$

For the limit $r \to \infty$, we redefine the functions $A$, and $F$ as $A(r) = 1 - a(r)$, and $F(r) = 1 - f(r)$. Then, the equations 4.7, and 4.8 can be linearized–by taking the leading order terms in $a$, and $f$ –as:

$$f''(r) + \frac{f'(r)}{r} - m_h^2 f(r) = 0$$
$$a''(r) - \frac{a'(r)}{r} - m_v^2 a(r) = 0$$

These equations can be solved in terms of the modified Bessel functions of the second kind $K_n(z)$. The solutions are then:

$$\begin{aligned} F(r) &\approx 1 - K_0(m_h r) \approx 1 - \mathcal{O}\left(\frac{e^{-m_h r}}{\sqrt{r}}\right) \\ A(r) &\approx 1 - m_v r K_1(m_v r) \approx 1 - \mathcal{O}\left(\sqrt{r} e^{-m_v r}\right) \end{aligned} \tag{4.9}$$

However, the asymptotic approximation 4.9 is valid if $m_h \leq 2m_v$. If $m_h > 2m_v$, a more accurate analysis is required. Expanding 4.7, and 4.8 up to second order in $a$, and $f$, the equations 4.7, and 4.8 become:

$$f''(r) + \frac{f'(r)}{r} - m_h^2 f(r) + \frac{9}{2} m_h^2 f(r)^2 + \frac{n^2 a(r)^2}{r^2} = 0 \tag{4.10}$$

$$a''(r) - \frac{a'(r)}{r} - m_v^2 a(r) + 2m_v^2 a(r) f(r) = 0 \tag{4.11}$$

As discussed by Perivolaropoulos in [39], if $m_h > 2m_v$ the last term of 4.10 is not small compared to the other terms of the equation. In consequence, to study the asymptotic behaviour of the vortex solution, we consider the following ansatz:

$$\begin{aligned} f(r) &= \left( c_{f_0} + \frac{c_{f_1}}{r} + \mathcal{O}\left(\frac{1}{r^2}\right) \right) r^{\alpha_f} e^{-\gamma_f r} \\ a(r) &= \left( c_{a_0} + \frac{c_{a_1}}{r} + \mathcal{O}\left(\frac{1}{r^2}\right) \right) r^{\alpha_a} e^{-\gamma_a r} \end{aligned} \tag{4.12}$$

where $c_{a_0}$, $c_{a_1}$, $c_{f_0}$, $c_{f_1}$ are non-zero constant coefficients and $\alpha_a$, $\gamma_a$ and $\alpha_f$, $\gamma_f$ determine how fast $a$ and $f$ approach 0, respectively. As we discuss in the appendix A.2, the constants $c_{a_0}$, and $c_{a_1}$ constraint $c_{f_0}$, $c_{f_1}$, and we conclude that the functions $A$ and $F$ can be asymptotically approximated in terms of two parameter family of solutions.

Depending on the values of $m_h$ of $m_v$, the $\phi^6$-model can be in two different regimes, and the asymptotic approximations for $A$ and $F$ are different–as we present below.

- Regime $m_h \leq 2m_v$:

$$\begin{aligned} A(r) &= 1 - c_{a_0} \sqrt{r} e^{-m_v r}, \\ F(r) &= 1 - c_{f_0} \frac{e^{-m_h r}}{\sqrt{r}}, \end{aligned} \tag{4.13}$$

  where $c_{a_0}$ and $c_{f_0}$ are the independent parameters. The core of the vortex has two characteristic lengths: $m_h^{-1}$ and $m_v^{-1}$. The first corresponds to the size of the scalar field profile, while the second corresponds to the size of the vector field profile.

- Regime $m_h > 2m_v$:

$$\begin{aligned} A(r) &= 1 - \left( c_{a_0} \sqrt{r} e^{-m_v r} + c_{a_1} \frac{e^{-m_v r}}{\sqrt{r}} \right), \\ F(r) &= 1 - \left( c_{f_0} \frac{e^{-2m_v r}}{r} + c_{f_1} \frac{e^{-2m_v r}}{r^2} \right), \end{aligned} \tag{4.14}$$

  where

$$c_{f_0} = \frac{c_{a_0}^2 n^2}{m_h^2 - 4m_v^2},$$

$$c_{f_1} = \frac{2c_{a_0}(c_{a_0}m_v + c_{a_1}(m_h^2 - 4m_v^2))n^2}{(m_h^2 - 4m_v^2)^2}.$$

In this regime, $c_{a_0}$, and $c_{a_1}$ are the independent parameters. We highlight that the characteristic lengths of the scalar, and the vector field profiles of the vortex are $(2m_v)^{-1}$, and $m_v^{-1}$, respectively. Thus, their size are not independent from each other and are of order $\mathcal{O}(m_v^{-1})$.

### 4.2.2. Behavior for $r \to 0$

For the limit $r \to 0$, $A(r)$ and $F(r)$ can be approximated by polynomials:

$$F(r) = \sum_{i=1}^{N} b_i r^i,$$

$$A(r) = \sum_{i=1}^{N} c_i r^i,$$

where $c_i$, and $b_i$ are constant coefficients for $i = 1, \dots, N$, and $N$ is sufficiently large. Substituting this ansatz in 4.8 and 4.7, and requiring the leading order to be zero, we find the following approximations for $A$ and $F$ for different winding numbers $n$:

$$\begin{aligned} F(r) &= br^n + \frac{b\left(m_h^2 - 8cn^2\right)}{16(n+1)} r^{n+2}, \\ A(r) &= cr^2 - \frac{b^2 m_v^2}{4n(n+1)} r^{2n+2}, \end{aligned} \tag{4.15}$$

where $b$, and $c$ are independent parameters, and depend on $n$. Moreover, note that $b$ has different dimensionality for different $n$. Note also that $F$ has an n-th order zero at 0. We conclude that, for $r \to 0$, it is also truth that $A$ and $F$ can be approximated by two parameter family of solutions, as we discussed in the limit $r \to \infty$. This conclusion is crucial for finding numerical approximations to the field profiles, as we discuss in the next section.

## 4.3. Numerical Approximations to the Vortex Profiles

For intermediate values of $r$, explicit solutions to the equations 4.8 and 4.7 are not known, but approximate solutions can be obtained numerically. We have found these solutions for different parameters of the theory, using the shooting method that we describe in the appendix A.3. Figure 4.1 shows an example of the numerical solutions $A$, and $F$, and the asymptotic analytical approximations.

Proceeding as it is described in the appendix, we found the numerical approximations to the functions $A$, and $F$ for different parameters of the theory, $(m_v, m_h, n)$. In what

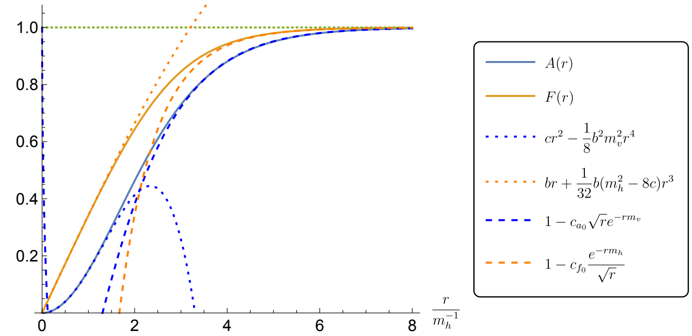


Figure 4.1.: Analytical approximations to the Vortex profile functions $F$ and $A$. The approximations are given by the equation 4.13 for $r \to \infty$, and the equation 4.15 for $r \to 0$. In this example, $m_h = 1$, $m_v = 1$ and $n = 1$. We found that the independent parameters are $b = 0.346$, $c = 0.163$, $c_{a_0} = 3.23$, and $c_{f_0} = 6.86$.

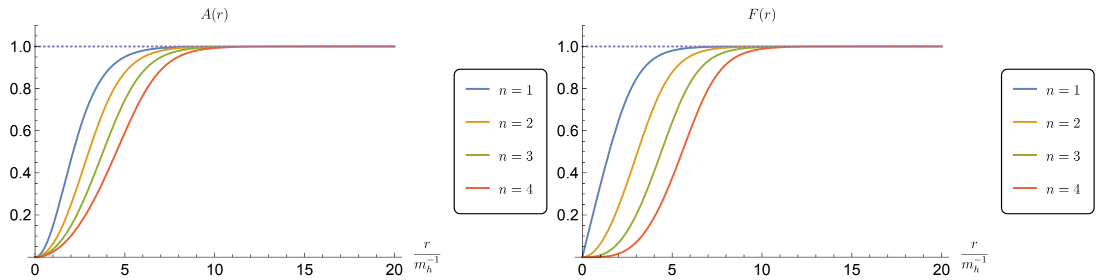


Figure 4.2.: Numerical approximations to the Vortex profile functions $A$, and $F$, when $m_h = 1$, and $m_v = 1$. Here, the dependence of the core size on the winding number, $n$, can be observed. Note also that the asymptotic behaviour of $A(r)$ and $F(r)$ does not depend on $n$, as it is expected from equation 4.13.

follows we have set $v = 1$ unless stated otherwise. We present some of the approximations that we found for different masses regimes. We refer the reader to the chapter 5 for more details in the numerical simulation of the time evolution.

### Regime $m_h \leq 2m_v$:

Figure 4.2 shows the numerical approximations for the case $m_h = 1$, and $m_v = 1$, while figure 4.3 shows the case $m_h = 1$, and $m_v = 10$. Different colors correspond to different winding numbers $n = 1, 2, 3, 4$. The analytical approximations for $r \to 0$ , and $r \to \infty$, and the corresponding numerical coefficients are presented in the tables A.1 and A.2.

### Regime $m_h > 2m_v$

The figure 4.4 shows the numerical approximations for the case $m_h = 1$, and $m_v = 0.1$, for $n = 1, 2, 3, 4$. The asymptotic behaviour and the corresponding numerical coefficients

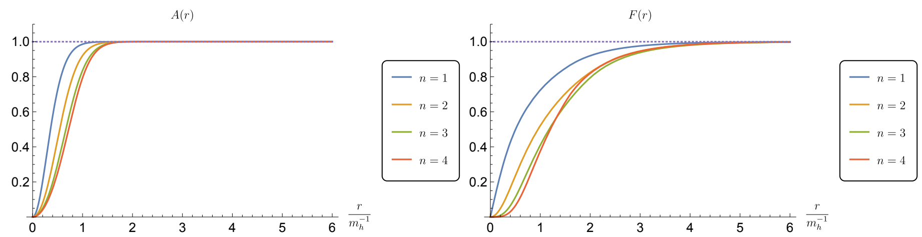


Figure 4.3.: Numerical approximations to the Vortex profile functions $A$, and $F$, when $m_h = 1$, and $m_v = 10$, for different winding numbers $n$.

are presented in the table A.3.

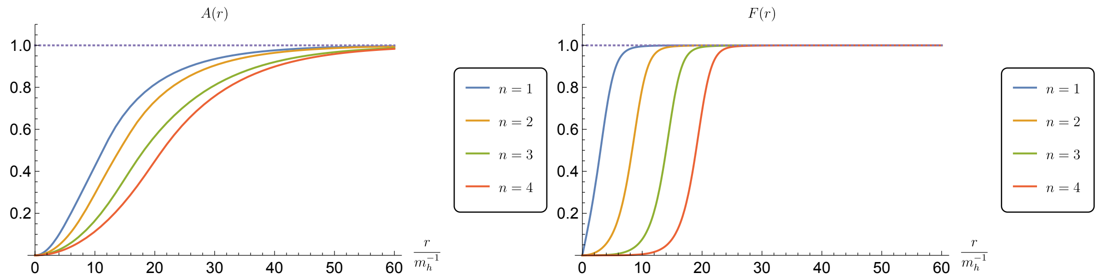


Figure 4.4.: Vortex Profiles for $m_h = 1$, and $m_v = 0.1$. Comparing this profiles to the profiles shown in figure 4.2, the gauge core size increases, as it expected, approximately 10 times. On the other hand, note that the scalar core size is bigger than the one found in the previous regime increases with $n$

### 4.3.1. Numerical Stability

The vortex solutions 4.5, and 4.6 are static, and stationary solutions to the field equations 2.4, and 2.5. These solutions are topologically protected. Thus, they are classically stable under small perturbations. On the other hand, the numerical approximations to the vortex solutions are not exact solutions, and can be treated as perturbations of the vortex field configuration. We are interested in the classical evolution of the vortex configuration, thus it is necessary to determine how stable the approximated solutions are.

To determine the stability of the approximated solutions, we proceed to simulate numerically the time evolution of the fields $\phi$, and $A_\mu$. We used the approximate vortex profiles as initial condition. Following, we determined the stability of a solutions in terms of the stability of the vortex mass, $m_{\text{vo}}$, and its winding number, $n$. $m_{\text{vo}}$, and $n$ are conserved quantities. However, numerically these quantities may vary over time in a finite region. If the relative errors of $m_{\text{vo}}$, and $n$ decrease over time, and they are smaller than the numerical relative error of the simulation[2], then we consider that the corresponding approximate solutions is stable under time evolution. We describe bellow the details of this criteria.

*The Vortex Mass:*

$m_{\text{vo}}$ is obtained by replacing 4.5, and 4.6 in 2.6, and integrating the energy density over all space. Under time evolution, $m_{\text{vo}}$ is constant. Moreover, since the field configuration is static, if the energy integral is done over a finite region, its value is also constant. We perform the energy integral numerically at different times, and for a finite region inside which the vortex is localised. We denote by $m_{\text{vo}}(t)$ the value of the integral at time $t$. The mean value of $m_{\text{vo}}(t)$ over time is

$$\langle m_{\text{vo}}(t)\rangle = \frac{1}{t}\int_0^t dt' m_{\text{vo}}(t').$$

If the relative error

$$\Delta_{m_{\text{vo}}}(t) = \sqrt{\frac{\langle m_{\text{vo}}(t)\rangle^2 - \langle m_{\text{vo}}(t)^2\rangle}{\langle m_{\text{vo}}(t)\rangle^2}}$$

decreases over time, then the energy is approximately conserved inside the region of integration, and we conclude that the $m_{\text{vo}}$ is stable under time evolution. On the contrary, if $\Delta_{m_{\text{vo}}}$ increases, it means that $m_{\text{vo}}$ is not constant on the region of integration, and thus we can conclude that approximated solution is not static. The second requirement–for which $\Delta_{m_{\text{vo}}} \sim \mathcal{O}(10^{-3})$–is motivated by the acceptable numerical error of our simulations. In general, however, this requirement can be improved.

*The Winding Number:*

$n$ can be computed by two different methods. In the first method, $n$ is computed in terms of the field $\phi$–by equation 4.2. In the second method, $n$ is computed in terms of the magnetic field, $B$, while using the fact that the $n$ is proportional to the magnetic flux[3]. We can rewrite the ansatz 4.6 as

$$A_i(r,\theta) = \frac{n}{e}A(r)\partial_i\theta.$$

The corresponding magnetic field, has norm

$$B(r,\theta) = \frac{n}{er}\partial_r A(r). \tag{4.16}$$

Thus, using the Stokes theorem, the winding number can be computed as

$$\begin{aligned} n &= \lim_{r\to\infty}\frac{e}{2\pi}\oint_{C_r} dx^i A_i(x,y) \\ &= \frac{e}{2\pi}\int d^2x B(x,y). \end{aligned} \tag{4.17}$$

[2]The numerical relative error for our simulations is $\mathcal{O}(10^{-3})$

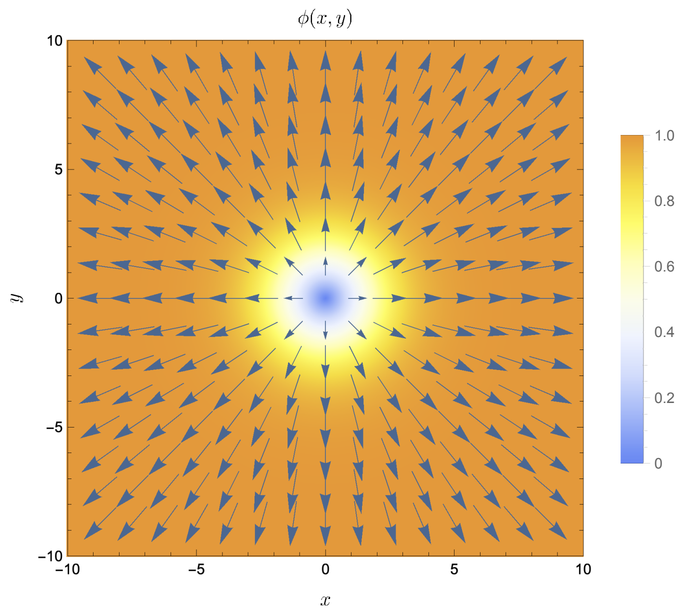


Figure 4.5.: Vortex field configuration for the field $\phi$–equation 4.5. Here $n = 1$, $m_h = 1$, $m_v = 1$, and $n = 1$. The vector at the point $(x, y)$ has components $(\text{Re}(\phi(x, y)), \text{Im}(\phi(x, y)))$. Consequently, the direction of each vector represents the phase $Arg(\phi(x, y))$, while the colour represents the norm $|\phi(x, y)|$.

Numerically, the first method can be carried out if the integral is computed over a circumference $C_r$ of radius $r$ sufficiently large. For the second method, the integral 4.17 can be computed over the region bounded by $C_r$. We used the second method to determine the winding number at different times in terms of the magnetic flux. We denote by $n(t)$ the value of the numerical integral at time $t$, and its mean value over time by $\langle n(t) \rangle$. Analogous to the discussion of the vortex mass, if the relative error $\Delta_n(t)$ decreases over time, then the magnetic flux is approximately conserved on the region of integration, and we conclude that $n$ is stable under time evolution. Finally, we used as stability criteria whether or not the approximate solutions conserve $m_{\text{vo}}$, and $n$ in the region inside which the vortex is localised

We recall the reader that our purpose is to study the vortex-unwinding while encountering a Coulomb vacuum layer, and the classical time evolution of the fields during these process. As we will discuss in the next chapter, the time evolution of $m_{\text{vo}}(t)$, and $n(t)$ is different when the vortex interacts with a Coulomb vacuum layer.

### Vortex Time Evolution

Bellow we present the results of the simulation for the vortex profile with $n = 1$, $m_h = 1$ and $m_v = 1$. Figures 4.5, and 4.6 show the vortex profiles for $\phi$ and $A_\mu$, respectively. These field configurations were used as the initial conditions of the fields, and $\partial_t A_i = 0$, and $\partial_t \phi = 0$ as initial conditions of the time derivative of the fields. The figure 4.7 shows

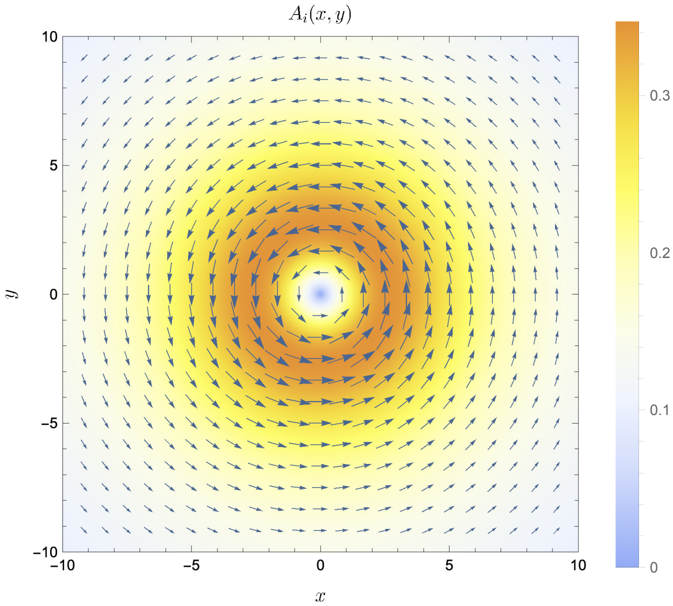


Figure 4.6.: Vortex field configuration for the field $A_\mu$–equation 4.6. . Here $e = 1/\sqrt{2}$, $m_h = 1$, $m_v = 1$, and $n = 1$.The vector at the point $(x, y)$ has components $(A_1(x, y), A_2(x, y))$. The colour represents the norm $|A_i(x, y)|$

the corresponding energy density, and magnetic field. The white circumference has radius $r = 10$, and determines the region of integration of $m_{\text{vo}}(t)$, and $n(t)$.

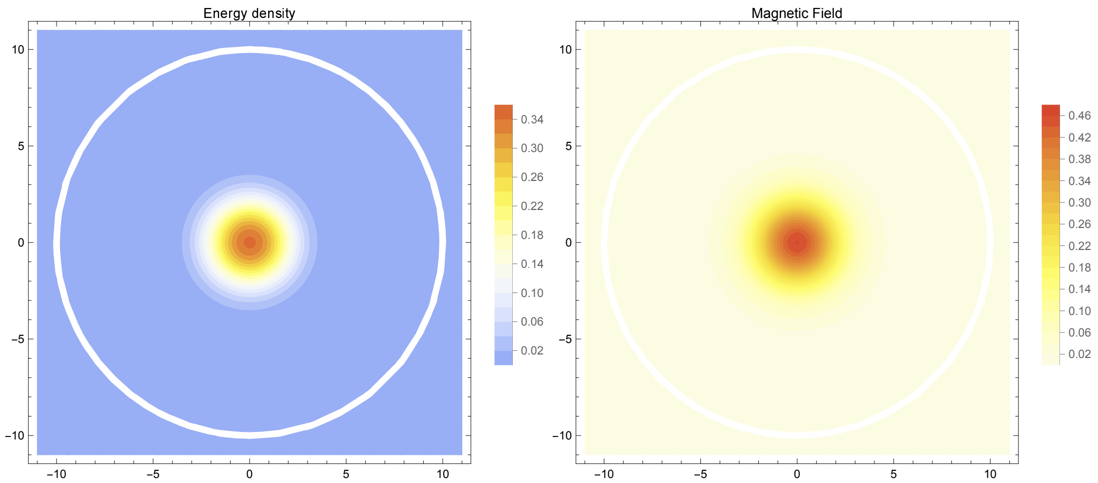


Figure 4.7.: Energy density, $E[\phi, A_\mu]$, and magnetic field, $B$, of a Vortex with winding number $n = 1$. Here $m_h = 1$, and $m_v = 1$. The white circumference has radius $r = 10$, and determines the region of integration, $C_r$.

Figures 4.8, and 4.9 show the field configurations of $\phi$, and $B$ at different times $t$ of the simulation. Figure 4.10 shows the total energy, $m_{\text{vo}}(t)$, and the relative error $\Delta_{m_{\text{vo}}}(t)$.

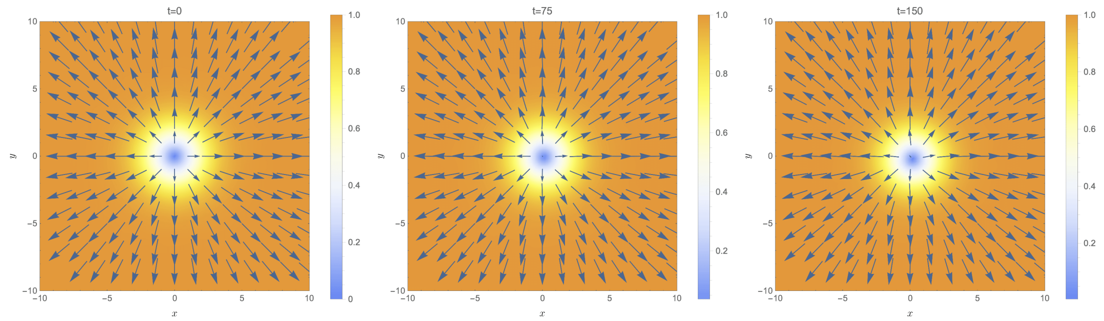

Figure 4.8.: Scalar field, $\phi$, at different times $t$, for the time evolution of a Vortex with winding number $n = 1$. Here $m_h = 1$, and $m_v = 1$.

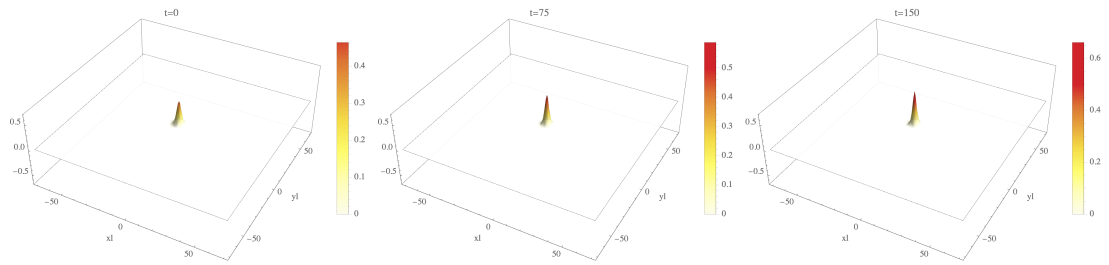

Figure 4.9.: Magnetic field, $B$, at different times $t$, for a Vortex with winding number $n = 1$. Here $m_h = 1$, and $m_v = 1$.

At $t_{max} = 150$, we obtained $m_{\text{vo}}(t_{max}) = 5.18$, and $\Delta_{m_{\text{vo}}}(t_{max}) = 5.0 \times 10^{-3}$. Similarly, figure 4.11 shows the winding number, $n(t)$, and the relative error $\Delta_n(t)$. At $t_{max} = 150$, we obtained $n = 1 - 4.63 \times 10^{-4}$, and $\Delta_n(t_{max}) = 3.4 \times 10^{-4}$. As mentioned before, the bound for the relative error can be decreased, for instance, if we consider a bigger region of integration $C_{r'}$, with $r' = 480$,the relative error decreases to $\mathcal{O}(10^{-7})$. According to the criteria that we explained before, we conclude that, for the approximated solution, the energy and winding number are stable in $C_r$.

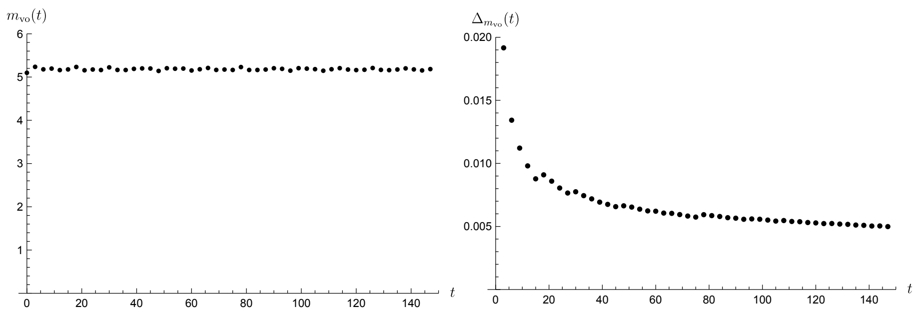


Figure 4.10.: Total energy, $m_{\text{vo}}(t)$, and relative error $\Delta_{m_{\text{vo}}}(t)$, at different times of a vortex-evolution simulation. Here $n = 1$, $m_h = 1$, and $m_v = 1$. Observe how the relative error decreases in time, indicating that the total energy is conserved in the region of integration, $C_{10}$.

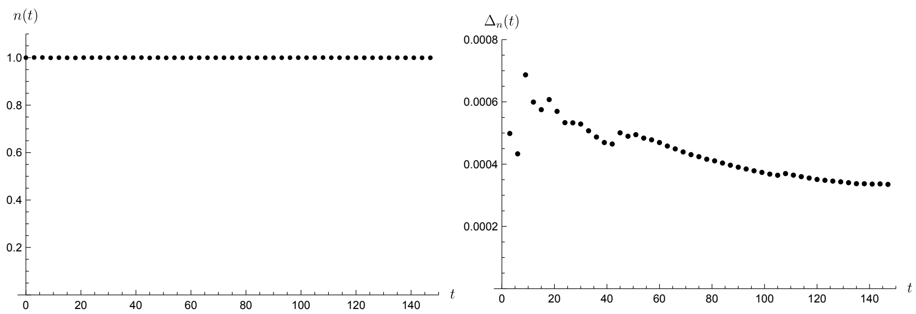


Figure 4.11.: Winding number, $n(t)$, and relative error $\Delta_n(t)$, at different times of a vortex-evolution simulation. Here, $m_h = 1$, $m_v = 1$, and the winding number of the initial conditions is $n = 1$. Observe how the relative error decreases in time, indicating that the winding number, calculated from the magnetic flux, is conserved in the region of integration, $C_{10}$.

# 5. Erasure of Vortex by a Coulomb Vacuum Layer

In chapters 3, and 4, we presented the different Domain Walls, Vacuum Layers, and Vortex solutions that are part of the spectrum of the $\phi^6$-model, 2.3. In this chapter, we investigate the erasure of a vortex by a Coulomb Vacuum layer sweeping. We simulate the collision of a Vortex with a $(-\nu, 0, \nu)$-Domain Wall, for different parameters of the model, $(m_h, m_v, n, l)$. Within this approach, one can observe how the collision leads to the unwinding of the scalar field, and the dissipation of the magnetic flux in the core of the Coulomb Vacuum Layer. As a consequence, the topological charge $n$ decreases dissipating in the core of the layer. We observed this same behaviour for different values of the parameters of the model.

In the following link, the reader can find the results of our simulations:

`https://github.com/jusvalbuenabe/TMP-Valbuena`

In the following sections we describe the simulations, and results more in detail. Firstly, we discuss the Cauchy problem, and how to solve the time evolution in gauge theories, and in the $\phi^6$ model. Secondly, we describe the Cauchy Data we used to approximate the initial conditions of the Vortex-Coulomb Vacuum Layer configuration. Thirdly, we present the results of the simulations, and finally describe the erasure of defects mechanism in the $\phi^6$-model.

## The Cauchy Problem

In general the formulation of the Cauchy Problem in gauge theories is not trivial. The reason is that the gauge redundancy allows the existence of different solutions to the field equations with the same *Cauchy data*, or initial conditions. Then, if one wants to avoid the ambiguity in the solutions, it is necessary to fix the gauge redundancy. The time gauge, in which $A_0 = 0$ for every time and position, is convenient for solving time evolution problems. Thus, we use the time gauge to numerically solve the field equations 2.4, and 2.5.

For the time gauge, the *Cauchy data*–$(A_i,\ \partial_t A_i,\ \phi,\ \partial_t \phi)$–or initial conditions must satisfy the Gauss constraint

$$D_i F^{i0} = j^0 \tag{5.1}$$

at $t = 0$. Then, the field equations can be integrated to evaluate $A_i$, and $\phi$ at $t > 0$.

Proceeding in this way, after fixing the time gauge, the field equations 2.4, and 2.5 become:

$$\begin{aligned}
\partial_t^2\phi &= \partial_i\partial_i\phi - 2ieA_i\partial_i\phi - \left[e^2A_iA_i + ie\partial_iA_i\right]\phi \\
&\qquad - \left[\lambda^2\nu^4 - 4\lambda^2\nu^2\left|\phi\right|^2 + 3\lambda^2\left|\phi\right|^4\right]\phi, \\
\partial_t^2A_x &= \partial_y^2A_x - \partial_x\partial_yA_y - 2e\left|\phi\right|^2A_x + 2\mathrm{Im}\left[\phi^*\partial_x\phi\right], \\
\partial_t^2A_y &= \partial_x^2A_y - \partial_y\partial_xA_x - 2e\left|\phi\right|^2A_y + 2\mathrm{Im}\left[\phi^*\partial_y\phi\right].
\end{aligned} \tag{5.2}$$

The integration of the system of partial differential equations 5.2 gives the time evolution for a given Cauchy Data. General analytical solutions for this system are not known. However, approximate solutions can be found by numerical simulations. We implemented this approach using the finite elements method. The simulations allowed us to study the Vortex, and Domain Walls stability separately, and their interactions.

## 5.1. The Vortex-Coulomb Vacuum Layer Configuration

Lets denote the vortex field configuration 4.5, and 4.6 by $\phi_{\mathrm{vo}}(x,y)$, and $A_{i\mathrm{vo}}(x,y)$, respectively. On the other hand, the Coulomb vacuum layer configuration we will consider is given by $\phi_{(-\nu,0,\nu)}(x)$–equation 3.12. We remark here that this Domain Wall has not electric charge. To simulate the Vortex-Coulomb Vacuum Layer interaction, we consider the following ansatz to approximate the initial conditions:

$$\begin{aligned}
\phi_{\text{vo-dw}}(x,y) &= \phi_{(-\nu,0)}\left((x+L_{\mathrm{vd}}) + \frac{l}{2}\right) \\
&\quad + \left(\frac{\phi_{(0,\nu)}\left((x+L_{\mathrm{vd}}) - \frac{l}{2}\right)}{\nu}\right)\phi_{\mathrm{vo}}(x,y),
\end{aligned} \tag{5.3}$$

$$A_{i\text{vo-dw}}(x,y) = \left(\frac{\phi_{(0,\nu)}\left((x+L_{\mathrm{vd}}) - \frac{l}{2}\right)}{\nu}\right)A_{i\mathrm{vo}}(x,y), \tag{5.4}$$

where $L_{\mathrm{vd}}$ is the initial distance between the cores of the vortex, and the Coulomb vacuum layer. For $L_{\mathrm{vd}} \to \infty$, the fields configuration 5.3, and 5.4 reproduce asymptotically the required initial conditions. To observe this limit, consider a region of space $\mathcal{R} = [-L_x, L_x] \times [-L_y, L_y]$ such that

$$\frac{1}{m_h} < L_y \ll L_x \ll L_{\mathrm{vd}}.$$

In the Limit $L_{\mathrm{vd}} \to \infty$, the field configuration for $x > -L_x$ approaches the vortex configuration

$$\lim_{\substack{L_{\mathrm{vd}}\to\infty \\ x>-L_x}} \phi_{\text{vo-dw}}(x,y) = \phi_{\mathrm{vo}}(x,y),$$

$$\lim_{\substack{L_{\text{vd}}\to\infty \\ x>-L_x}} A_{i\text{vo-dw}}(x,y) = A_{i\text{vo}}(x,y).$$

On the other hand, if $x < -L_x$, the field configuration approaches a $(-\nu, 0, e^{i\alpha}\nu)$-Domain Wall configuration centered at $-L_{\text{vd}}$, i.e.

$$\lim_{\substack{L_{\text{vd}}\to\infty \\ x\ll -L_x}} \phi_{\text{vo-dw}}(x,y) = \phi_{(-\nu,0)}\left(x' + \frac{l}{2}\right) + \phi_{(0,\nu)}\left(x' - \frac{l}{2}\right) e^{i\alpha(x,y)},$$

$$\lim_{\substack{L_{\text{vd}}\to\infty \\ x\ll -L_x}} A_{i\text{vo-dw}}(x,y) < A_{i\text{vo}}(-L_x,y) \sim 0,$$

where $x' = x + L_{\text{vd}}$, and $e^{i\alpha(x,y)} = \left(\frac{x+iy}{\sqrt{x^2+y^2}}\right)^n$. Moreover, if $|y| \ll |x|$, then $e^{i\alpha(x,y)} \sim (-1)^n$. Thus,

$$\begin{aligned}\lim_{\substack{L_{\text{vd}}\to\infty \\ x<-L_x \\ |y|<L_y}} \phi_{\text{vo-dw}}(x,y) &= \phi_{(-\nu,0)}\left(x' + \frac{l}{2}\right) + \phi_{(0,(-1)^n\nu)}\left(x' - \frac{l}{2}\right) \\ &= \phi_{(-\nu,0,(-1)^n\nu)}(x').\end{aligned}$$

We conclude that the field configuration $(\phi_{\text{vo-dw}}(x,y), A_{i\text{vo-dw}}(x,y))$, in the limit $L_{\text{vd}} \to \infty$, approaches a Vortex configuration near the origin, and a Coulomb vacuum layer configuration for $x \sim -L_{\text{vd}}$.

In addition, motivated by the fact that domain walls are, in general, very high energetic objects moving through space, we consider an initial relativistic velocity, $v$, of the Coulomb vacuum layer. To do it, we boost the domain walls profiles, i.e

$$\begin{aligned}\phi_{\text{vo-dw}}(t,x,y) &= \phi_{(-\nu,0)}\left(\gamma\left(x' - vt + \frac{l}{2}\right)\right) \\ &\quad + \left(\frac{\phi_{(0,\nu)}\left(\gamma\left(x' - vt - \frac{l}{2}\right)\right)}{\nu}\right)\phi_{\text{vo}}(x,y), \\ A_{i\text{vo-dw}}(t,x,y) &= \left(\frac{\phi_{(0,\nu)}\left(\gamma\left(x' - vt - \frac{l}{2}\right)\right)}{\nu}\right) A_{i\text{vo}}(x,y),\end{aligned} \tag{5.5}$$

where $\gamma = \frac{1}{\sqrt{1-v^2}}$ is the Lorentz factor. Figures 5.1, and 5.2 show an example of the field configuration $\phi_{\text{vo-dw}}(t,x,y)$, and $A_{i\text{vo-dw}}(t,x,y)$ at $t = 0$, respectively. We checked numerically that the fields configuration 5.5 satisfies approximately the Gauss constrain 5.1, allowing us to use it as initial conditions.

## 5.2. Time Evolution

We simulate the interaction of a Coulomb Vacuum Layer with a Vortex, using as initial conditions the field configuration that is shown in figures 5.1, and 5.2. In the simulation,

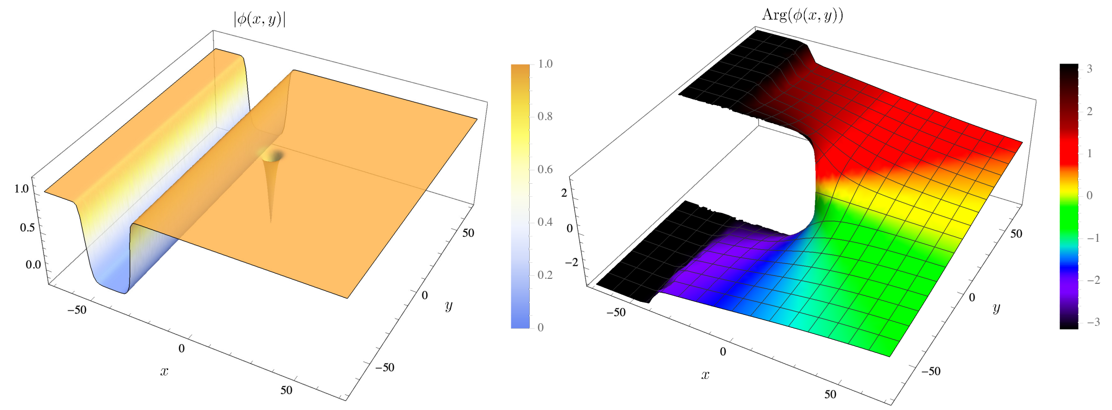


Figure 5.1.: Vortex-Coulomb Vacuum Layer configuration $\phi_{\text{vo-dw}}(t,x,y)$ at $t=0$. Here $\nu=1$, $m_h=1$, $l=40$, $L_{\text{vd}}=40$, and $v=0.8$. On the left, the norm $|\phi|$ is plotted. Observe the Coulomb vacuum layer centered at $x=-40$, and the vortex core at the origin. On the right, the phase $\mathrm{Arg}(\phi)$ is plotted. Observe the winding of the field $\phi$ around the origin. On the other hand, for $x<-40$, the phase is approximately constant, and it is equal to $\pi$.

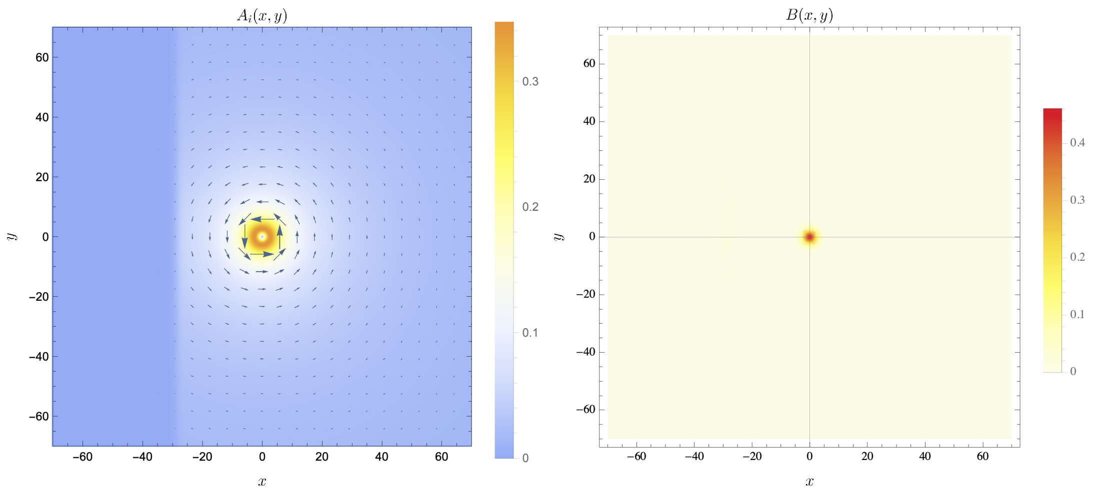


Figure 5.2.: Vortex-Coulomb Vacuum Layer configuration $A_{\text{vo-dw}}(t,x,y)$ at $t=0$. Here $\nu=1$, $m_h=1$, $l=40$, $L_{\text{vd}}=40$, and $v=0.8$. On the left, the vector at a point $(x,y)$ has coordinates $(A_1(x,y),A_2(x,y))$, while the norm $|A_i(x,y)|$ is represented by the background colour. Observe the Coulomb vacuum layer configuration centered at $x=-40$, and the vortex configuration at the origin. On the right, the corresponding magnetic field $B(x,y)$ is plotted.

we observed the unwinding of the scalar vortex when it enters the Coulomb phase, producing two perturbations that travel along the $(0,\nu)$-Domain Wall. In addition, the magnetic field gets unconfined in the Coulomb phase producing radiation modes that are reflected by the $(\nu, 0)$-Domain Wall. Subsequently most of this radiation is confined to the core of the layer. Bellow we present these results, first describing the time evolution for the field $\phi$, and afterwards the evolution of $A_i$, and $B$.

*$|\phi|$ evolution:* Figure 5.3 shows the time evolution of the norm of the scalar field, $|\phi|$. Recall that in the Higgs phase, the degree of freedom corresponding to $|\phi|$ becomes the degree of freedom of the neutral scalar field $h$. On the other hand, in the Coulomb phase, $|\phi|$ is one of the two degrees of freedom of the complex field $\phi$. Observe the Wave modes corresponding to $h$, and $|\phi|$ that are generated as the Domain wall starts to interact with the vortex. As the vortex encounters the Coulomb vacuum layer, two perturbations on the $(0, \nu)$-Domain Wall are produced, and they start propagating in opposite directions along the wall. In figure 5.5, these two travelling perturbations can be appreciated in a clearer way.

If a domain wall evolution is tension dominated, the evolution of perturbations on the wall is effectively described by considering the thin-Wall approximation. Then the total energy will be proportional to the length (or area in $(3+1)$-dimensions) of the wall. The corresponding action is the Nambu-Goto action[4].

$$S = -\sigma \int d\mathcal{A},$$

where $\sigma = \frac{m_h^2}{8\lambda}$ is the tension of the $(\nu, 0)$-Domain Wall, and $d\mathcal{A}$ is the differential area of the world-sheet. It can be shown that the speed of propagation of perturbations on the wall is $c = 1$, as it is observed in our simulations.

*$Arg(\phi)$ evolution:* Figure 5.4 shows the time evolution of the phase of the scalar field, $\text{Arg}(\phi)$. Recall that in the Higgs phase, the degree of freedom corresponding to $\text{Arg}(\phi)$ becomes the longitudinal degree of freedom of the massive vector field $B_\mu$, while in the Coulomb phase $\text{Arg}(\phi)$ is one of the two degrees of freedom of the complex field $\phi$. As the vortex encounters the Coulomb vacuum layer, the norm of the scalar field approaches zero, $|\phi| \sim 0$, and the phase, $\text{Arg}(\phi)$, becomes ill defined. Observe this behaviour, at $t = 33$ in figure 5.4. As a consequence, the phase of the scalar field is allowed to unwind in the Coulomb Vacuum Layer phase.

As the $(\nu, 0)$-Domain-Wall approaches the original position of the vortex, at $t = 70$, the phase at the origin, $\text{Arg}(\phi(t, 0, 0))$, acquires a value corresponding to $\pi$. This coincides precisely with the initial asymptotic phase at $r \to \infty$–see figure 5.1. A more detailed plot of the phase configuration near the origin is shown in figure 5.6.

*$B$ evolution:* The time evolution of the field $A_i$ provides the time evolution of the magnetic field $B$, which is shown in figure 5.7. As the vortex enters the Coulomb layer, the electric current $j^\mu$–that localises the magnetic field on the core of the vortex– approaches zero. In fact, the electric current

$$j^\mu = -i\left(\phi^* D^\mu \phi - (D^\mu \phi)^* \phi\right)$$

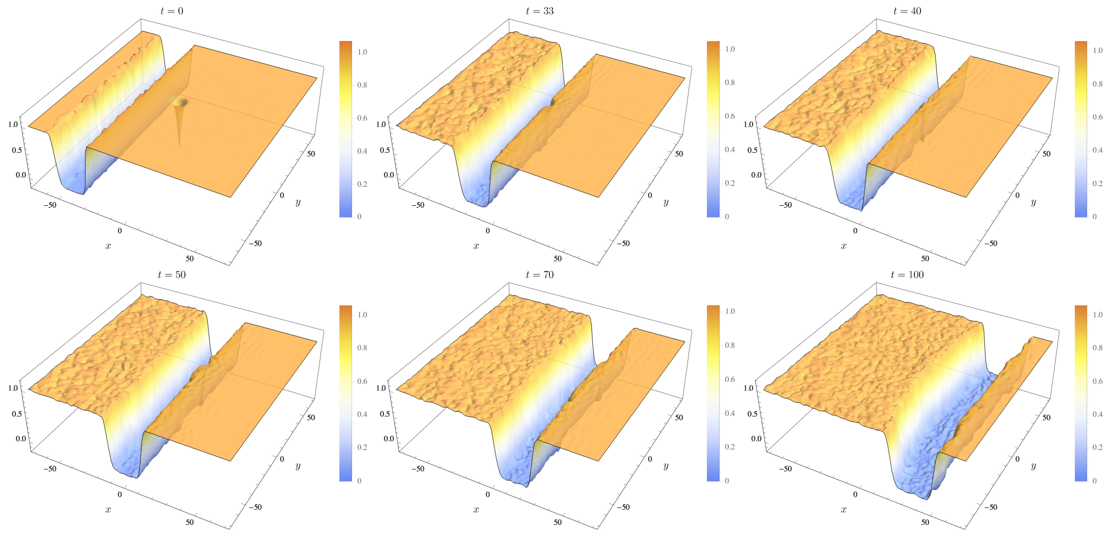

Figure 5.3.: Time evolution of $|\phi|$. The colour represents the value of $|\phi(x,y)|$. The blue regions corresponds to the Coulomb phase, while the orange regions correspondto the Higgs phase-compare to figure 2.2. Observe at $t = 33$, the moment the vortex enters the Coulomb vacuum layer, and two perturbations are generated on the wall. At subsequent times observe how these two perturbations travel along the wall in oposite directions.

is proportional to the norm of the field $|\phi|$. Since $|\phi| \sim 0$ in the core of the Coulomb Vacuum Layer, then $|j^\mu| \sim 0$. We observe this behaviour in our simulations, as it is shown in figure 5.9. Consequently, the field equations, 2.5 become approximately the Maxwell equations in (Coulomb) vacuum. Thus, the magnetic field dissipate in the core of the layer while producing electromagnetic radiation. This behaviour is precisely observed at $t = 40$ in figures 5.7, and 5.8. Afterwards, as the front of the electromagnetic radiation encounters the $(v, 0)$-Domain Wall, it gets reflected. To appreciate this result, we plot the time evolution of the electromagnetic energy density in figure 5.10.

*Energy density evolution:* Figure 5.11 shows the time evolution of the total energy density–2.6.The energy corresponding to the mass of the vortex is dissipated in the Coulomb Vacuum layer by two mechanisms. The first one is the dissipation of energy on the $(0, v)$-Domain Wall carried by two travelling perturbations. The second contributions is the dissipation of electromagnetic energy in the core of the wall.

The first contribution corresponds to the energy density of the scalar field:

$$\mathcal{E}_\phi = (D_0\phi)^* D_0\phi + (D_i\phi)^* D_i\phi + V(\phi),$$

while the second contribution corresponds to the electromagnetic energy

$$\mathcal{E}_{EM} = \frac{1}{2} F_{0i} F_{0i} + \frac{1}{4} F_{ij} F_{ij}.$$

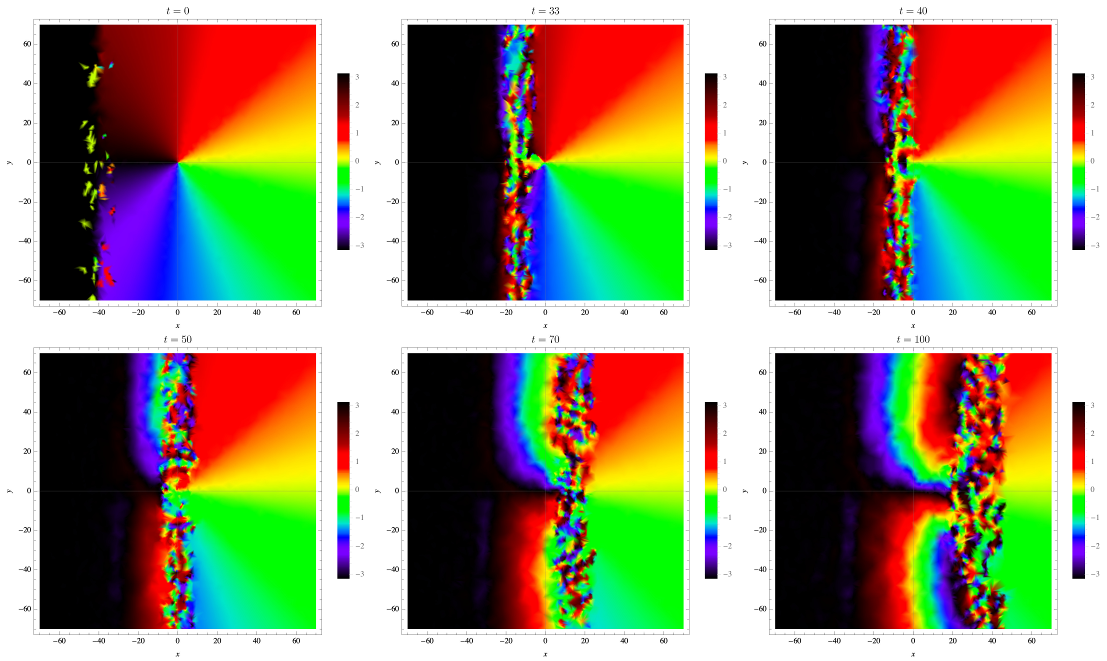


Figure 5.4.: Time evolution of the phase Arg($\phi$). The colours represent the phase value measured in radians. The dark region corresponds to Arg($\phi$) $= \pi$. After the Coulomb Vacuum Layer passes over the vortex at $t = 70$, a phase value $\pi$ is established at the origin. At $t = 100$, no winding is observed.

Figures 5.12, and 5.10 show the time evolution of $\mathcal{E}_\phi$, and $\mathcal{E}_{EM}$, respectively. Observe that at $t = 70$, the energy density is almost constant along the the $(0, \nu)$-Domain Wall, and thus the dynamics of the wall is tension dominated, and its evolution is effectively described by the Nambu-Goto action. On the other hand, the $(\nu, 0)$-Domain Wall reflects the electromagnetic wavefront, and it loses momentum due to the electromagnetic pressure. Consequently, it is red-shifted respect to the $(0, \nu)$-Domain Wall. Form the previous results of our simulations, we conclude that the $m_{\rm vo}$ is dissipated along the Coulomb Vacuum Layer, after the Vortex has been swept.

### 5.2.1. Unwinding of the Vortex: Time evolution of $n$

To describe the unwinding process of the vortex we have numerically computed the time evolution of the winding number $n$, by two different methods. As we described before, the winding number is proportional to the magnetic flux $\Phi_B$–see equation4.17. We used this first method to compute the winding number over a finite region $C_r$. As it is shown in figure 4.11,for $r = 10$, $n(t)$ is constant for the Vortex configuration we are considering. On the other hand, as the vortex is swept away by the Coulomb vacuum Layer, $n_{10}$ decreases, and eventually tends to 0. Figure 5.14 shows precisely this time evolution of $n(t)$. From the simulation results described above, this behaviour is to be

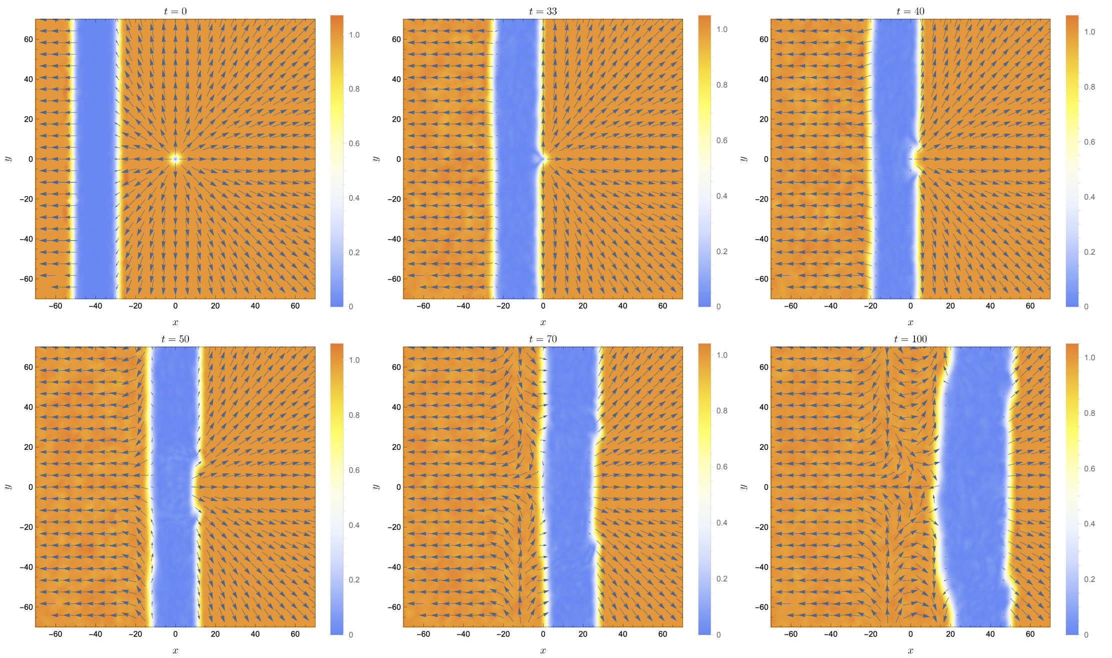

Figure 5.5.: Time evolution of field $\phi$. The vector at a point $(x, y)$ has components $(\mathrm{Re}(\phi(x, y)), \mathrm{Im}(\phi(x, y)))$. The norm $|\phi|$ is represented by the background colour.

expected, since the magnetic field dissipates in the Coulomb vacuum, and its flux is not localised around the origin anymore.

The second method we used to compute the winding number, is in terms of scalar field. From equation 4.2, we define $n_\phi$ as

$$n_\phi = \frac{1}{2\pi i v^2} \oint_{C_r} dx^i \frac{1}{2} \left(\phi^* \partial_i \phi - \phi \partial_i \phi^*\right),$$

where $r$ is a given finite radius. Figure 5.15 shows the time evolution of $n_\phi(t)$, for $r = 10$. We observe that $n_\phi = 1$ at $t = 0$, as it corresponds to the vortex configuration. As the vortex approaches the Coulomb vacuum layer, $n_\phi$ decreases and becomes negative. To understand this behaviour, lets consider the case $t \sim 33$. Notice that $n_\phi(33) \sim 0.5$, and that the $(0, v)$-Domain Wall is localised approximately at $x = 0$–see figure 5.6. As a first approximation, in the boundary of the region of integration $C_r$,

$$\phi(t \sim 33, x, y) \sim \Theta(-x) v e^{in\theta},$$

where $\Theta(x)$ is the step function. Thus, after replacing the approximation for $\phi$, the integral $n_\phi(33)$ becomes $n/2 = 0.5$. As the Coulomb vacuum layer passes over the origin, the winding number $n_\phi$ is not well defined until the $(v, 0)$-domain wall passes over the origin. As we mentioned before, the phase near the origin becomes $\mathrm{Arg}(\phi) \sim \pi$, thus, as a first approximation, in the region of integration $C_r$:

$$\phi(t \sim 100, x, y) \sim -v e^{i\pi},$$

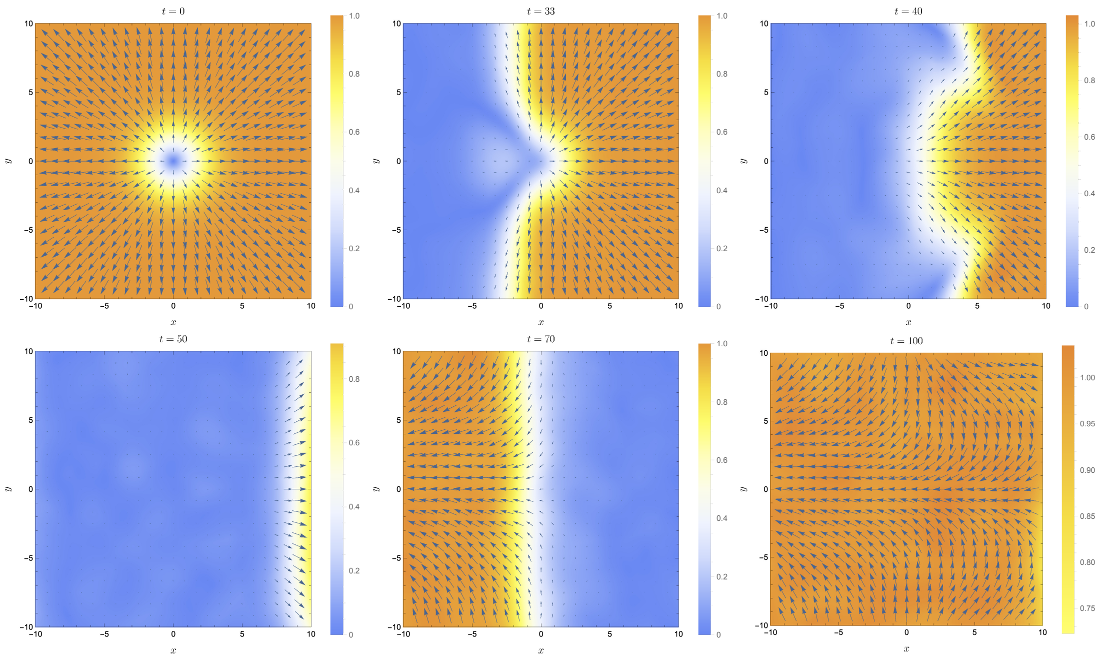


Figure 5.6.: Time evolution of the field configuration $\phi$ near the vortex position. At $t = 0$, the initial vortex configuration is observed. On the other hand, at $t = 100$, no winding of the phase is observed. Compare this evolution to the evolution of the vortex alone–it is shown in figure 4.8.

for $t \sim 100$. Thus the winding number $n_\phi \sim 0$. From the previous results, We conclude that locally the vortex is unwinded once it is swweept by the Coulomb Vacuum Layer.

As a final remark, we observed this same behaviour of vortex unwinding in different regimes of parameters of the $\phi^6$-model, different winding numbers $n$, and different widths of the Coulomb vacuum layer $l$. The results of this simulations can be found in the following web page:

`https://github.com/jusvalbuenabe/TMP-Valbuena`

Our results allow us to conclude that erasure of defects mechanism is born out in the $\phi^6$-model at the classical level, and suggest that this mechanism for the vortex unwinding is independent of the parameters of the model.

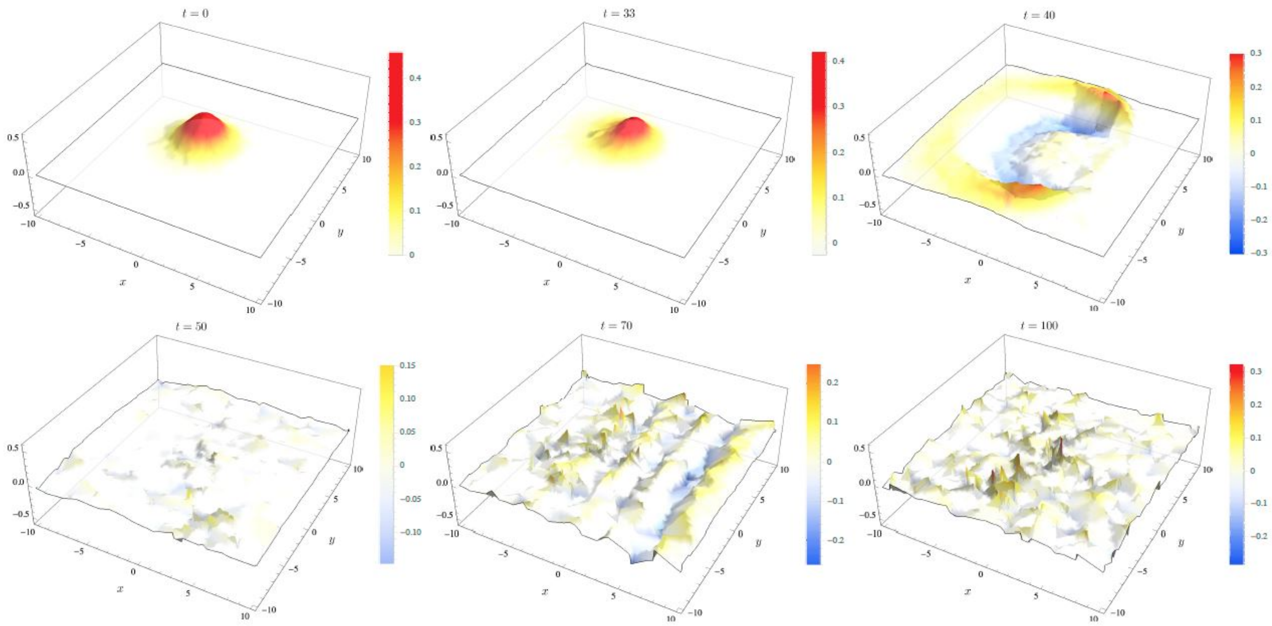


Figure 5.7.: Time evolution of the magnetic field $B$ near the vortex position. At $t = 0$, the initial field configuration corresponds to the vortex configuration–compare to figure 4.9. As the Coulomb layer encounters the vortex, at $t = 33$, the magnetic field starts to dissipate in the core of the layer. As a consequence, electromagnetic radiation is produced. Observe a hemispherical wavefront of such radiation at $t = 40$. At $t = 70$, the $(\nu, 0)$-Domain Wall encounters the wavefront, and most of the of the electromagnetic radiation is reflected.

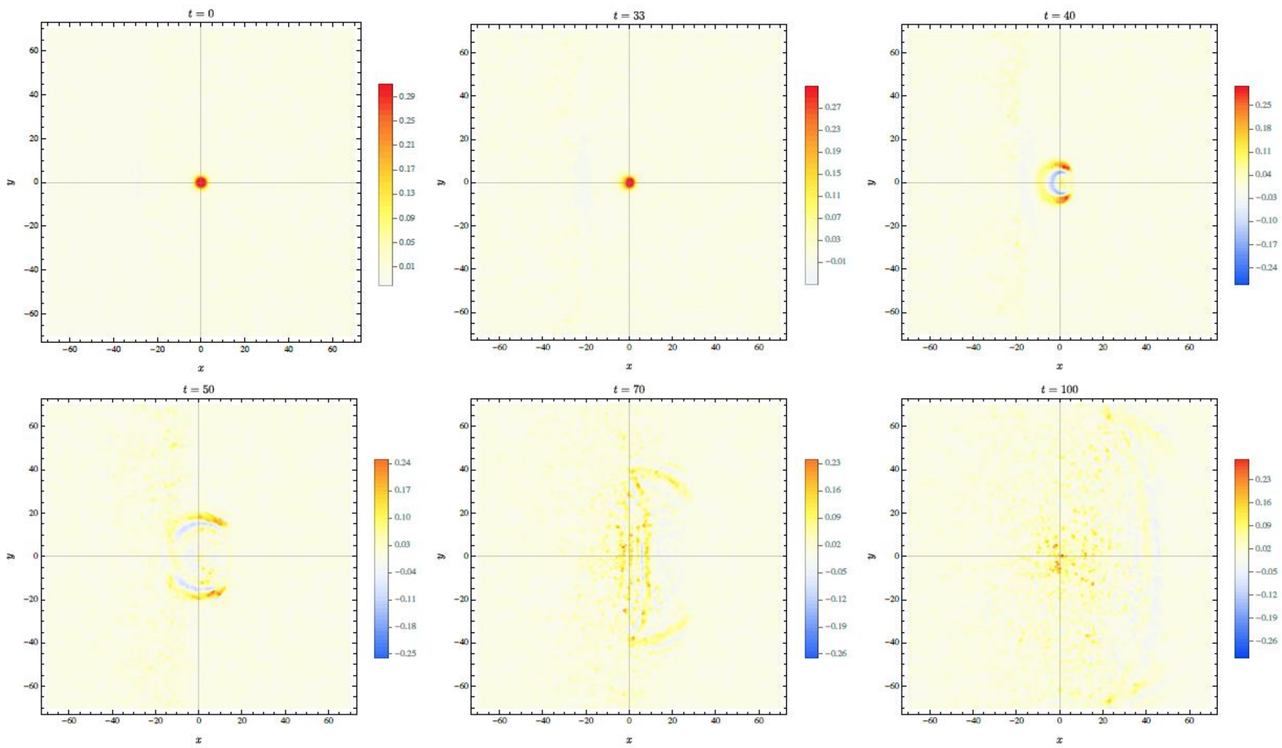


Figure 5.8.: Time evolution of the magnetic field $B$.

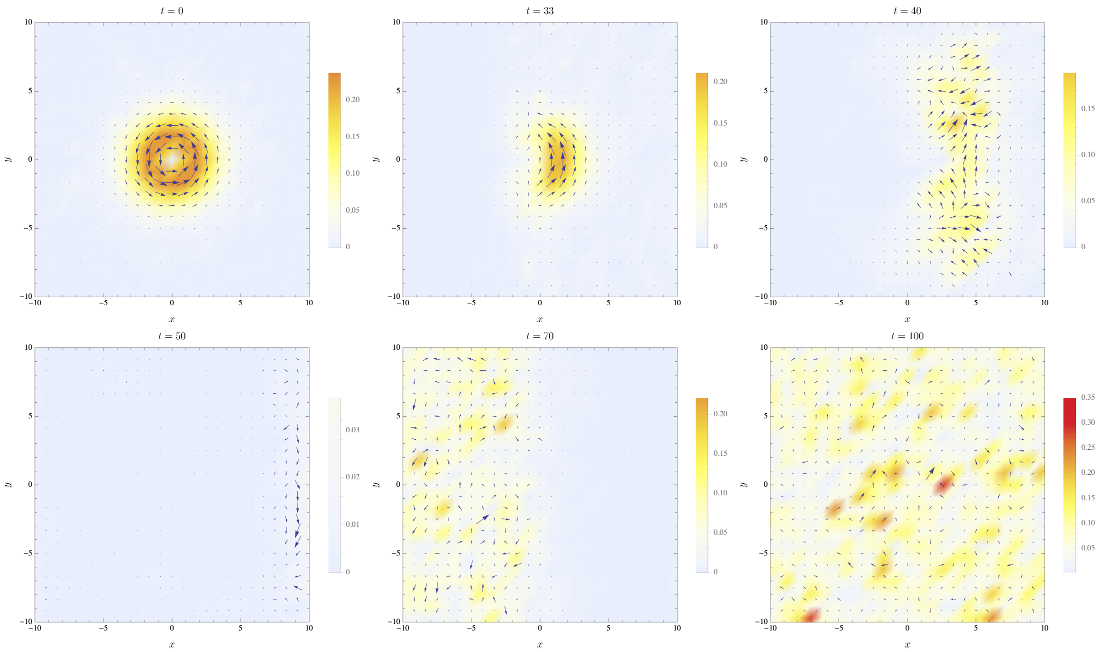


Figure 5.9.: Time evolution of the electric current $j^{\mu}$. The vector at the point $(x, y)$, has components $(j_1, j_2)$, while the background colour represents the norm $|j_i|$

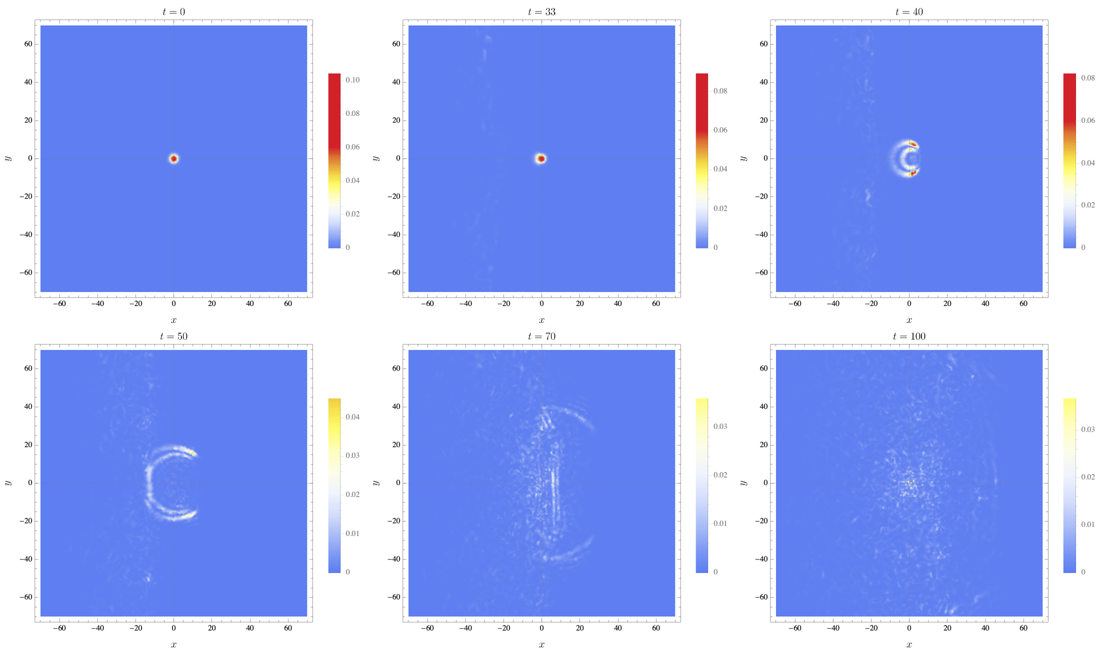


Figure 5.10.: Time evolution of the electromagnetic energy density.

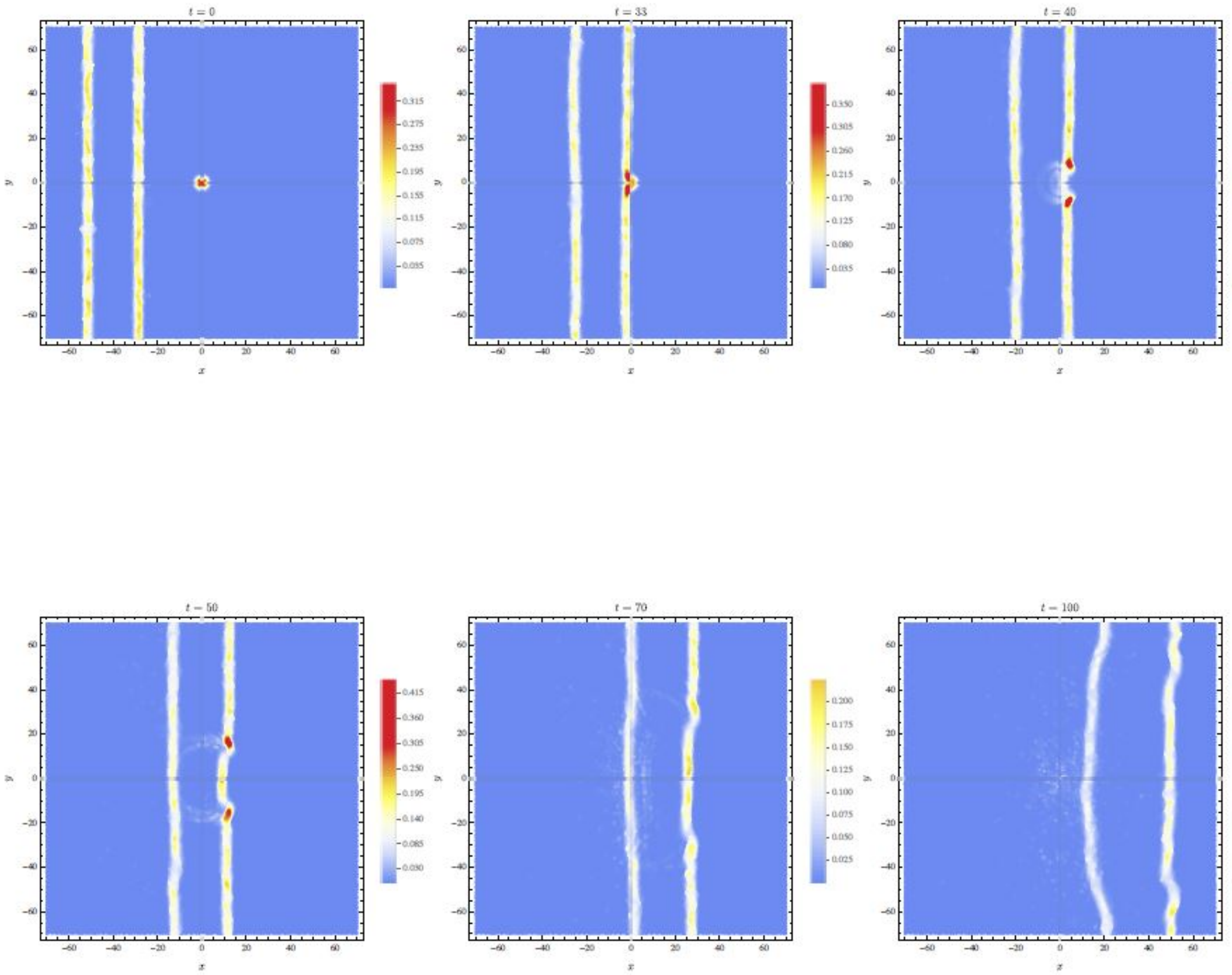


Figure 5.11.: Time evolution of Total energy

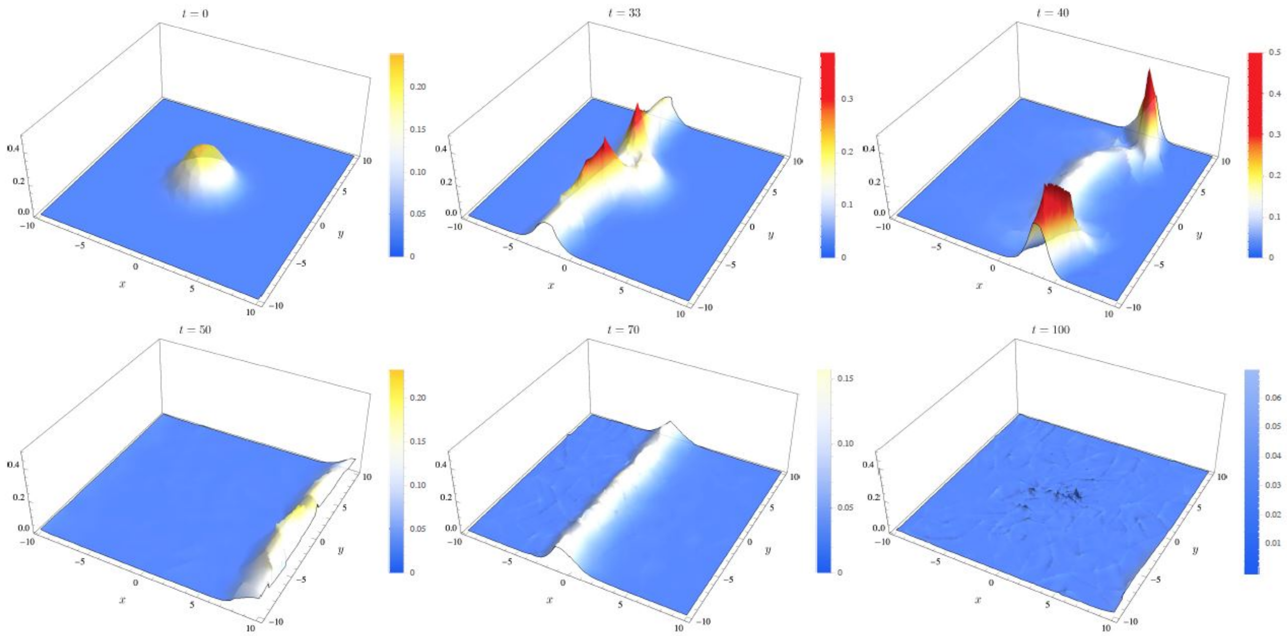


Figure 5.12.: Time evolution of the energy density $\mathcal{E}_\phi$

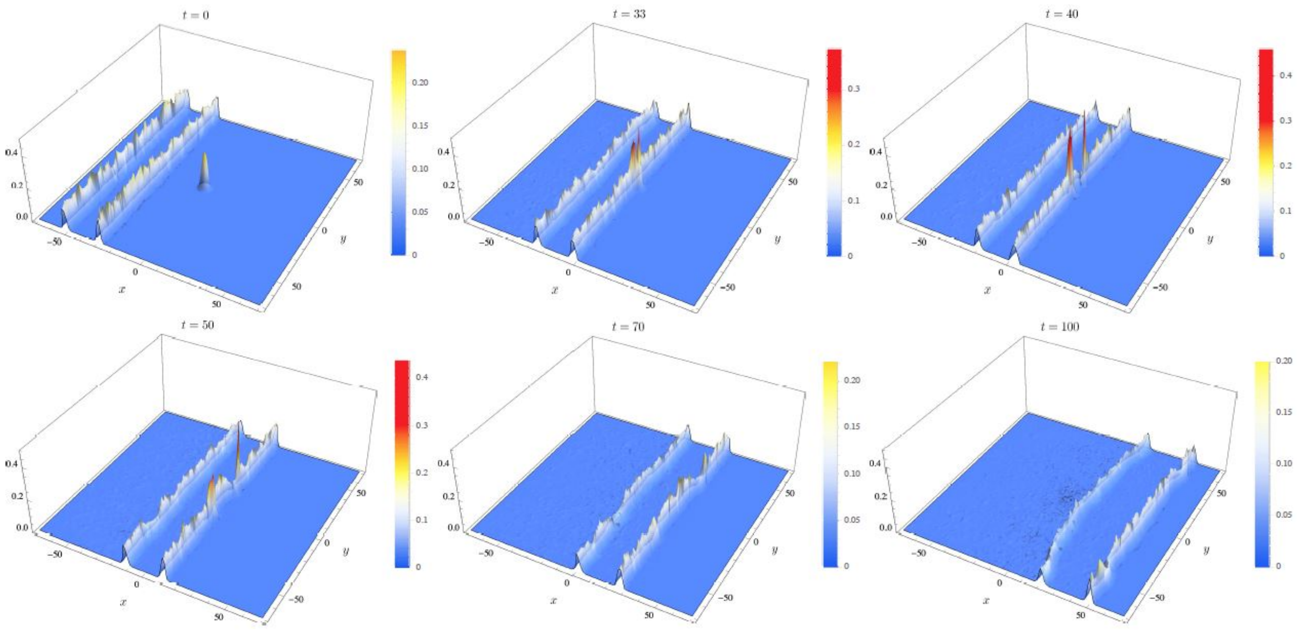


Figure 5.13.: Time evolution of the energy density $\mathcal{E}_\phi$.

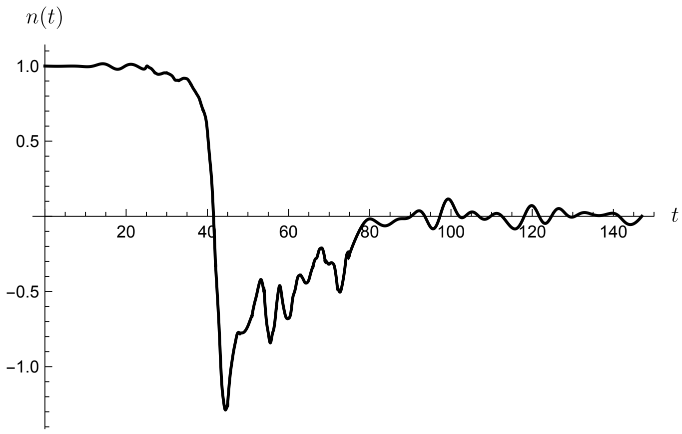


Figure 5.14.: Time evolution of $n(t)$, computed from the flux of the magnetic field $B$.

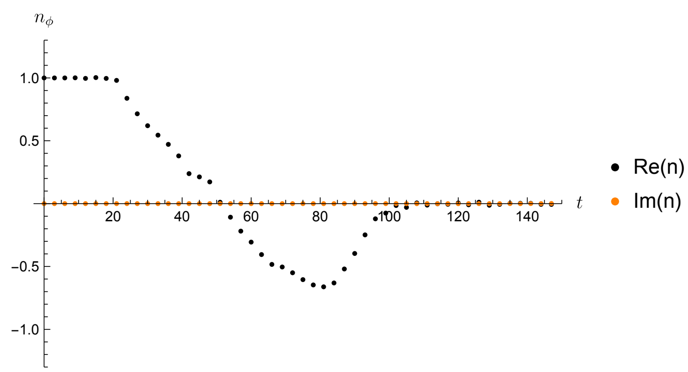


Figure 5.15.: Time evolution of $n_\phi$, computed from the scalar field $\phi$.

# Conclusions and outlook

The erasure of defects mechanism proposed by Dvali-Liu-Vachaspati mechanism is born out, at the classical level, in the $\phi^6$ model. In this model, a Coulomb vacuum layer sweeps away a vortex. The results of our simulation of the interaction between a Coulomb vacuum layer, and a vortex allow us to conclude that the vortex unwinds for all considered regimes of the parameter space. In addition, we have not observed any partial unwinding, or transitions from one topological sector with high winding to a lower one. It suggests the independence of the Dvali-Liu-Vachaspati mechanism from the values of the parameters, and the winding number of the vortex.

The $\phi^6$-model is versatile enough to study the time evolution of the field configuration in the core of a Coulomb Vacuum Layer, and it can be used as a first approximation to more general models in which the interaction of topological defects is relevant. For instance, in GUT that contain discrete symmetries, and the Higgs sector breaks the unified group as well as the discrete group, allows the existence of non-stable Domain Walls, and monopoles. If in the core of such a domain wall the whole symmetry group is restored, then the Coulomb phase is realised. Thus when a monopole is swept by a domain wall, it will unwind, in analogous evolution to the vortex unwinding in a Coulomb vacuum layer in the $\phi^6$-model. We remark here that the gauge fields are expected to be localised in the core of the domain wall, and that the energy of the monopole will dissipate while heating the wall.

Further generalisations, and applications of the $\phi^6$-model include considering higher dimensions. In $(3+1)$ dimensions, The vortex solutions can be extended in the third spatial dimension, and serve as a model for cosmic strings, or vortex lines in super fluids. In the cosmological context, this model can be treated as a numerical experiment to study the interactions of strings with domain walls, allowing the possibility now to have strings ending on walls, or walls being bounded by strings.

Although our results can be trusted for time scales $\mathcal{O}(100m_h^-1)$, further studies are necessaries to study the subsequent evolution of the domain walls after the magnetic charge is dissipated in its core. In addition, if we free the requirement that the Coulomb vacuum layer is metastable–$l \sim \mathcal{O}(40m_h^-1)$–the interaction the vortex needs further study. At the moment of writing this document simulations in this direction are being realized. Further updates can be found in the following link `https://github.com/jusvalbuenabe/TMP-Valbuena`

# A. Vortex Profiles Approximations

The Vortex Profiles 4.5, and 4.6,

$$\phi(r,\theta) = v e^{in\theta} F(r),$$
$$A_i(r,\theta) = -\frac{n}{er}\epsilon_{ij} n_j A(r),$$

are determined by the dimensionless functions $F(r)$, and $A(r)$. In the following sections we discuss different analytical, and numerical approximations to these functions. Moreover, we describe the procedure that we used to get the different approximations.

## A.1. Analytical Approximations for $r \to 0$

For the limit $r \to 0$, $A(r)$ and $F(r)$ can be approximated by polynomials:

$$F(r) = \sum_{i=1}^{N} b_i r^i,$$

$$A(r) = \sum_{i=1}^{N} c_i r^i,$$

where $c_i$, and $b_i$ are constant coefficients for $i = 1, \ldots, N$, and $N$ is sufficiently large– $N > n+2$. Substituting this ansatz in 4.7, and 4.8, and requiring the leading order to be zero, we find that $b_i = 0$ for $i < n+2$, and $j \neq n$, and $c_j = 0$ for $j < n$ and $j \neq 2$ (otherwise the leading order does not vanish). Thus

$$\begin{aligned} F(r) &= b_n r^n + b_{n+2} r^{n+2} + \mathcal{O}(r^{n+3}), \\ A(r) &= c_2 r^2 + c_{2n+2} r^{2n+2} + \mathcal{O}(r^{2n+3}). \end{aligned} \tag{A.1}$$

Replacing A.1 in 4.7, and 4.8 one gets

$$0 = -\frac{1}{4} r^{n+1} \left( (m_h^2 - 8c_2 n^2) b_n - 16(n+1) b_{n+2} \right) + \mathcal{O}(r^{n+3}),$$

$$0 = -r^{2n-1} \left( b_n^2 m_v^2 + 4n(n+1) c_{2n+2} \right) + \mathcal{O}(r^{2n+2}),$$

respectively. Requiring the coefficients of the leading order term to vanish, on e gets the constrains

$$b_{2+n} = \frac{b \left( m_h^2 - 8cn^2 \right)}{16(n+1)}$$

$$c_{2+2n} = -\frac{b^2 m_v^2}{4n(n+1)}$$

Consequently, we obtain the following approximations for $A$ and $F$–for $r \to 0$:

$$\begin{aligned} F(r) &= br^n + \frac{b\left(m_h^2 - 8cn^2\right)}{16(n+1)} r^{n+2}, \\ A(r) &= cr^2 - \frac{b^2 m_v^2}{4n(n+1)} r^{2n+2}, \end{aligned} \tag{A.2}$$

where $b$, and $c$ are independent parameters.

## A.2. Analytical Approximations for $r \to \infty$

To study the asymptotic behaviour of the Vortex profiles as $r \to \infty$, we approximate the solutions to the equations 4.7, and 4.8 by the ansatz 4.12:

$$\begin{aligned} f(r) &= \left(c_{f_0} + \frac{c_{f_1}}{r} + \mathcal{O}\left(\frac{1}{r^2}\right)\right) r^{\alpha_f} e^{-\gamma_f r}, \\ a(r) &= \left(c_{a_0} + \frac{c_{a_1}}{r} + \mathcal{O}\left(\frac{1}{r^2}\right)\right) r^{\alpha_a} e^{-\gamma_a r}, \end{aligned}$$

where $c_{f_0}$, $c_{f_1}$, $c_{a_0}$, and $c_{a_1}$ are non-zero constant coefficients, while the pairs $(\alpha_f, \gamma_f)$, and $(\alpha_a, \gamma_a)$ determine how fast the functions $f$ and $a$ approach 0, respectively. Replacing the ansatz in equation 4.8 we obtain

$$\begin{aligned} 0 = {} & r^{\alpha_a} e^{-\gamma_a r}\left(c_{a_0}\left(\gamma_a^2 - m_v^2\right) + \frac{c_{a_0}\gamma_a\left(1 - 2\alpha_a\right) + c_{a_1}\left(\gamma_a^2 - m_v^2\right)}{r}\right) \\ & + r^{\alpha_a + \alpha_f} e^{-(\gamma_a + \gamma_f)r}\left(2m_v^2 c_{a_0} c_{f_0} + 2m_v^2 \frac{c_{a_1} c_{f_0} + c_{a_0} c_{f_1}}{r}\right) \\ & + r^{\alpha_a + 2\alpha_f} e^{-\left(\gamma_a + 2\gamma_f\right)r}\left(-m_v^2 c_{a_0} c_{f_0}^2 + m_v^2 \frac{-c_{a_1} c_{f_0}^2 - 2c_{a_0} c_{f_1} c_{f_0}}{r}\right) \\ & + r^{\alpha_a} e^{-\gamma_a r}\left(1 + r^{\alpha_f} e^{-\gamma_f r} + r^{2\alpha_f} e^{-2\gamma_f r}\right) \mathcal{O}\left(\frac{1}{r^2}\right). \end{aligned} \tag{A.3}$$

The first term of the rhs of A.3 is its leading order term. Then, requiring that the coefficients of $r^{\alpha_a} e^{-\gamma_a r}$ and $r^{\alpha_a - 1} e^{-\gamma_a r}$ to be zero, we can conclude that: $\gamma_a = m_v$ and $\alpha_a = \frac{1}{2}$.

On the other hand, replacing the ansatz in equation 4.7 we obtain

$$
\begin{aligned}
0 = \; & r^{2\alpha_a} e^{-2\gamma_a r} \left( \frac{n^2 c_{a_0}^2}{r^2} + \frac{2n^2 c_{a_0} c_{a_1}}{r^3} \right) \\
& + r^{\alpha_f} e^{-\gamma_f r} \Bigg( c_{f_0} \left( \gamma_f^2 - m_h^2 \right) + \frac{c_{f_1} \left( \gamma_f^2 - m_h^2 \right) - c_{f_0} \left( 2\alpha_f + 1 \right) \gamma_f}{r} \\
& \qquad\qquad + \frac{c_{f_0} \alpha_f^2 + c_{f_1} \left( 1 - 2\alpha_f \right) \gamma_f}{r^2} + \frac{c_{f_1} \left( \alpha_f - 1 \right)^2}{r^3} \Bigg) \\
& + r^{2\alpha_f} e^{-2\gamma_f r} \left( \frac{9}{2} m_h^2 c_{f_0}^2 + \frac{9 m_h^2 c_{f_0} c_{f_1}}{r} + \frac{9 m_h^2 c_{f_1}^2}{2r^2} \right) \\
& + r^{2\alpha_a + \alpha_f} e^{-\left(2\gamma_a + \gamma_f\right) r} \left( - \frac{n^2 c_{a_0}^2 c_{f_0}}{r^2} - \frac{n^2 c_{a_0} \left( 2 c_{a_1} c_{f_0} + c_{a_0} c_{f_1} \right)}{r^3} \right) \\
& + \left( 1 + r^{\alpha_f} e^{-\gamma_f r} \right) \left( r^{2\alpha_a} e^{-2\gamma_a r} + r^{\alpha_f} e^{-\gamma_f r} \right) \mathcal{O} \left( \frac{1}{r^4} \right) \\
& + \mathcal{O} \left( r^{3\alpha_f} e^{-3\gamma_f r} \right) .
\end{aligned}
\tag{A.4}
$$

If $m_h < 2m_v$, the leading term of the rhs of A.4 is the second term. Requiring the coefficients of $r^{\alpha_f} e^{-\gamma_f r}$, and $r^{\alpha_f - 1} e^{-\gamma_f r}$ to be zero, we obtain $\gamma_f = m_h$ and $\alpha_f = -\frac{1}{2}$, as it was stated in 4.9.

If when $m_h > 2m_v$, the leading term of the rhs of A.4 is now the first term. In this case we might required the coefficients of $r^{2\alpha_a - 2} e^{-2\gamma_a r} = r^{-1} e^{-2m_v r}$ and $r^{2\alpha_a - 3} e^{-2\gamma_a r} = r^{-2} e^{-2m_v r}$ to be zero. Since $c_{a_0} \neq 0$, the second term of A.4 must be such that it compensates the first one. In other words, $\alpha_f = 2\alpha_a - 2 = -1$ and $\gamma_f = 2\gamma_a = 2m_v$. With this result, the leading order of the rhs of A.4 is

$$
e^{-\gamma_f r} \left( \frac{\delta_1}{r} + \frac{\delta_2}{r^2} \right).
$$

where

$$
\begin{aligned}
\delta_1 &= n^2 c_{a_0}^2 - \left( m_h^2 - 4m_v^2 \right) c_{f_0}, \\
\delta_2 &= 2n^2 c_{a_0} c_{a_1} + 2m_v c_{f_0} - \left( m_h^2 - 4m_v^2 \right) c_{f_1}.
\end{aligned}
$$

Requiring $\delta_1$, and $\delta_2$ to vanish, one gets that $c_{f_0}$, and $c_{f_1}$ depend on $c_{a_0}$, and $c_{a_1}$ as follows:

$$
\begin{aligned}
c_{f_0} &= \frac{c_{a_0}^2 n^2}{m_h^2 - 4m_v^2}, \\
c_{f_1} &= \frac{2 c_{a_0} (c_{a_0} m_v + c_{a_1} (m_h^2 - 4m_v^2)) n^2}{(m_h^2 - 4m_v^2)^2}.
\end{aligned}
$$

To summarize this section, we have found the following two regimes, in which the functions $A$ and $F$ can be asymptotycally pproximated in terms of two parameter family of solutions:

- Regime $m_h \leq 2m_v$

$$
\begin{aligned}
A(r) &= 1 - c_{a_0}\sqrt{r}e^{-m_v r}, \\
F(r) &= 1 - c_{f_0}\frac{e^{-m_h r}}{\sqrt{r}},
\end{aligned}
\tag{A.5}
$$

where $c_{a_0}$ and $c_{f_0}$ are the independent parameters. The core of the vortex has two characteristic lengths: $m_h^{-1}$ which corresponds to the size of the scalar vortex, and $m_v^{-1}$ which corresponds to the size of the vector vortex.

- Regime $m_h > 2m_v$

$$
\begin{aligned}
A(r) &= 1 - \left(c_{a_0}\sqrt{r}e^{-m_v r} + c_{a_1}\frac{e^{-m_v r}}{\sqrt{r}}\right), \\
F(r) &= 1 - \left(c_{f_0}\frac{e^{-2m_v r}}{r} + c_{f_1}\frac{e^{-2m_v r}}{r^2}\right),
\end{aligned}
\tag{A.6}
$$

where

$$
\begin{aligned}
c_{f_0} &= \frac{c_{a_0}^2 n^2}{m_h^2 - 4m_v^2}, \\
c_{f_1} &= \frac{2c_{a_0}(c_{a_0}m_v + c_{a_1}(m_h^2 - 4m_v^2))n^2}{(m_h^2 - 4m_v^2)^2},
\end{aligned}
$$

In this regime, $c_{a_0}$, and $c_{a_1}$ are the independent parameters. We highlight that the characteristic lengths of the scalar, and the vector profiles of the vortex are $(2m_v)^{-1}$ and $m_v^{-1}$ respectively. Thus, their size are not independent from each other.

## A.3. Numerical Approximations

For intermediate values of $r$, explicit solutions to the equations 4.7 and 4.8 are not known, but approximate solutions can be obtained numerically. We have found these solutions for different parameters of the theory, using the shooting method that we describe below.

In our method, we use the the initial conditions 4.15 at $r = r_1 \sim \mathcal{O}(10^{-3}m_h^{-1})$, to numerically integrate the equations 4.7, and 4.8. The numerical values of the initial conditions 4.15 at $r = r_1$ are determined by the values of the independent parameters $(b, c)$. The numerical integration is done by the software Mathematica. Typically, the Wolfram Language goes to considerable effort to pick the best integration method automatically, and it chosses between several different methods known for doing particular types of numerical integrations[40].

Subsequently, the parameters $b$, and $c$ are varied until the numerical solutions approach 1 asymptotically. However–for $r \sim \mathcal{O}(10m_h^{-1})$–the solutions that are found contain instabilities that produce divergent solutions. One example of such solutions is shown in figure A.1.

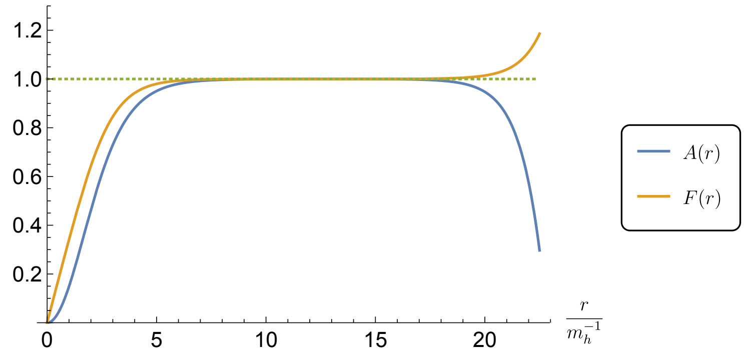


Figure A.1.: An example of numerical solutions to the equations 4.7, and 4.8, for $m_h = 1$,$m_v = 1$ and $n = 1$. The solutions are found by the numerical integration of the initial conditions 4.15, where $b = 0.346$, $c = 0.163$, and $r_1 = 10^{-3} m_h^{-1}$. For $5 < r/m_h^{-1} < 10$, the solutions approach 1 asymptotically. However, for $r > 10$, the solutions are divergent.

It is then necessary to do a second approximation to the solutions for $r \to \infty$. We use the asymptotic behaviour of $A(r)$, and $F(r)$, and the fact that both functions are monotonically increasing. We firstly determine a second radius $r_2 \sim \mathcal{O}(10 m_h^{-1})$ for which

$$\min(A(r_2), F(r_2)) = 1 - \mathcal{O}(10^{-3}),$$
$$A'(r_2) > 0, \text{ and } F'(r_2) > 0.$$

Then, for $r > r_2$, the solutions are approximated by the ansatz 4.13, or 4.14, depending on the regime of the masses. The corresponding independent parameters–$(c_{a_0}, c_{f_0})$, or $(c_{a_0}, c_{a_1})$–are found by imposing continuity of $A$, and $A'$ at a radius $r_A \gtrsim r_2$, and continuity of $F$, and $F'$ at a different radius $r_F \gtrsim r_2$. This four conditions determine $(c_{a_0}, c_{f_0}, r_A, r_F)$–for $m_h \leq 2m_v$–or $(c_{a_0}, c_{a_1}, r_A, r_F)$–for $m_h = 2m_v$.

Continuing with the example shown in the figure A.1, we present the analytical approximations to the vortex profiles for $r \to 0$ in the figure A.2, and for $r \to \infty$ in the figure A.3

Proceeding as it was described before we have found the Vortex profile for different parameters of the theory, $(m_v, m_h, n)$. In what follows we have set $v = 1$ unless stated otherwise. We present some of the vortex profiles that were found for the different regimes.

### A.3.1. Regime $m_h \leq 2m_v$:

The figures 4.2 and 4.3 shows the vortex profiles obtained numerically for the cases $m_h = m_v = 1$, and $m_h = 1$ and $m_v = 10$, respectively. The colors correspond to different winding numbers $n$. The asymptotic approximations and the corresponding numerical coefficients are presented in the tables A.1 and A.2, which can be found in the appendix.

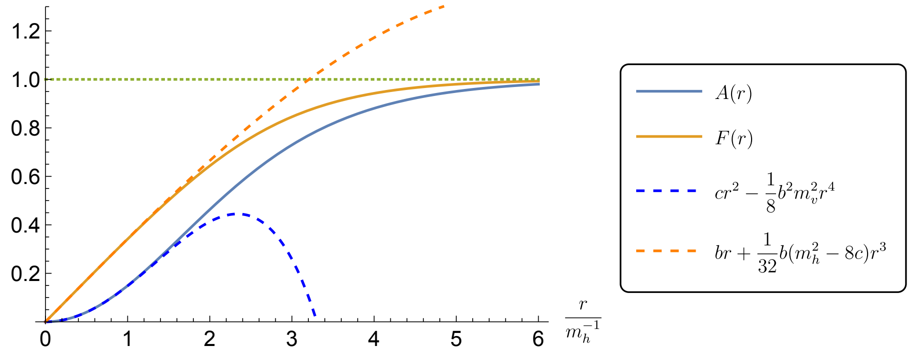


Figure A.2.: Analytical approximations–given by equation 4.15–to the vortex profiles for $r \to 0$. In this example $m_h = 1$, $m_v = 1$ and $n = 1$. We found that the independent parameters are $b = 0.346$ and $c = 0.162$.

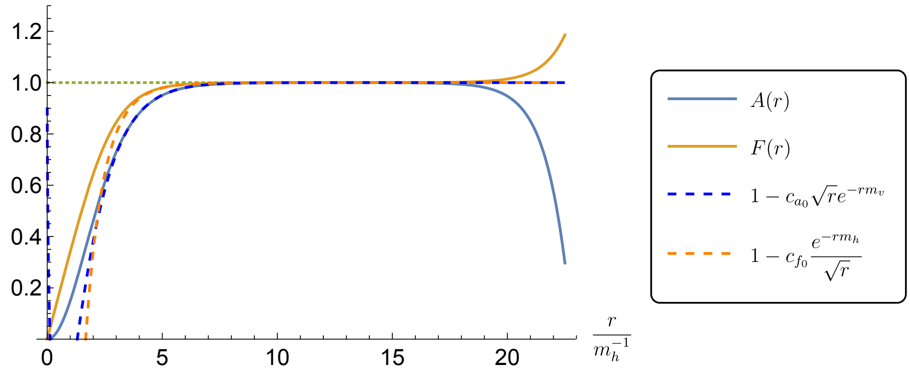


Figure A.3.: Analytical approximations–given by equation 4.13–to the Vortex profiles for $r \to \infty$. In this example $m_h = 1$, $m_v = 1$ and $n = 1$. We found that the independent parameters are $c_{a_0} = 3.23$ and $c_{f_0} = 6.86$.

### A.3.2. Regime $m_h > 2m_v$

The figure 4.4 shows the vortex profiles obtained numerically for $m_h = 1$ and $m_v = 0.1$ for $n = 1, 2, 3, 4$. The asymptotic behaviour and the corresponding numerical coefficients are presented in the table A.3, which can be found in the appendix.

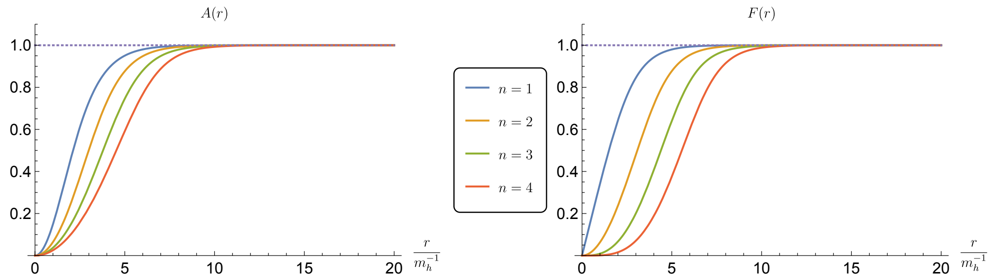


Figure A.4.: Vortex Profile for $m_h = m_v = 1$. Here the dependence of the core size on $n$ can be observed. Note however how the asymptotic behavour of $A(r)$ and $F(r)$ does not depend on $n$ as it is expected if we refer to the equation 4.13

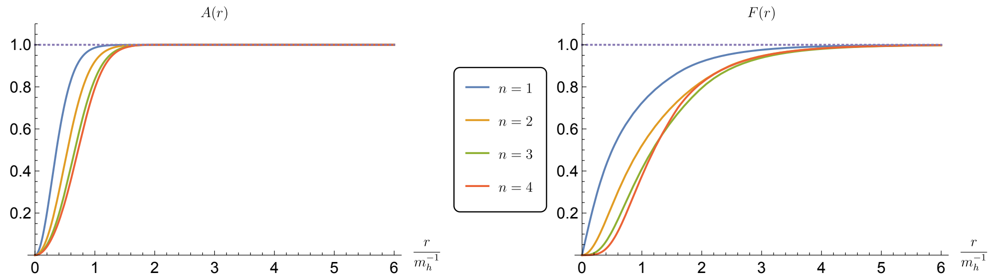


Figure A.5.: Vortex Profiles for $m_h = 1$ and $m_v = 10$ for different winding number $n$

## A.4. Figures

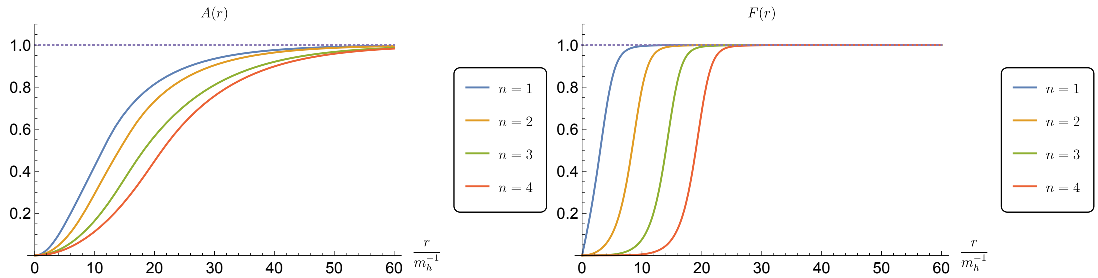


Figure A.6.: Vortex Profiles for $m_h = 1$ and $m_v = 0.1$. Comparing this profiles to the profiles shown in figure 4.2 the gauge core increases, as it expected, 10 times. On the other hand, note that the scalar core size is bigger than the one found in the previous regime increases with $n$

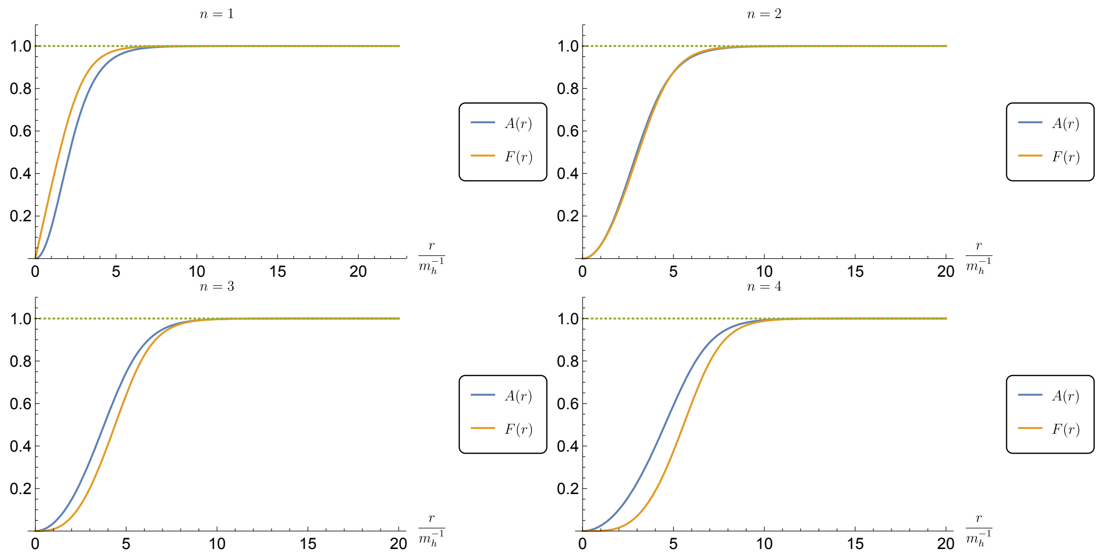


Figure A.7.: Vortex Profiles for $m_h = m_v$.Here the shape of the core for $A(r)$ and $F(r)$ for a given $n$ can be compared. Note that the scalar vortex core is smaller than gauge vortex core for $n = 1$ while they are practically the same size for $n = 2$. For $n \geq 3$ it is found that the scalar core slightly bigger.

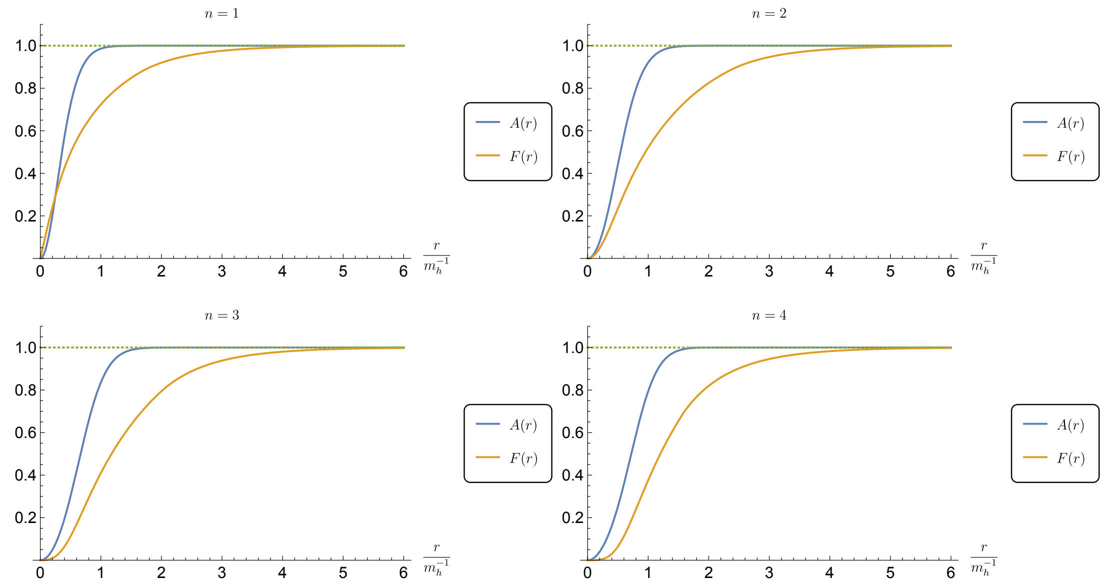


Figure A.8.: Vortex Profiles for $m_h = 1.0$ $m_v = 10.0$..

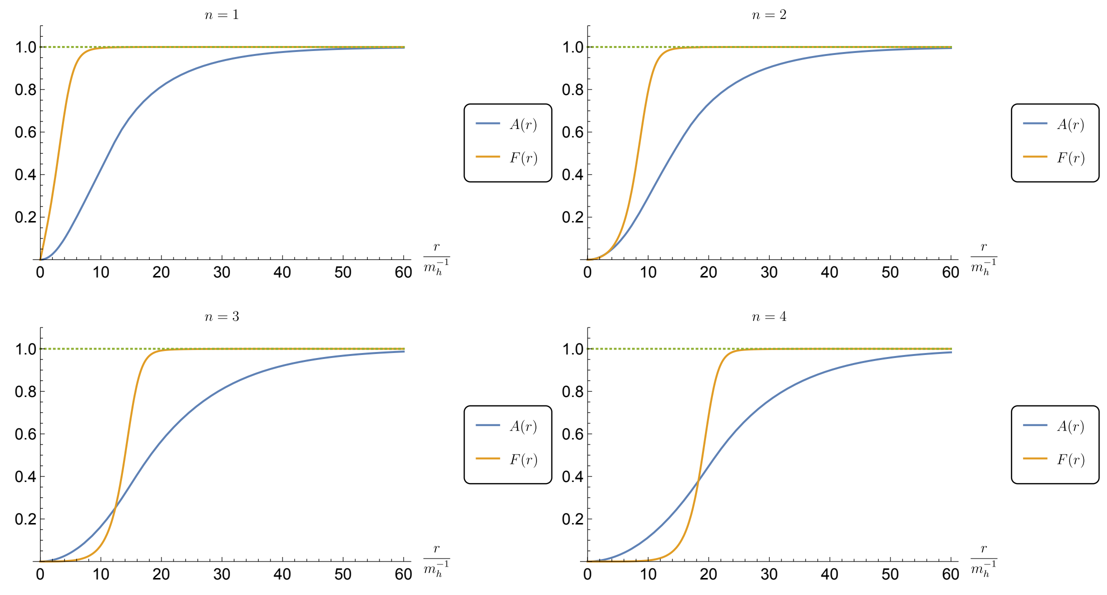


Figure A.9.: Vortex Profiles for $m_h = 1.0$ and $m_v = 0.1$.

| | Analytical approximation for $r < 10^{-3}$ | b | c | Analytical approximation for $r > 10$ | $c_{a_0}$ | $c_{f_0}$ |
|---|---|---|---|---|---|---|
| $n = 1$ | $A(r) = cr^2 - \frac{1}{8}b^2 m_v^2 r^4$<br>$F(r) = br + \frac{1}{32}b\left(m_h^2 - 8c\right)r^3$ | $3.46 \times 10^{-1}$ | $1.63 \times 10^{-1}$ | $A(r) = 1 - c_{a_0}\sqrt{r}e^{-m_v r}$<br>$F(r) = 1 - c_{f_0}\frac{e^{-m_h r}}{\sqrt{r}}$ | 3.23 | 6.86 |
| $n = 2$ | $A(r) = cr^2 - \frac{1}{24}b^2 m_v^2 r^6$<br>$F(r) = br^2 + \frac{1}{48}b\left(m_h^2 - 32c\right)r^4$ | $6.45 \times 10^{-2}$ | $6.44 \times 10^{-1}$ | | 8.60 | 49.7 |
| $n = 3$ | $A(r) = cr^2 - \frac{1}{48}b^2 m_v^2 r^8$<br>$F(r) = br^3 + \frac{1}{64}b\left(m_h^2 - 72c\right)r^5$ | $8.93 \times 10^{-3}$ | $3.73 \times 10^{-2}$ | | 21.9 | $2.23 \times 10^{2}$ |
| $n = 4$ | $A(r) = cr^2 - \frac{1}{80}b^2 m_v^2 r^{10}$<br>$F(r) = br^4 + \frac{1}{80}b\left(m_h^2 - 128c\right)r^6$ | $1.02 \times 10^{-3}$ | $2.53 \times 10^{-2}$ | | 52.9 | $8.15 \times 10^{-2}$ |

Table A.1.: Analytic approximations for the vortex profiles for the case $m_h = m_v = 1.0$

| | Analytical approximation for $r < 10^{-3}$ | $b$ | $c$ | Analytical approximation for $r > r_2$ | $r_2$ | $c_{a_0}$ | $c_{a_1}$ |
|---|---|---|---|---|---|---|---|
| $n = 1$ | $A(r) = cr^2 - \frac{1}{8}b^2 m_v^2 r^4$<br>$F(r) = br + \frac{1}{32}b\left(m_h^2 - 8c\right)r^3$ | 1.27 | 5.78 | $A(r) = 1 - c_{a_0}\sqrt{r}e^{-m_v r}$<br>$F(r) = 1 - c_{f_0}\frac{e^{-m_h r}}{\sqrt{r}}$ | 1.5 | $1.89 \times 10^{3}$ | $8.34 \times 10^{-1}$ |
| $n = 2$ | $A(r) = cr^2 - \frac{1}{24}b^2 m_v^2 r^6$<br>$F(r) = br^2 + \frac{1}{48}b\left(m_h^2 - 32c\right)r^4$ | 1.27 | 2.01 | | 2.5 | $5.49 \times 10^{4}$ | 1.85 |
| $n = 3$ | $A(r) = cr^2 - \frac{1}{48}b^2 m_v^2 r^8$<br>$F(r) = br^3 + \frac{1}{64}b\left(m_h^2 - 72c\right)r^5$ | 1.2 | 1.23 | | 2.0 | $1.11 \times 10^{5}$ | 2.14 |
| $n = 4$ | $A(r) = cr^2 - \frac{1}{80}b^2 m_v^2 r^{10}$<br>$F(r) = br^4 + \frac{1}{80}b\left(m_h^2 - 128c\right)r^6$ | 1.2 | 1.01 | | 1.6 | $5.13 \times 10^{4}$ | 1.88 |

Table A.2.: Analytic approximations for the vortex profile for the case where $m_h = 1.0$, $m_v = 10.0$

| | Analytical approximation for $r < 10^{-3}$ | $b$ | $c$ | Analytical approximation for $r > r_F$ and $r > r_A$, respectively | $r_A$ | $r_F$ | $c_{a_0}$ | $c_{a_1}$ |
|---|---|---|---|---|---|---|---|---|
| $n = 1$ | $A(r) = cr^2 - \frac{1}{8}b^2 m_v^2 r^4$<br>$F(r) = br + \frac{1}{32}b\left(m_h^2 - 8c\right)r^3$ | $1.36 \times 10^{-1}$ | $6.65 \times 10^{-3}$ | $A(r) = 1 - \left(c_{a_0}\sqrt{r}e^{-m_v r} + c_{a_1}\frac{e^{-m_v r}}{\sqrt{r}}\right)$ | 12.0 | 17.4 | $1.01 \times 10^{-1}$ | 4.09 |
| $n = 2$ | $A(r) = cr^2 - \frac{1}{24}b^2 m_v^2 r^6$<br>$F(r) = br^2 + \frac{1}{48}b\left(m_h^2 - 32c\right)r^4$ | $2.60 \times 10^{-3}$ | $3.06 \times 10^{-3}$ | | 16.0 | 18.6 | $1.71 \times 10^{-1}$ | 5.40 |
| $n = 3$ | $A(r) = cr^2 - \frac{1}{48}b^2 m_v^2 r^8$<br>$F(r) = br^3 + \frac{1}{64}b\left(m_h^2 - 72c\right)r^5$ | $9.36 \times 10^{-6}$ | $1.65 \times 10^{-3}$ | $F(r) = 1 - \left(\left(\frac{c_{a_0}^2 n^2}{m_h^2 - 4m_v^2}\right)\frac{e^{-2m_v r}}{r} + \left(\frac{2c_{a_0}\left(c_{a_0} m_v + c_{a_1}\left(m_h^2 - 4m_v^2\right)\right)n^2}{\left(m_h^2 - 4m_v^2\right)^2}\right)\frac{e^{-2m_v r}}{r^2}\right)$ | 20.0 | 28.2 | $6.56 \times 10^{-1}$ | 1.20 |
| $n = 4$ | $A(r) = cr^2 - \frac{1}{80}b^2 m_v^2 r^{10}$<br>$F(r) = br^4 + \frac{1}{80}b\left(m_h^2 - 128c\right)r^6$ | $1.09 \times 10^{-7}$ | $1.15 \times 10^{-2}$ | | 25.0 | 31.2 | $8.3 \times 10^{-1}$ | 1.59 |

Table A.3.: Analytic approximations for the vortex profile for the case where $m_h = 1.0$ and $m_v = 0.1$

# Bibliography


[1] B. Acharya, J. Alexandre, S. Baines, P. Benes, B. Bergmann, J. Bernabéu, A. Bevan, H. Branzas, M. Campbell, S. Cecchini, and et al. "Magnetic Monopole Search with the Full MoEDAL Trapping Detector in 13TeV pp Collisions Interpreted in Photon-Fusion and Drell-Yan Production". In: *Physical Review Letters* 123.2 (July 2019). ISSN: 1079-7114. DOI: 10.1103/physrevlett.123.021802. URL: http://dx.doi.org/10.1103/PhysRevLett.123.021802.

[2] A. Lazanu, C. Martins, and E. Shellard. "Contribution of domain wall networks to the CMB power spectrum". In: *Physics Letters B* 747 (July 2015), pp. 426–432. ISSN: 0370-2693. DOI: 10.1016/j.physletb.2015.06.034. URL: http://dx.doi.org/10.1016/j.physletb.2015.06.034.

[3] V. A. Rubakov. *Classical theory of gauge fields*. 2002.

[4] A. Vilenkin and E. P. S. Shellard. *Cosmic Strings and Other Topological Defects*. Cambridge University Press, 2000. ISBN: 9780521654760. URL: http://www.cambridge.org/mw/academic/subjects/physics/theoretical-physics-and-mathematical-physics/cosmic-strings-and-other-topological-defects?format=PB.

[5] T. P. Cheng and L. F. Li. *GAUGE THEORY OF ELEMENTARY PARTICLE PHYSICS*. 1984. ISBN: 9780198519614.

[6] V. Mukhanov. *Physical Foundations of Cosmology*. Oxford: Cambridge University Press, 2005. ISBN: 0521563984. URL: http://www-spires.fnal.gov/spires/find/books/www?cl=QB981.M89::2005.

[7] S. Weinberg. "Gauge and global symmetries at high temperature". In: *Phys. Rev. D* 9 (12 June 1974), pp. 3357–3378. DOI: 10.1103/PhysRevD.9.3357. URL: https://link.aps.org/doi/10.1103/PhysRevD.9.3357.

[8] J. Zinn-Justin. "Quantum field theory at finite temperature: An Introduction". In: (2000). arXiv: hep-ph/0005272 [hep-ph]. URL: https://arxiv.org/abs/hep-ph/0005272v1.

[9] S. Coleman and E. Weinberg. "Radiative Corrections as the Origin of Spontaneous Symmetry Breaking". In: *Phys. Rev. D* 7 (6 Mar. 1973), pp. 1888–1910. DOI: 10.1103/PhysRevD.7.1888. URL: https://link.aps.org/doi/10.1103/PhysRevD.7.1888.

[10] M. Shifman. *Advanced topics in quantum field theory.* Cambridge, UK: Cambridge Univ. Press, 2012. ISBN: 9781139210362. URL: http://www.cambridge.org/mw/academic/subjects/physics/theoretical-physics-and-mathematical-physics/advanced-topics-quantum-field-theory-lecture-course?format=AR.

[11] T. W. B. Kibble. "Topology of cosmic domains and strings". In: *Journal of Physics A: Mathematical and General* 9.8 (Aug. 1976), pp. 1387–1398. DOI: 10.1088/0305-4470/9/8/029. URL: https://doi.org/10.1088%2F0305-4470%2F9%2F8%2F029.

[12] E. J. Weinberg. *Classical solutions in quantum field theory*. Cambridge Monographs on Mathematical Physics. Cambridge University Press, 2012. ISBN: 9780521114639. DOI: 10.1017/CBO9781139017787. URL: http://www.cambridge.org/us/knowledge/isbn/item6813336/.

[13] Ya. B. Zeldovich, I. Yu. Kobzarev, and L. B. Okun. "Cosmological Consequences of the Spontaneous Breakdown of Discrete Symmetry". In: *Zh. Eksp. Teor. Fiz.* 67 (1974). [Sov. Phys. JETP40,1(1974)], pp. 3–11.

[14] G. H. Derrick. "Comments on nonlinear wave equations as models for elementary particles". In: *J. Math. Phys.* 5 (1964), pp. 1252–1254. DOI: 10.1063/1.1704233.

[15] A. Kudryavtsev, B. M. A. G. Piette, and W. J. Zakrzewski. "Skyrmions and domain walls in (2+1) dimensions". In: *Nonlinearity* 11.4 (July 1998), pp. 783–795. DOI: 10.1088/0951-7715/11/4/002. URL: https://doi.org/10.1088%2F0951-7715%2F11%2F4%2F002.

[16] G. Alestas and L. Perivolaropoulos. "Evading Derrick's theorem in curved space: Static metastable spherical domain wall". In: (2019). DOI: 10.1103/PhysRevD.99.064026. eprint: arXiv:1901.06659.

[17] W. Press, B. Ryden, and D. Spergel. "Dynamical evolution of domain walls in an expanding universe". In: *apj* 347 (Dec. 1989), pp. 590–604. DOI: 10.1086/168151.

[18] H. Nielsen and P. Olesen. "Vortex-line models for dual strings". In: *Nuclear Physics B* 61 (1973), pp. 45–61. ISSN: 0550-3213. DOI: https://doi.org/10.1016/0550-3213(73)90350-7. URL: http://www.sciencedirect.com/science/article/pii/0550321373903507.

[19] Y. Zeldovich and M. Khlopov. "On the concentration of relic magnetic monopoles in the universe". In: *Physics Letters B* 79.3 (1978), pp. 239–241. ISSN: 0370-2693. DOI: https://doi.org/10.1016/0370-2693(78)90232-0. URL: http://www.sciencedirect.com/science/article/pii/0370269378902320.

[20] J. Preskill. "Cosmological Production of Superheavy Magnetic Monopoles". In: *Phys. Rev. Lett.* 43 (1979), p. 1365. DOI: 10.1103/PhysRevLett.43.1365.

[21] A. H. Guth. "The Inflationary Universe: A Possible Solution to the Horizon and Flatness Problems". In: *Phys. Rev.* D23 (1981). [Adv. Ser. Astrophys. Cosmol.3,139(1987)], pp. 347–356. DOI: 10.1103/PhysRevD.23.347.

[22] M. T. et al. (Particle Data Group). "Review of Particle Physics". In: *Phys. Rev. D* 98 (3 Aug. 2018), p. 030001. DOI: 10.1103/PhysRevD.98.030001. URL: https://link.aps.org/doi/10.1103/PhysRevD.98.030001.

[23] P. Langacker and S.-Y. Pi. "Magnetic Monopoles in Grand Unified Theories". In: *Phys. Rev. Lett.* 45 (1980), p. 1. DOI: 10.1103/PhysRevLett.45.1.

[24] G. R. Dvali, A. Melfo, and G. Senjanovic. "Is There a monopole problem?" In: *Phys. Rev. Lett.* 75 (1995), pp. 4559–4562. DOI: 10.1103/PhysRevLett.75.4559. arXiv: hep-ph/9507230 [hep-ph].

[25] G. Dvali, H. Liu, and T. Vachaspati. "Sweeping Away the Monopole Problem". In: *Phys. Rev. Lett.* 80 (11 Mar. 1998), pp. 2281–2284. DOI: 10.1103/PhysRevLett.80.2281. URL: https://link.aps.org/doi/10.1103/PhysRevLett.80.2281.

[26] J. Preskill, S. P. Trivedi, F. Wilczek, and M. B. Wise. "Cosmology and broken discrete symmetry". In: *Nuclear Physics B* 363.1 (1991), pp. 207–220. ISSN: 0550-3213. DOI: https://doi.org/10.1016/0550-3213(91)90241-O. URL: http://www.sciencedirect.com/science/article/pii/055032139190241O.

[27] L. Pogosian and T. Vachaspati. "Interaction of magnetic monopoles and domain walls". In: *Phys. Rev.* D62 (2000), p. 105005. DOI: 10.1103/PhysRevD.62.105005. arXiv: hep-ph/9909543 [hep-ph].

[28] L. Pogosian and T. Vachaspati. "Domain walls in SU(5)". In: *Phys. Rev. D* 62 (12 Nov. 2000), p. 123506. DOI: 10.1103/PhysRevD.62.123506. URL: https://link.aps.org/doi/10.1103/PhysRevD.62.123506.

[29] M. Brush, L. Pogosian, and T. Vachaspati. "Magnetic monopole—domain wall collisions". In: *Phys. Rev.* D92.4 (2015), p. 045008. DOI: 10.1103/PhysRevD.92.045008. arXiv: 1505.08170 [hep-th].

[30] S. Alexander, R. Brandenberger, R. Easther, and A. Sornborger. *On the Interaction of Monopoles and Domain Walls*. 1999. arXiv: hep-ph/9903254 [hep-ph].

[31] A. E. Kudryavtsev, B. M. A. G. Piette, and W. J. Zakrzewski. "Interactions of Skyrmions with domain walls". In: *Phys. Rev. D* 61 (2 Dec. 1999), p. 025016. DOI: 10.1103/PhysRevD.61.025016. URL: https://link.aps.org/doi/10.1103/PhysRevD.61.025016.

[32] T. S. Misirpashaev. "The topological classification of defects at a phase interface". In: *Journal of Experimental and Theoretical Physics* 72.6 (June 1991), pp. 973–982. URL: http://www.jetp.ac.ru/cgi-bin/dn/e_072_06_0973.pdf.

[33] V. Eltsov, P. Kapitza, M. Krusius, and G. Volovik. "Superfluid $^3$He: a laboratory model system for quantum field theory". In: (Nov. 2012). URL: https://www.researchgate.net/publication/267778107_SUPERFLUID_3_He_A_LABORATORY_MODEL_SYSTEM_FOR_QUANTUM_FIELD_THEORY.

[34] M. Krusius, E. Thuneberg, and Ü. Parts. "A–B phase transition in rotating superfluid 3He". In: *Physica B: Condensed Matter* 197.1 (1994), pp. 376–389. ISSN: 0921-4526. DOI: https://doi.org/10.1016/0921-4526(94)90235-6. URL: http://www.sciencedirect.com/science/article/pii/0921452694902356.

[35] A. P. Finne, V. B. Eltsov, R. Hänninen, N. B. Kopnin, J. Kopu, M. Krusius, M. Tsubota, and G. E. Volovik. "Dynamics of vortices and interfaces in superfluid3He". In: *Reports on Progress in Physics* 69.12 (Nov. 2006), pp. 3157–3230. DOI: 10.1088/0034-4885/69/12/r03. URL: https://doi.org/10.1088%2F0034-4885%2F69%2F12%2Fr03.

[36] V. A. Gani, A. E. Kudryavtsev, and M. A. Lizunova. "Kink interactions in the (1+1)-dimensional $\varphi^6$ model". In: (2014). DOI: 10.1103/PhysRevD.89.125009. eprint: arXiv:1402.5903.

[37] S. Coleman. *Aspects of Symmetry*. Cambridge, U.K.: Cambridge University Press, 1985. ISBN: 9780521318273. DOI: 10.1017/CBO9780511565045.

[38] B. Felsager. *GEOMETRY, PARTICLES AND FIELDS*. Graduate Texts in Contemporary Physics. Odense: Univ.Pr., 1981. DOI: 10.1007/978-1-4612-0631-6.

[39] L. Perivolaropoulos. "Asymptotics of Nielsen-Olesen vortices". In: *Physical Review, D (Particles Fields); (United States)* 48 (Dec. 1993). ISSN: 0556-2821. DOI: 10.1103/PhysRevD.48.5961.

[40] W. R. Inc. *Mathematica, Version 12.0*. Champaign, IL, 2019.